NUMERICAL INVESTIGATION OF DROPWISE CONDENSATION ON PLAIN AND FUNCTIONAL SURFACES

by
HOSSEIN MOHASSEL

Submitted to the Graduate School of Natural Science and Engineering in partial fulfilment of the requirements for the degree of Master of Science

Sabancı University December 2023

ABSTRACT

NUMERICAL INVESTIGATION OF DROPWISE CONDENSATION ON PLAIN AND FUNCTIONAL SURFACES

HOSSEIN MOHASSEL

MECHATRONIC ENGINEERING M.S. THESIS, DECEMBER 2023

Thesis Supervisor: Prof. ALI KOŞAR
Thesis Co-advisor: Asst. Prof. ABDOLALI SADAGHIANI

Keywords: dropwise condensation, heat transfer enhancement, biphilic surface, superhydrophobic, droplet distribution, numerical analysis

Condensation, a natural phase change phenomenon, is extremely significant in a variety of applications, from power generation to electronics cooling. While previous studies have predominantly focused on experimental studies and single droplet simulations, there is a gap in the literature on the comprehensive numerical analysis of dropwise condensation and parameters affecting its performance. By simulating condensing flow on different surfaces and performing parameter studies, this thesis reveals the effect of steam mass flux, contact angle, material, subcooled temperature, and configuration. First, this study covers heat transfer analysis during flow condensation on surfaces with uniform wettability. The unique aspect of this thesis is using simulations to visualize the entire dropwise condensation cycle, elucidating the dynamic processes. The findings reveal that higher steam mass flux improves heat transfer, as droplet departure diameter adversely changes with steam mass flux. Surfaces with low wettability exhibit substantial improvements in heat transfer (up to 33% increase in heat transfer coefficient) at high steam mass fluxes compared to highly wettable surfaces. The second part of the thesis investigates patterned surfaces, and the effect of pattern size and mixed wettability on dropwise condensation behavior, droplet size, and heat transfer. The findings identify the optimum pattern size for maximizing the heat transfer performance. Over a variety of surface types, findings consistently revealed a beneficial relationship among higher contact angles, decreased departure droplets, and superior heat transfer performance. Furthermore, this thesis validates the developed numerical model through comparison with experimental results, which provides the reliability of the computational approach in accurately modelling dropwise condensation and in predicting and optimizing dropwise condensation behavior for different applications.

ÖZET

FONKSIYONAL VE DESENLI YÜZEYLER ÜZERINDE DAMLACIKLI YOĞUŞMANIN SAYISAL İNCELEMESI

HOSSEIN MOHASSEL

MEKATRONIK MÜHENDISLIĞI YÜKSEK LİSANS TEZİ, ARALIK 2023

Tez Danışmanı: Prof. Dr. ALI KOŞAR
Ortak Danışman: Asst. Prof. ABDOLALI SADAGHIANI

Anahtar Kelimeler: damla yoğunlaşma, isi transferi geliştirme, bifilik yüzey, süperhidrofobik, damlacık dağılımı, sayısal analiz

Yoğunlaşma, doğal bir faz değişim olayı olarak, enerji üretiminden elektronik soğutma alanına kadar çeşitli uygulamalarda son derece önemlidir. Önceki çalışmalar genellikle deneysel çalışmalara ve tek damlacık simülasyonlarına odaklanmış olsa da, damlalı yoğunlaşma ve performansını etkileyen parametrelerin kapsamlı sayısal analizi konusunda literatürde bir boşluk bulunmaktadır. Farklı yüzeylerde kondanse akışını simüle ederek ve parametre çalışmaları gerçekleştirerek, bu tez buhar kütlesi akışı, temas açısı, malzeme, soğutulmuş sıcaklık ve konfigürasyonun etkilerini ortaya çıkarır. İlk olarak, bu çalışma uniform ıslanabilirlik özelliklerine sahip yüzeylerde akış yoğunlaşması sırasında ısı transfer analizini kapsar. Bu tezin benzersiz yanı, dinamik süreçleri aydınlatmak için simulasyonları kullanarak damlalı yoğunlaşma döngüsünün tamamını görselleştirmesidir. Bulgular, daha yüksek buhar kütlesi akışının ısı transferini artırdığını, çünkü damla ayrılma çapının buhar kütlesi akışı ile olumsuz bir şekilde değiştiğini ortaya koymaktadır. Islanabilirliği düşük yüzeyler, yüksek buhar kütlesi akışlarında (%33'e kadar ısı transfer katsayısında artış) yüksek ıslanabilir yüzeylere kıyasla önemli iyileştirmeler göstermektedir. Tezin ikinci kısmı desenli yüzeyleri ve desen boyutunun damlalı yoğunlaşma davranışı, damla boyutu ve ısı transferi üzerindeki etkilerini incelemektedir. Bulgular, ısı transfer performansını en üst düzeye çıkarmak için optimal desen boyutunu belirlemektedir. Farklı yüzey tiplerinde, bulgular sürekli olarak daha yüksek temas açıları, azalmış ayrılma damlacıkları ve üstün ısı transfer performansı arasında faydalı bir ilişki olduğunu ortaya koymaktadır. Ayrıca, bu tez, deneysel sonuçlarla karşılaştırma yaparak geliştirilen sayısal modeli doğrular; bu da sayısal yaklaşımın damlalı yoğunlaşmayı doğru bir şekilde modelleme ve farklı uygulamalar için damlalı yoğunlaşma davranışını tahmin etme ve optimize etme konusundaki güvenilirliğini sağlar.

ACKNOWLEDGEMENTS

I extend my heartfelt gratitude to my dissertation advisor, Prof. Ali Koşar, for his unwavering guidance and support throughout this academic endeavor. His expertise and encouragement were instrumental in shaping the direction of this research.

I am grateful to my co-advisor, Asst. Prof. Abdolali Sadaghiani, for his invaluable guidance and support throughout this dissertation. Their expertise and mentorship have significantly contributed to the success of this research.

To my dissertation committee, Prof. Metin Muradoğlu, Prof. Erdal Çetkin, Prof. Emre Erdem, I appreciate your valuable insights and constructive feedback that significantly contributed to the refinement of this dissertation.

I am deeply indebted to my friends and colleagues who offered camaraderie and assistance when needed, making this journey more enjoyable and enriching.

Most importantly, I want to express my profound gratitude to my wife, Fatemeh. Your unwavering support, patience, and understanding have been the bedrock upon which I built this dissertation. Your belief in me sustained me through the challenges, and your sacrifices did not go unnoticed. This achievement is as much yours as it is mine, and I am profoundly grateful for your presence in this journey.

To my family, thank you for your constant love and encouragement. Your belief in my abilities has been a driving force.

This dissertation is dedicated to all those who, in various ways, have contributed to its completion. Your collective support has left an indelible mark on this academic achievement.

Hossein Mohassel

This thesis is dedicated to my beloved family

TABLE OF CONTENTS

LIST OF TABLES

LIST OF FIGURES

LIST OF ABBREVIATONS

DWC Drop Wise Condensation…… 1
FWC Filmwise Condensation…….……...1
HTC Heat Transfer Coefficient……...….. 2
SFE Surface Free Energy…….……...……3
VOF Volume of Fraction……...….8
CFD Computational Fluid Dynamics ……...… 9
SMF Steam Mass Flux …… 6
HPHI Hydrophilic……..…59
HPHO Hydrophobic…….…….59
SHPHO Superhydrophobic…….……..59

NOMENCLATURE

u Velocity (m/s)

S_m Mass source term $(kg/m^3.s)$

S_q Energy source term $(J/m^3.s)$

t Time (s)

p Pressure (Pa)

g Gravitational acceleration (m/s^2)

F_s Continuum surface force $(kg/m^2.s^2)$

T Temperature (k)

E Total energy per unit mass (J/kg)

k Thermal conductivity $(W/m.K)$

$\dot{m}$ Mass transfer rate (kg/s)

c_p Specific heat capacity $(J/kg.K)$

Greek Symbols

θ Contact angle (°)

ρ Density (kg/m^3)

τ Stress tensor (Pa)

α Volume fraction

σ Surface tension (N/m)

μ Dynamic viscosity $(Pa.s)$

Subscripts

l liquid

v Vapor

g Gas

sat Saturation

1 INTRODUCTION

Condensation is a fundamental phase-change phenomenon that plays a crucial role in a wide range of industrial and environmental applications. It is the transformation of a vapor or gas into a liquid when it comes into contact with a cold surface. Understanding and optimizing condensation is vital for enhancing the efficiency and sustainability of numerous technologies and industries including power generation [1-3], solar thermal applications [4], building and environmental thermal systems [5], water desalination systems [6-8], air conditioning [9, 10], and electronics cooling [11, 12]. Therefore, improving the condensation process yields more efficient and compact condensers, which in turn decreases the system weight and size and boosts output energy in a variety of engineering applications, which could cause in lower costs and emissions of CO_2.

Depending on the surface wettability, there are two distinct scenarios for condensation [13]: dropwise condensation (DWC) when liquids do not wet the surface and filmwise condensation (FWC) when the surface is wetted by liquids, schematically shown in FIG 1-1.

Dropwise condensation (DWC) is a specific mode of condensation that has attracted a great deal of interest during recent years for its potential to significantly improve heat transfer and energy efficiency [14]. In this mode, vapor or gas condenses into discrete droplets on the condensing surface, which then fall off under gravity or shear force. Unlike filmwise condensation, where a continuous liquid film forms, dropwise condensation offers advantages such as reduced surface wetting and improved thermal performance. These features make it appealing for applications where efficient heat transfer is crucial.

Two methods are employed to improve condensation heat transfer: active and passive methods. Active methods involve applying external forces such as an electrical field [15], while passive approaches control condensate droplet nucleation and growth by manipulating surface properties or adding fluid additives, resulting in an improved performance [16].

The growing significance of dropwise condensation and the potential of engineered surfaces for achieving high heat transfer rates, reduced energy consumption, and enhanced environmental sustainability have driven extensive research efforts during recent years. Advances in materials and surface treatments, coupled with a deeper understanding of the underlying physical mechanisms, have proposed innovative opportunities across various industries.

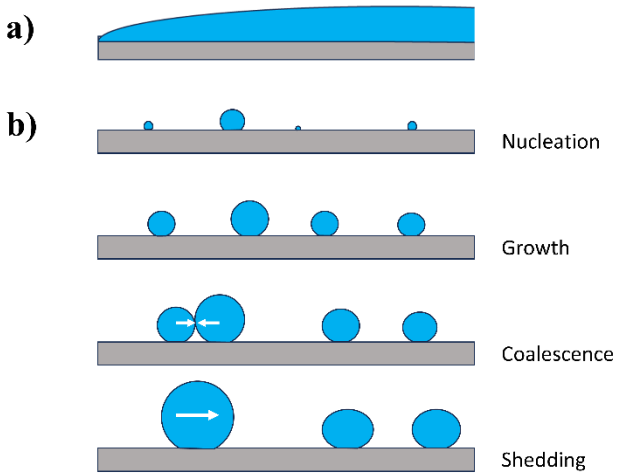

FIG 1-1 Schematic showing the condensation types: a) filmwise condensation (FWC), b) dropwise condensation (DWC)

This thesis aims to comprehensively examine dropwise condensation behavior on engineered surfaces, exploring key parameters such as the steam mass flux, wettability, temperature, and material. To investigate the underlying mechanisms governing dropwise condensation, it is crucial to delve into fundamentals of this process. This thesis presents a numerical analysis on parameters influencing nucleation, droplet growth, and droplet departure in dropwise condensation. By gaining a deeper understanding of the physics involved, we can lay the foundation for optimizing the condensation performance on engineered surfaces. So that every problem could be addressed in systems involving condensation heat transfer.

1.1 Literature Review

1.1.1 Plain Surfaces

Condensation is categorized as filmwise condensation (FWC) or dropwise condensation (DWC) [17-19]. In FWC, heated vapor in contact with a cold surface forms a thin layer of condensed water on the surface, which adds another layer of heat transfer resistance. On the other hand, in DWC, vapor condensates into tiny droplets, following periodically a four-step process: nucleation, growth, coalescence, and removal of droplet from the surface. DWC heat transfer coefficient (HTC) is typically 4– 28 times greater than FWC's [20-22] due to discrete drops having lower thermal resistance than a continuous film. Therefore, improvement in any of these steps will enhance the efficiency of the condensation process, which will boost the energy efficiency of the entire industrial system. Thus, optimization of this process plays an indispensable role in energy and natural resource consumption reductions for a wide range of applications [23-25]. Either passive techniques such as surface engineering and altering surface wettability properties or active techniques such as vibration [26], acoustic [27], gas generation [28], and electric fields [29] could be used for this task. Dropwise condensation is also effective in reducing the size and weight of the condensers such as in thermal management devices [30] and air conditioning systems [31].
Comparing condensation modes, dropwise condensation reveals lower wettability and surface

free energy (SFE). The contact angle (θ) is used to determine the wettability or hydrophobicity level of a surface (as shown in FIG 1-2). The creation of a water droplet contact angle is explained by Thomas Young [32] in terms of the surface energy of the surrounding vapor, substrate, and fluid. A surface is classified as hydrophobic if the contact angle is greater than or equal to 90 degrees. Moreover, a surface with a contact angle greater than 150 degrees is highly hydrophobic, considered as superhydrophobic. While a surface with a contact angle less than 90 degrees could be considered as hydrophilic. Droplet nucleation is influenced by intrinsic wettability, enabling condensation at lower temperature differences on hydrophilic surfaces. The advantage of dropwise over filmwise condensation lies in surface renewal, wherein droplets slide down at a specific size, which facilitates small droplet growth through direct vapor contact. Surface renewal enables the regeneration of small droplets on condensing surfaces with low thermal resistance and promotes enhanced heat transfer. Studies by Cassie and Baxter [33] and Wenzel [34] explored the impact of surface microstructure on hydrophobicity. Dettre and Johnson [35, 36] investigated the influence of contact angle hysteresis on wettability, defined as the difference between the contact angles of advancing and receding droplets. Yaminksy [37] attributed varied contact angles to surface roughness, which affects droplet contact-line pinning. Surface modifications that increase the contact angles and minimize contact angle hysteresis typically enhance dropwise condensation heat transfer.

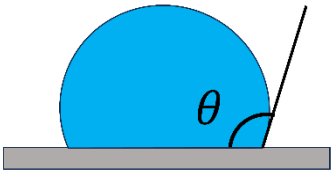

FIG 1-2 Schematic of a droplet on a surface with a contact angle of θ

Since Schmidt et al.'s discovery of DWC [17], dropwise condensation over nonwetting substrates has drawn much interest. A thorough investigation of flow and heat transfer fundamentals reveals the effectiveness of surface modification as a valuable tool for enhancing condensation heat transfer through continuous surface renewal and droplet shedding [9, 38, 39]. Surface modification, a broad field that includes diverse techniques, has evolved with advances in nanotechnology and microfabrication, which allows access to more sophisticated methods [40-45] and such modifications encompass changes in wettability, adhesion, roughness, chemical composition. Surface modification, particularly related to wettability control with superhydrophobic or hydrophobic surfaces, has attracted significant attention [46-48]. Microstructured surfaces exhibit prolonged operational reliability while enhancing the condensation performance.

During the 1970s, various studies explored techniques to enhance and sustain dropwise condensation [19, 49, 50]. The focus was primarily on coating surfaces with low surface energy materials. In a specific investigation [51], the researchers experimentally examined the influence of wall wettability on steam condensation in microchannels, which revealed significant effects on the heat transfer performance, pressure drop, and flow field regarding

the hydrophobicity of the microchannel's wall. Compared to hydrophilic surfaces, hydrophobic surfaces resulted in higher heat transfer rates and pressure drops. In subsequent decades, advanced surface engineering methods were employed to facilitate early droplet departure through coalescence-induced jumping or gravity to enhance rates of heat and mass transfer during dropwise condensation. As an example, Lee et al. [52] experimentally investigated the impact of artificial micro- and nano-sized porous surfaces on the thermal efficiency of steam condensers. Their study suggested that these surfaces can enhance dropwise condensation by increasing nucleation rates, reducing the formation of large droplets, and promoting the creation of tiny droplets.

The critical size at which droplets can be detached from the surface, is a vital aspect of dropwise condensation. Sliding droplets clear the surface, which allows the nucleation of new and smaller droplets. Smaller droplets ($R \sim 10\ \mu m$) in dropwise condensation exhibit more efficient heat transfer characteristics than larger ones [19, 53, 54]. Therefore, increasing the percentage of small droplets on the surface is desirable. Passive methods, such as tilting the surface [55, 56] or aligning it vertically [57], take advantage of gravity to enhance droplet removal. Surface energy gradients constitute another technique to enhance droplet mobility [58, 59]. Macner et al. [60] demonstrated a shift in droplet size distribution towards smaller droplets compared to homogeneous energy surfaces. Furthermore, superhydrophobic surfaces have been proposed to enhance condensation in numerous studies [61-63]. Dropwise condensation on appropriately engineered superhydrophobic surfaces with low adhesion has the potential in achieving significantly higher heat transfer coefficients, up to 100% more than those on hydrophobic surfaces [63, 64]. This improvement in heat transfer is attributed to condensate droplets jumping of the surface through coalescence, a phenomenon known as "jumping-droplet condensation"[65, 66]. Coalescence leads to the removal of condensate, which results in a reduction in the average droplet size on the surface, and consequently, a decrease in vapor-to-surface thermal resistance [53, 67, 68].

Wen et al. [69] controlled droplet behavior in each condensation stage during condensation by creating unique superhydrophobic surfaces with nanowire micropatterns. This method led to enhanced heat transfer and reduced departure diameter. Compared to superhydrophobic surfaces with uniform nanowires, they observed 37% increase in the required heat flux for the condensation of jumping droplets. The potential in enhancement in condensation heat transfer has also been explored for advanced two-tier textured superhydrophobic surfaces, which facilitated continuous dropwise condensation and rapid removal of condensate droplets [46]. However, nucleation within the roughness features hinders mobility by pinning droplets to the surface during condensation [70, 71]. Surfaces facilitating condensate droplet generation in the Cassie state have been explored to overcome these limitations, which promoted sustained dropwise condensation and rapid condensate droplet removal [46, 71]. A comparison of single-level structured surfaces and a two-tier roughness surface with nanowires on micro-pyramids for condensation in ambient conditions revealed superior droplet mobility on the two-tier surface under both wet (condensation) and dry conditions [72]. Reduced adhesion to the pyramid side and prevention of the transition from the Cassie to Wenzel state were observed due to the structures on the micro-pyramids of the two-tier surface.

The micro-scale coalescence of droplets on nanostructured superhydrophobic surfaces, where surface energy was released and droplets jumped away from the surface against gravity, has

gained increased attention since its first description by Boreyko and Chen [73]. Consequently, superhydrophobic nanostructured surfaces were recently designed to promote droplet jumping-induced removal [74, 75]. Using nanostructured CuO surfaces that facilitated droplet jumping during condensation, Miljkovic et al. observed a 30% improvement in condensation heat transfer [63].

Employing textured surfaces coated with a lubricating liquid is an additional strategy to enhance droplet mobility, and enabled droplets to exhibit very low contact angle hysteresis ($\sim 1°$) and to promote dropwise condensation [76]. A recent study by Anand et al. [77] demonstrated that condensate droplets as small as $100\ \mu m$ became highly mobile on a surface with hierarchical micronanoscale texture saturated with lubricant.

The mentioned droplet condensation studies were conducted in vast, unbounded environments, primarily addressing steam droplet condensation and neglecting vapor shear. In those cases, coalescence-induced jumping or gravity controls the primary droplet detachment mechanism. However, during flow condensation, vapor shear becomes the primary droplet departure mechanism. Reducing the cross-sectional area of the channel increases vapor shear rates and vapor mass fluxes. The potential of hydrophobic surfaces in improving the steam flow condensation heat transfer performance in minichannels and microchannels was explored in the literature [51, 78-82]. Recently, Chehregani et al. [83] investigated condensed droplet behavior in vapor flow with varying vapor quality and its impact on enhancing heat transfer. They conducted heat transfer analysis, examined droplet dynamics, and performed a visualization study on flow condensation in a minichannel. Increasing the steam mass flux (SMF) led to a decrease in droplet departure diameter and a shift in droplet size distribution to smaller radii, thereby improving condensation heat transfer. Comparing the tested superhydrophobic surface to the reference plain hydrophobic surface, up to a 33% improvement in the heat transfer was reported at lower steam quality.

Smaller droplets ($100\ nm$ to $10\ \mu m$) contribute more to the condensation heat transfer coefficient for thin hydrophobic coatings ($< 1\ \mu m$) because their conduction thermal resistance is lower than that of larger droplets ($> 10\ \mu m$ to $1mm$). Calculating the heat transfer rate in dropwise condensation involves the determination of the heat flux from a condensing surface through a single droplet and then consideration of the heat flux through all droplets on the surface using a distribution that provides the number of droplets within a specific size range on an identified surface area [19, 84, 85]. This method assumes that droplets of different sizes are uniformly dispersed across the condensing surface at random nucleation sites. Therefore, understanding the droplet size distribution is crucial for determining the overall surface heat transfer in dropwise and jumping-droplet condensation.

Numerous studies investigated the periodic distribution of droplet sizes during dropwise condensation, and various parameters, including surface characteristics [86-88], surface orientation [89-93], and subcooling temperature [94-96] influenced the rate of cyclic droplet formation. The presence of droplets from various generations and sizes on the surface of the same time which is due to multiple coalescences, complicates droplet size distribution modeling. Since the pioneering work of Le Ferve and Rose [97], who introduced the concept of droplet size distribution for analyzing heat transfer during dropwise condensation, several models have been developed to predict the droplet size distribution for precise estimation of

heat transfer during dropwise condensation [19, 98-103].

Rose et al. investigated the steady-state distribution of droplet sizes during dropwise condensation on hydrophobic surfaces and emphasized on scenarios where droplets predominantly grow through coalescence. Both numerical and experimental methods were employed to validate the droplet distribution [104]. While the Rose distribution was initially derived empirically, it was also independently modeled using fractal theory [105]. Abu Orabi developed an analytical population balance model to predict the size distribution function for droplets smaller than the coalescence radius, using the Rose distribution to establish boundary conditions for the coalescence radius [100, 106]. However, the population balance concept lacks support from computational or experimental evidence. Despite its suitability for conventional dropwise condensation, Rose's distribution is not applicable to jumping-droplet condensation and does not accurately represent the associated mechanics.

1.1.2 Biphilic Surfaces

Achieving dropwise condensation (DWC) with optimal features such as sufficient nucleation sites, rapid droplet growth, and prompt droplet departure is challenging but crucial to prevent thin liquid film formation on solid surfaces. Hence, the formation of dropwise or filmwise condensation depends significantly on the surface wettability. Recently, biphilic surfaces with mixed wettability were explored to provide sustained and effective dropwise condensation [107-110]. The benefits of both dropwise and filmwise condensation can be combined on a single surface by carefully developing surfaces with the optimal geometry and wettability. Hydrophilic or less-hydrophobic surfaces exhibit higher nucleation rates than hydrophobic surfaces due to a smaller free energy barrier [111], which heavily depends on the surface wettability [112]. This implies that while a hydrophilic surface is necessary for achieving a high condensation rate, a hydrophobic surface is required for DWC and a high heat transfer coefficient [113]. Although hydrophobic surfaces generally have higher heat transfer coefficients than hydrophilic surfaces, arranging different hydrophobic and hydrophilic sections in a pattern may or may not improve the condensation heat transfer coefficient [31], which is highly dependent on the configuration. The study by Leu et al. [114] indicates that specific condensation surfaces with distinct patterns of hydrophobic and hydrophilic regions can yield higher heat fluxes than completely hydrophobic surfaces, while other patterns may produce heat fluxes lower than those of completely hydrophilic surfaces.

Achieving desired dropwise condensation with a high heat transfer rate requires a thorough understanding and fine control of nucleation, development, coalescence, and droplet departure on condensation surfaces with specific designs. The improvement of dropwise condensation (DWC) and associated heat transfer depends on effectively balancing diverse surface wettabilities required at different phases of the condensation cycle. Various approaches can be employed to create two or more zones with different degrees of wettability on condensing surfaces at different scales and ratios (i.e., pattern to contrasting environment ratio). The degree of wettability contrast in the pattern design plays a crucial role in determining the condensation heat transfer performance of the surface. Effective wettability contrast enhances

droplet mobility, droplet-departure frequency, and condensation heat transfer rates [59, 60]. Furthermore, this technique can mitigate impediments by reducing the quantity and/or size of droplets suspended below condenser tubes [115] or by partially controlling the condensate's course and/or direction.

The study of Daniel et al. [59] revealed that droplets tend to migrate arbitrarily from a less wettable side to a more wettable one. Subsequently, Chen and colleagues [116] created micropyramids with nanograss and a center-to-center spacing of $20-40\ \mu m$, which affected a 65% increase in droplet number density with mixed wettability. Due to the extremely low steam mass flux in these investigations, the impact of the vapor drag force on the condensing droplets was disregarded. Later, Chehregani et al. [117] studied the impact of flow on condensing droplets on biphilic surfaces, and reported optimum island hydrophobic diameters on a superhydrophobic surface as a function of steam mass flux.

Nature inspired the generation of engineered surfaces promoting dropwise condensation, by mimicking nanofeatures seen on lotus leaves [118], Nepenthes pitcher plants [119], moss Rhacocarpus [120], and Namib Desert insects [121]. Advanced engineering techniques such as lithography [122], plasma treatment [123], electrodeposition [124], and sol-gel procedures [125] were employed to produce different micro/nanostructures. Surface free energy is adjusted through functional coatings using organic molecules, noble metals, rare earth oxides, polymers [126, 127], self-assembled monolayers, [128], and porous coatings [129].

Maintaining dropwise condensation is crucial and requires a detailed understanding of droplet behavior on various patterned surfaces. However, several significant issues should be resolved before widespread use of engineered surfaces in energy systems. For instance, under severe subcooling conditions, nucleation of nanoscale droplets within micro/nanostructures might lead to pinned droplets and flooding issues [68, 130-132]. Investigating the flooding mechanism and pinned droplets on micro/nanostructures is essential to prevent or delay the formation of undesirable liquid thin films for effective heat transfer.

Additionally, understanding the effects of pattern design on wettability contrast and condensation rates often involves parametric research efforts through experimental tests. The optimum performance under a given operating condition can be achieved by determining the best arrangement for a specific patterned surface design. However, the fundamental characteristics of the fabrication process make experimental optimization challenging and costly. Therefore, instead of relying on time-consuming and expensive experimental parametric research efforts, modeling condensation on surfaces with various patterns can provide insights into optimal design.

Previous valuable computational investigations highlighted the significant influence of nucleation site quantity on droplet growth behavior [133]. A mathematical model predicting droplet evolution, coalescence, and departure, incorporating contact angle and hysteresis variation was successfully developed and validated against experimental data [56]. Subsequent numerical analyses explored droplet dynamics and heat-transfer performance of various wettability patterns. Specific attention was given to the impacts of pillar microstructure on droplet dynamics, which include coalescence-induced droplet jump, pillar-induced droplet jump, and droplet dragging by wettability gradients [134]. Later, numerical studies employing the VOF (volume of fraction) method investigated different combinations of patterned textures to identify optimal designs for desired dropwise condensation [135].

The majority of studies in the literature have focused extensively on the condensation heat transfer on nanostructured superhydrophobic surfaces, which demonstrate their potential to enhance condensation heat transfer performance. However, these studies often overlooked the impact of steam flow, specifically the vapor shear rate. Additionally, visualization studies in existing literature have primarily focused on droplet cycle time, neglecting other crucial visual parameters related to droplet dynamics, such as droplet number density, droplet departure diameter, and the distribution of droplets on the condensing surface at different steam mass fluxes.

Furthermore, in the exploration of condensation heat transfer on biphilic surfaces, while existing studies provide valuable insights into the cooperative effects of biphilic surfaces, the optimal ratio of pattern to superhydrophobic surface areas, crucial parameters for achieving optimal thermal performance, have not been thoroughly investigated. Moreover, while these studies offer valuable information about condensation heat transfer on various hybrid surfaces, where the effect of vapor shear is often neglected, there remains a scarcity of numerical research specifically addressing flow condensation on biphilic surfaces within a minichannel, where vapor shear force governs the mechanism for droplet departure.

1.2 Motivation and Objective of the Thesis

Numerical simulation techniques provide a robust tool for gaining insights into the intricate dynamics of dropwise condensation. This dissertation utilizes Computational Fluid Dynamics (CFD) and covers simulations conducted using the Ansys FLUENT 2021 R2 software using the VOF method. This method provides a detailed understanding of local flow behavior, encompassing droplet distribution, size, and their influence on condensation rates.

This thesis aims to deepen the understanding of dropwise condensation physics at the microscale by presenting fluid flow patterns, heat transfer, and droplet dynamics. Additionally, the numerical simulations were validated against experimental results for contributing to the development of accurate models and advancing the field.

Beyond fundamental research, the application of numerical simulation techniques aids in designing and optimizing industrial condensers. The integration of numerical simulations with experiments will enable the exploration of diverse operating conditions, provide insights into dropwise condensation behavior and optimize practical applications. Simulations help in optimizing geometric parameters such as pattern features and surface coatings and improving the overall system performance. This thesis addresses gaps in the literature, related to a comprehensive model for dropwise condensation, and focuses on the crucial droplet evolution and mobility process on plain and biphilic surfaces.

Numerical investigation of heat transfer enhancement in dropwise condensation in a minichannel with a surface with uniform wettability was first made by the considering various steam mass fluxes, wall temperatures, materials, and wettabilities. Results reveal the efficiency of superhydrophobic surfaces in improving condensation heat transfer.

Furthermore, this thesis also explores heat transfer in flow condensation on biphilic surfaces,

conducting a parametric analysis was made for optimum designs. Transient simulations provide visuals of droplet dynamics, indicating increased nucleation sites due to surface wettability gradient. The developed model provides the accuracy in capturing droplets of different sizes simultaneously, enhancing understanding of nucleation, development, coalescence, and departure of droplets on specialized surfaces. As a result, thesis contributes to achieving desired dropwise condensation with high heat transfer rates and improved droplet mobilities.

2 METHODOLOGY

This chapter outlines the employed methodology for exploring dropwise condensation on both horizontal plain and engineered surfaces. Comparisons in the heat transfer performance between plain and biphilic surfaces were made, by using numerical simulations in the Ansys FLUENT 2021 R2 software. Our goal is to gain insight into the underlying physics and optimization in the surface design for improved heat transfer efficiency. This chapter covers details on the simulation setup, governing equations, and numerical methods employed to achieve the objectives of the thesis.

2.1 Governing Equations

The simulations were based on conservation equations for mass, momentum, and energy. The Navier-Stokes equations were solved for the fluid flow, while the energy equation accounts for heat transfer. The continuity equation is expressed as follows:

$$\frac{\partial \rho}{\partial \mathrm{t}} + \nabla.(\rho u) = \mathrm{S}_m \quad (2\text{-}1)$$

where t is the time, ρ is the density, u is the velocity, and S_m is mass source term. The momentum equations are expressed as:

$$\frac{\partial \rho}{\partial t} + \nabla.(\rho u u) = -\nabla p + \rho g + \nabla.(\tau) + F_s \quad (2\text{-}2)$$

where p stands for the static pressure, τ is the stress tensor, ρg and F_s are the gravity and external body forces, respectively. The energy equation is described as:

$$\frac{\partial (\rho E)}{\partial t} + \nabla.[u(\rho E + p)] = -\nabla.(k \nabla T) + S_q \quad (2\text{-}3)$$

where E, k, and T represent the energy, thermal conductivity, and temperature, respectively; S_q is energy source term accounting for heat transfer changes during phase change.

2.2 Numerical Simulation Setup

2.2.1.1 Computational Domain and Boundary Conditions

In this thesis, a three-dimensional model of a rectangular cross-section minichannel was developed with computational domain dimensions based on a specific experimental setup [117], as shown in the FIG 2-1. The horizonal surface with the dimensions of $37 \times 10 \times 0.5\ mm$ was considered. Due to numerical tool limitations and time constraints, parametric studies were conducted using a 2D model.

The boundary conditions were determined based on the specific experimental setup. The inlet conditions, including the mass flow rate and temperature, were set to match with the experimental conditions. Five different steam mass fluxes (10,20,30,40,50 $kg/m^2\ s$) were

examined. The outlet boundary was specified as a pressure outlet. The lower boundary condition was set to be a constant wall temperature with a $0.5\,mm$ thickness, employing materials including copper, aluminum, and steel. Periodic boundary conditions were applied to side walls, and the non-slip boundary condition was implemented on the wall. Gravity effects were considered in the y-direction.

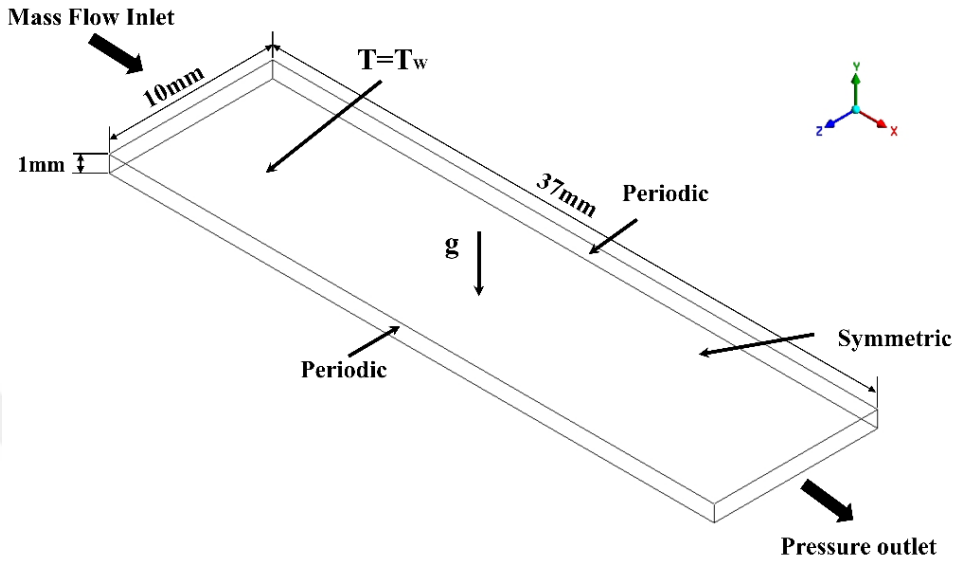

FIG 2-1: Schematic of computational domain and boundary conditions

2.2.2 Mesh and Mesh Convergence Analysis

The computational domain, where tiny droplets form on the cooled surface, was meshed using structured meshes with quadrilateral (2D) or hexahedral (3D) linear elements. Elements adjacent to the cooled surface were refined to smaller sizes to capture micro-scale droplet growth. To prevent droplets from leaking into coarser mesh regions, a 1.2 ratio of element size growth was implemented in the refinement region.

To ensure accuracy, mesh convergence analysis was conducted. FIG 2-2 displays the three-dimensional mesh and example meshes used for the mesh independence study, each corresponding to a two-dimensional model with 25,000, 280,000, 400,000, and 625,000 elements. Heat transfer coefficient examination showed that mesh convergence was achieved with over 280,000 elements, where resulted in a 2% deviation from as a benchmarking case for the ideal number of elements, illustrated in FIG 2-3. As a result, this work utilized 280,000 cells for precision and computational efficiency at the same time.

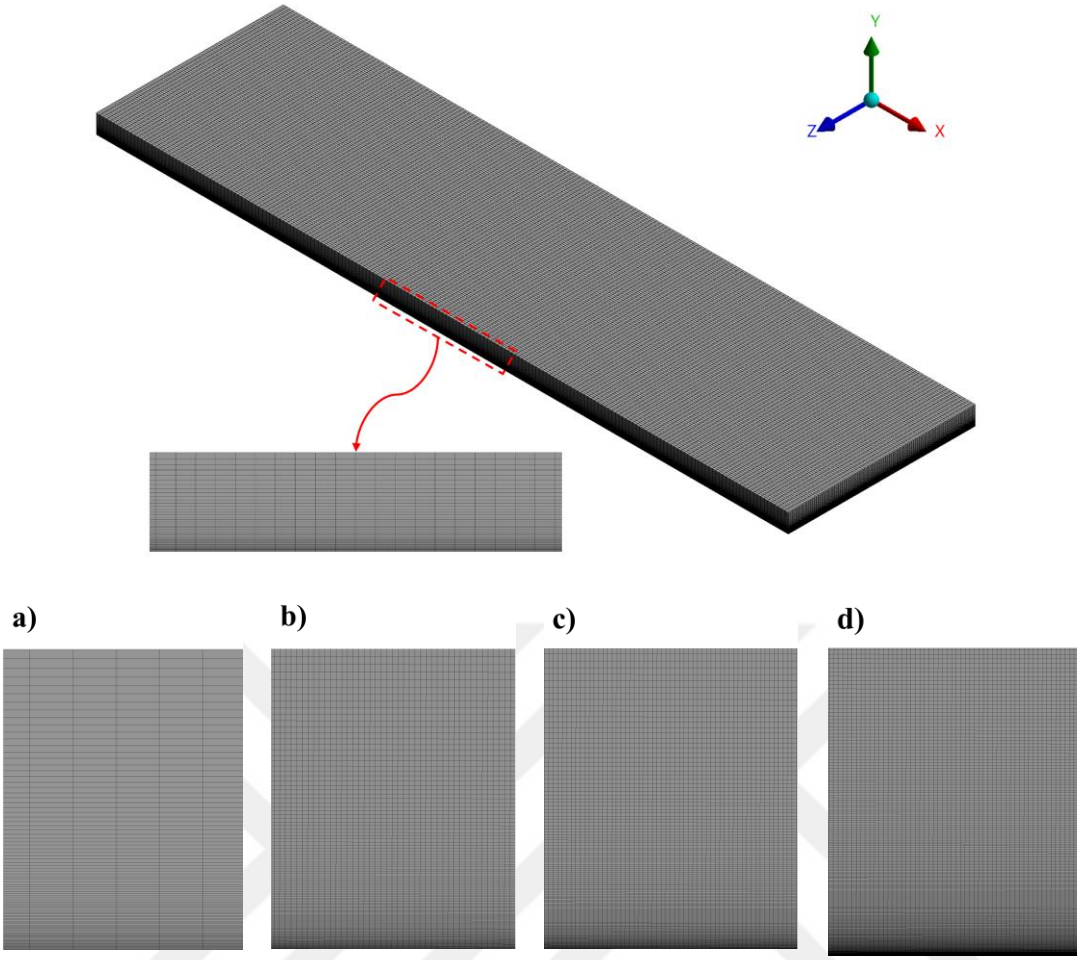

FIG 2-2: Mesh configuration of three-dimensional model's computational domain and a zoomed-in view of the mesh near the cooled wall, (a-d) Different Mesh Sizes used for the mesh independency study: a) 25,000, b) 280,000, c) 400,000, and d) 625,000 elements

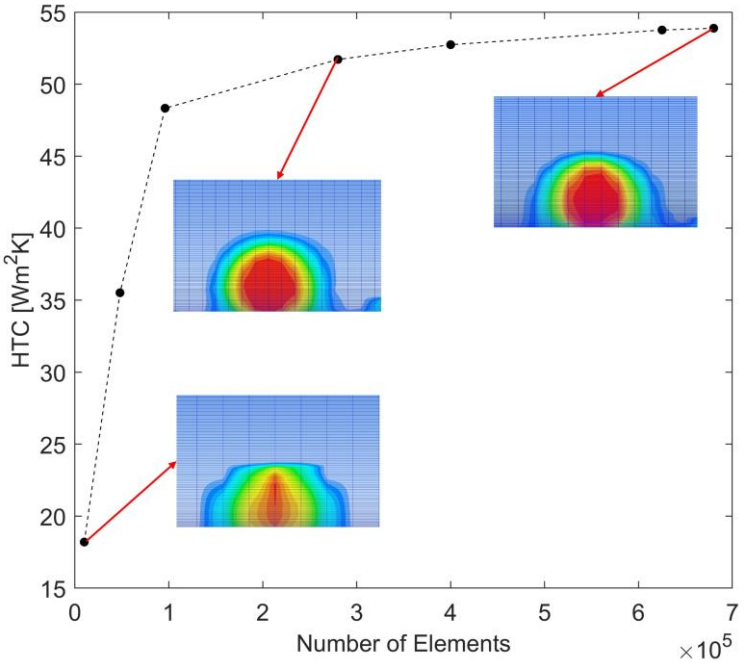

FIG 2-3: Mesh independency study of the 2D-model on a superhydrophobic surface of a steam mass flux of 10 kg/m^2s, which displays heat transfer coefficient with respect to varying mesh elements

2.2.3 Material and the Physical Properties

Material properties of the working fluid including the density, viscosity, and thermal conductivity were obtained from database values in Table 2-1. Density is considered to be affected by temperature, and enthalpies adjusted to ensure that the variation between enthalpies equates to the latent heat. Surface properties, such as surface tension and contact angle, were used in simulations to address their impact on the heat transfer performance. The surface material was copper with a 0.5 mm thickness in all studies, except when specified as aluminum or steel. For superhydrophobic surfaces, the contact angle was 172 degrees, for hydrophobic surfaces, it was 131 degrees, and for hydrophilic surfaces, it was 70 degrees.

Table 2-1 Material properties of the phases

	Water Liquid	Water Vapor	Two-phase
Density [kg/m^3]	$\rho_L = -0.0026429T^2 + 1.252209T + 859.0083$	Ideal gas	
Dynamic Viscosity [$mPas^{-1}$]	0.001003	Piecewise polynomial	
Thermal Conductivity [$W/m\ k$]	0.6	0.0261	
Enthalpy [kJ/kg]	0	4.068e+07	
Specific Heat Capacity [$J/kg\ k$]	4182	1.34e-05	
Latent Heat of vaporization [kJ/kg]	4.068e+07		
Surface Tension Coefficient [N/m]			0.0589

2.2.4 Simulation Procedure

The dropwise condensation of water in a horizontal minichannel was numerically simulated using the commercial CFD program ANSYS FLUENT 21 R2 and the pressure-based finite volume technique. The second-order upwind differencing method was applied to discretize the terms in the momentum and energy equations. Pressure-velocity coupling was achieved using the PISO method.

To visualize droplet growth, coalescence, and departure, a transient three-dimensional Volume of Fluid (VOF) model was employed. This model was capable of continuously tracking the liquid-vapor interface and droplet trajectories. Gravity was considered in the Y direction. Surface wettability effects were modeled by integrating the surface tension model with the wall adhesion angle. The Hertz-Knudsen equation, derived from kinetic theory, modeled condensation. Turbulent fluctuations in velocities and scalar values were described using the $k-\omega$ model. The primary phase was set as water vapor, and the secondary phase was set as liquid.

2.2.4.1 Volume of Fluid (VOF) Method

The VOF method was employed to model multiphase flows during condensation by tracking the liquid-gas interface through solving a transport equation for the volume fraction of the liquid phase. This approach can accurately represent interface dynamics, including droplet formation, growth, and shedding.

In the VOF model, a single set of equations for one phase is solved, and the solution is then shared between phases, which considerably reduces simulation time where the location of the interfaces of phases and the physical characteristics of the interfaces change with each iteration of the calculation. This allows for precise determination of phase presence by monitoring the location of the interface. The VOF model can handle two or more immiscible fluids and can trace their movement by solving a single set of Navier-Stokes equations for each fluid's volume fraction across the computational cell. Thus, in every control volume, the presence of a certain phase can be precisely determined from the volume fraction in any of the following three scenarios. In our study, using the volume fraction of the vapor phase as an example, if $\alpha_v = 1$, the vapor phase fills the entire cell. The liquid phase occupies the cell if $\alpha_v = 0$. There is a liquid-vapor interface in the cell if $0 < \alpha_v < 1$. The total volume fraction regarding the continuity equation of the phases remains consistent in each control volume as:

$$\alpha_v + \alpha_l = 1 \tag{2-4}$$

where α_l and α_v are volume fractions of liquid and vapor, respectively.

In this study, the secondary phase was considered to be liquid phase; the governing equations were solved only for the secondary phase, and Eq(2-4) was used to determine the volume fraction of the primary phase (α_v). The governing equations in the concept of the VOF model were stated as follows with the continuity equation rewritten:

$$\frac{\partial(\alpha_l \rho_l)}{\partial t} + \nabla.(\vec{u}\alpha_l \rho_l) = \dot{m}_{g\to l} \tag{2-5}$$

$$\frac{\partial(\alpha_v \rho_v)}{\partial t} + \nabla.(\vec{u}\alpha_v \rho_v) = \dot{m}_{l\to g} \tag{2-6}$$

where $\dot{m}_{g\to l}$ and $\dot{m}_{l\to g}$ are the source terms indicating volumetric mass transfer rates through the droplet interface, as described in section 2.1. The momentum equation, shared between phases through physical characteristics μ and ρ, can be expressed as:

$$\frac{\partial}{\partial t}(\rho_l \vec{u}) + \nabla.(\rho_l \vec{u}\vec{u}) = -\nabla p + \rho g + \nabla.\left[\mu(\nabla\vec{u} + \nabla\vec{u}^T) - \frac{2}{3}\mu\nabla.\vec{u}I\right] + F_s \tag{2-7}$$

Here, F_s, which was developed by Brackbill [136] and used in the Ansys Fluent software to consider the impact of surface tension, is the Continuum Surface Force (CSF) acting on the interface between two phases and is discussed in detail in section 2.2.4.3. The VOF model states that only the volume fractions of liquid and vapor are used to calculate the physical properties of a mixture:

$$\rho = \alpha_l \rho_l + \alpha_v \rho_v \tag{2-8}$$

$$\mu = \alpha_l \mu_l + \alpha_v \mu_v \tag{2-9}$$

The energy equation shared by phases is expressed:

$$\frac{\partial(\rho E)}{\partial t} + \nabla.[u(\rho E + p)] = -\nabla.(k\nabla T) + S_q \tag{2-10}$$

where k and E were computed based on the VOF model using the following equations of mixture characteristics:

$$\mathrm{k} = \alpha_l k_l + \alpha_v k_v \quad (2\text{-}11)$$

$$E = \frac{\alpha_l \rho_l C_{p_l} + \alpha_v \rho_v C_{p_v}}{\alpha_l \rho_l + \alpha_v \rho_v} (T - T_{sat}) \quad (2\text{-}12)$$

where k_l and k_v stand for the heat conductivity of liquid and vapor, respectively, and C_{p_l} and C_{p_v} are the specific heats of liquid and vapor, respectively. The energy source term S_q derived from latent heat (h_{lv}) and the mass source term $\dot{m}_{g\to l}$, were used to calculate the heat transfer between phases as:

$$S_{l\to g} = \dot{m}_{g\to l} \quad h_{lv} \quad (2\text{-}13)$$

$$S_{g\to l} = \dot{m}_{l\to g} \quad h_{lv} \quad (2\text{-}14)$$

2.2.4.2 Mass Transfer Model

In the multiphase VOF model, the evaporation-condensation model based on the Lee model [137] was employed to simulate the processes of evaporation and condensation. This model captures mass transfer between liquid and vapor phases along dynamic phases. The continuity and energy equations in the VOF model of the Ansys Fluent software require source terms which were proposed by De Schepper et al [138] in addition to the evaporation-condensation mechanistic model [137]. This model relies on the temperature difference between local temperature and saturation temperature and focused on phase transitions at quasi-thermoequilibrium. Condensation occurs when the local temperature is below the saturation temperature and concerts vapor mass to liquid phase. Evaporation and boiling occur otherwise. The magnitude and direction of mass transfer were defined based on various temperature regimes:

$$\dot{m}_{g\to l} = \begin{cases} C_l . \alpha_l \rho_l (T_l - T_{sat})/T_{sat} & T_l > T_{sat} \\ 0 & T_l \le T_{sat} \end{cases} \quad (2\text{-}15)$$

$$\dot{m}_{l\to g} = \begin{cases} C_v . \alpha_v \rho_v (T_v - T_{sat})/T_{sat} & T_v > T_{sat} \\ 0 & T_v \le T_{sat} \end{cases} \quad (2\text{-}16)$$

Where C_l and C_v are coefficients representing the relaxation time, and $\dot{m}_{l\to g}$ is the rate of mass transfer from the liquid phase to the vapor. The relaxation time coefficients (C_l and C_v) can vary significantly based on the interfacial mass flux. These coefficients are highly dependent on the specific problem, and their ideal values should be determined through experimental validation. In previous studies, values such as 100 or 750,000 [30-32] were used. Extremely low values cause substantial differences between interfacial and saturation temperatures, while very high values can lead to numerical convergence problems. Various parameters, including mesh size, phase-change phenomena, mass flow rate, computational time step size, and experimental conditions, can affect the relaxation time coefficient. In this study, C_l and C_v were chosen as between 50000 and $850000\ s^{-1}$ based on operational conditions, which minimized deviations from experimental results [83] and ensured the rapid observation of droplet condensation.

2.2.4.3 Surface Tension

Surface tension arises from molecular attraction within a fluid, and created a force that balances the pressure gradient across a curved interface. This force minimizes surface free energy by reducing the interface area when one of two separated fluids is not in spherical form. The Young-Laplace equation relates interfacial tension (σ) and equilibrium shape to the pressure difference across the interface:

$$P_{\mathrm{I}} - P_{\mathrm{II}} = \sigma(\frac{1}{r_1} + \frac{1}{r_2}) \quad (2\text{-}17)$$

where orthogonal radii are denoted as r_1 and r_2, with the pressure within the bubble or drop (P_{I})greater than the pressure outside (P_{II}).

The Continuum Surface Force (CSF) model introduced by Brackbill [136] and implemented in the ANSYS FLUENT software, computed surface tension at vapor-liquid interface cells. The force at this interface, acting as a volume force, is incorporated as a source term in the momentum equation using the divergence theorem. The equation for this force (F_s) is given as:

$$F_s = \sigma \frac{\alpha_l \rho_l \kappa_v \nabla \alpha_v + \alpha_v \rho_v \kappa_l \nabla \alpha_l}{\frac{1}{2}(\rho_l + \rho_v)} \quad (2\text{-}18)$$

where σ is the interfacial tension force between the liquid and vapor (in our case $0.0589\ N/m$). The CSF model utilizes local gradients in the surface normal at the interface to calculate the surface curvature. Given that the gradient of volume fraction (α) is defined as the surface normal n,

$$n = \nabla \alpha \quad (2\text{-}19)$$

The unit normal's divergence, $\hat{n} = n/|n|$, is used to define the curvature [136]:

$$\kappa = \nabla . \hat{n} \quad (2\text{-}20)$$

Thus, the curvature for the liquid (κ_l) and vapor (κ_v) phases can be expressed as:

$$\kappa_l = \nabla . \frac{\nabla \alpha_l}{|\nabla \alpha_l|} \quad and \quad \kappa_v = \nabla . \frac{\nabla \alpha_v}{|\nabla \alpha_v|} \quad (2\text{-}21)$$

2.2.4.4 Wall Adhesion

In the VOF model, cells adjacent to the wall have their surface normal adjusted using the wall adhesion angle in conjunction with the surface tension model. This dynamic boundary condition enables the adjustment of interface curvature near the wall. If θ_w is the contact angle at the wall, the surface normal at the cell next to the wall is given as:

$$\hat{n} = \hat{n}_w cos\theta_w + \hat{t}_w sin\theta_w \quad (2\text{-}22)$$

where $\hat{n}_w$ and $\hat{t}_w$ represent the normal and tangential unit vectors to the wall, respectively. The combination of this contact angle with the surface normal located one cell away from the wall yields the local curvature of the surface. This local curvature determines how the surface tension formula adjusts the body force term.

2.2.4.5 Initialization and Convergence Criteria

The simulations were initialized with well-defined initial conditions, such as liquid volume fraction and temperature profiles. Convergence criteria, including residual errors and physical quantities, were monitored during the simulations to ensure precision and reliability. Convergence criteria were set based on the desired level of accuracy and computational resources. In this study, convergence criteria for the continuity, momentum, and volume of fraction equations were set at 10^{-3} , while it was set at 10^{-6} for the energy equation.

2.3 Validation of Simulation Results

FIG 2-4 illustrates the comparison between the numerical results of the model and experimental data of Chehreghani et al [83]. This comparison validates the proposed model, which predicts heat and mass transfer in dropwise condensation for various parameters.
Heat transfer coefficients for hydrophilic, hydrophobic, and superhydrophobic surfaces were considered, at steam mass fluxes ranging from $10\ kg/m^2s$ to $50\ kg/m^2\ s$ and contact angles of $70°, 131°, and\ 172°$, respectively. FIG 2-4 clearly demonstrates that the developed numerical method accurately predicts condensation heat transfer coefficient, with a maximum 10% deviation from experimental data. This prediction is attributed to the effective use of the VOF approach, which ensures comprehensive capture of heat and mass transfer at the interface between water vapor and liquid.

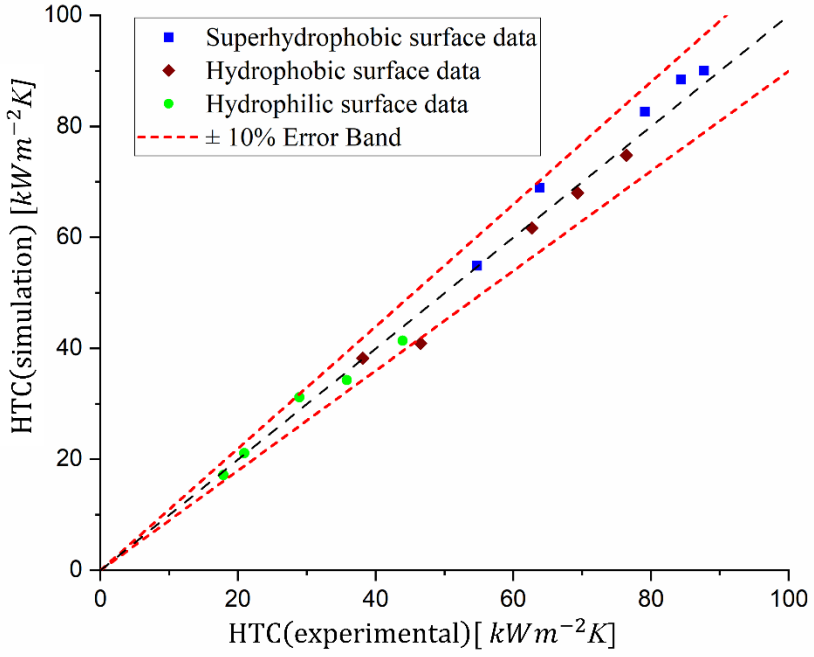

FIG 2-4: Comparison in condensation heat transfer coefficients on various surfaces: numerical calculations of the model and experimental data by Chehrghani et al. [83].

3 RESULTS AND DISCUSSION FOR PLAIN SURFACES

This section explores the effect of different parameters on flow dropwise condensation heat transfer enhancement and provides a comprehensive and parametric study on surface material, wettability, and operating conditions.

3.1 Effect of Steam Mass Flux on Wall Heat Flux

Superhydrophobic surfaces possess properties that promote dropwise condensation by facilitating the formation and easy removal of condensate droplets. The droplet formation and the distribution of wall heat flux for steam mass fluxes (SMF) of $10,20,30,40,50\ kg/m^2\ s$ on the superhydrophobic surface with $\theta = 172°$ are illustrated in FIG 3-1. Droplet formation is illustrated using the iso-surface value $\alpha_L = 0.5$ of the liquid volume fraction.

According to the results, increasing SMF increases wall heat flux, as depicted in FIG 3-1. Two factors contribute to this effect. Firstly, the reduction in droplet size due to increased SMF leads to a thinner thermal boundary layer near the condensing surface, which allows for more efficient heat transfer and contributes to increased wall heat flux. Secondly, the increasing SMF augments shear stresses, which facilitate the easy removal of droplets and further improves heat transfer, as illustrated in FIG 3-1(e).

As shown in FIG 3-1, an increase in steam mass flux leads to a decrease in the average droplet size. This is attributed to the heightened shear force that facilitates the removal of droplets before they can grow larger. The droplet forms and is swiftly eliminated prior to the substantial growth when the inlet mass flux increases to $50\ kg/m^2 s$, as seen in FIG 3-1(a)–(e).

Two opposing forces control droplet removal in flow condensation: the droplet adhesion force (F_{adh}) in the opposite direction and the vapor-droplet shear force (F_{drag}) in the flow direction. The condensed droplet is subject to a vapor shear stress force, which makes droplets move off the surface. The adhesion force needs to be overcome by vapor drag in order to remove the droplets. As a result of the balance between the adhesion and drag force, droplet departure diameter reduces with mass flow rate, as depicted in FIG 3-1(a)-(e). As the mass flow rate and subsequently velocity increase, the drag force increases as shown in this formula:

$$F_{drag} = \frac{1}{2}\rho_v u_v^2 A c_D \tag{3-1}$$

where $\rho_v\ and\ u_v$ represent the vapor density and velocity, respectively, and A is the frontal area of the deformed droplet. c_D is the drag coefficient that depends on the droplet shape. As the droplet shape is deformed by the contact angle, c_D depends on the contact angle. According to Minle et al. [139], the adhesion force exerted on a liquid droplet of any shape is expressed as:

$$F_{adh} = k\sigma(\cos\theta_{max} - \cos\theta_{min})L_b \quad (3\text{-}2)$$

where $(\cos\theta_{max} - \cos\theta_{min})$ is the hysteresis contact and L_b is the droplet bases length; and k is the defined parameter that takes the irregular and deformed geometries of the liquid droplet into account in addition to consideration of a variety of contact angles. Superhydrophobic surfaces exhibit a low contact angle hysteresis, which enables easy droplet sliding. However, at low velocities, droplets move, develop, expand, and coalesce slowly, as depicted in FIG 3-1(a). Higher vapor velocity promotes droplet removal and continuous dropwise condensation, as shown in FIG 3-1(e).

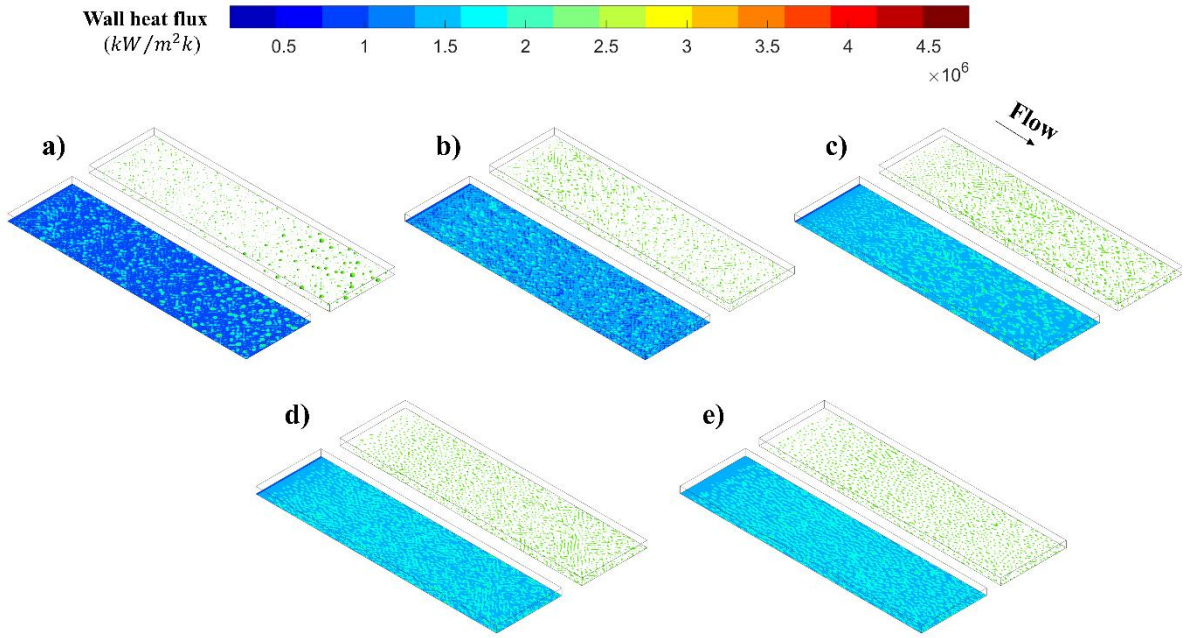

FIG 3-1 Iso-surface of $\alpha_L = 0.5$ and wall heat flux distribution on superhydrophobic surfaces at $t = 0.5\ s$ for various steam mass fluxes: a) SMF10, b) SMF20, c) SMF30, d)SMF40, e)SMF50 kg/m^2s

FIG 3-2 shows droplet formation and wall heat flux distribution on hydrophobic surfaces with $\theta = 131°$ at various inlet steam mass fluxes. At low steam mass flux ($SMF = 10\,kg/m^2$), the droplets are difficult to be removed due to drag force reduction, which leads to coalescence and the formation of larger droplets and results in increased thermal resistance and poor wall heat flux (FIG 3-2(a)). Considerable heat flux is observed at specific locations where droplets exist. Similar to superhydrophobic surfaces, FIG 3-2 shows that increased SMF reduces the droplet size and improves the removal frequency due to the increased shear force. However, droplets on hydrophobic surfaces are larger compared to superhydrophobic surfaces. Additionally, the wall heat flux is lower on hydrophobic surfaces. Utilizing superhydrophobic surfaces can boost wall heat flux by up to 88% compared to the hydrophobic surfaces.

As the flow velocity increases, overall condensation rate intensifies compared to low-velocity conditions, which causes more small liquid droplets on the surface and leads to a more even distribution of wall heat flux.

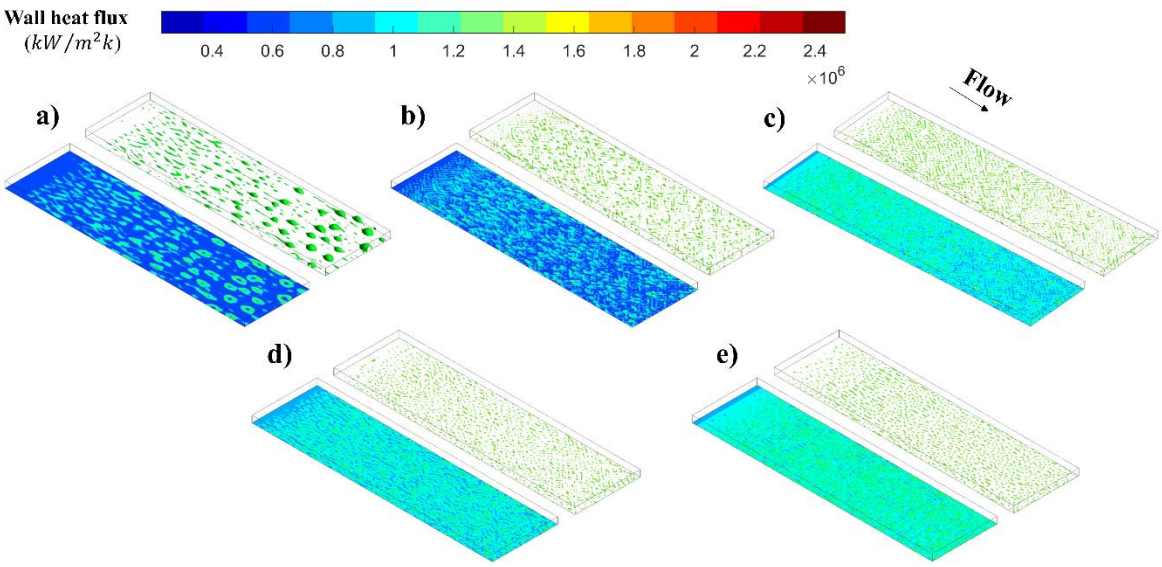

FIG 3-2 Iso-surface of $\alpha_L = 0.5$ and wall heat flux distribution on hydrophobic surfaces at $t = 0.5\ s$ for various steam mass fluxes: a) SMF10, b) SMF20, c) SMF30, d)SMF40, e)SMF50 $kg/m^2\ s$

Using the iso-surface value $\alpha_L = 0.5$ of the liquid volume fraction and corresponding temperature distribution, the liquid droplet evolution during condensation is displayed in FIG 3-3 (for a superhydrophobic surface at $SMF = 10\ kg/m^2 s$ and $\theta = 172°$ at mid-plane). The droplet begins to nucleate in direct contact of hot vapor with the cold surface, as shown in FIG 3-3(a) (red circle). Then, droplets approach one another and begin to coalesce. This happens both in a perpendicular direction to the flow (FIG 3-3(b)) and in the direction of the flow (FIG 3-3(c)), which generates a larger droplet. Red circle in FIG 3-3(b) displays a large droplet grew due to coalescences of two neighboring droplets in the perpendicular direction to the flow. Following this, the droplet coalesces with the several nearby droplets in the flow direction, and it further enlarges, as shown with blue box in FIG 3-3(c). Then, droplets begin to sweep, which creates space for the nucleation in the following condensation cycle. Coalescence is a critical aspect as it triggers the formation of larger droplets, which are more prone to shedding from the surface. This shedding of droplets enhances heat transfer efficiency by preventing the accumulation of a continuous water film, which promotes a cycle of nucleation and condensation. Finally, the resulting combined droplet elongates vertically due to the reaction force raised from the surface.

In FIG 3-3, the temperature distribution aligns with the steps of droplet evolution depicted by the iso-surface. It illustrates the coalescence of small droplets, their enlargement, and the subsequent cleaning in a surface for new nucleation cycle. Notably, in FIG 3-3 (b), where coalescence occurs perpendicular direction to the flow, the resulting merged droplet is obscured in the corresponding temperature distribution. It becomes visible in FIG 3-3 (c) as it enlarges through coalescence in the flow direction.

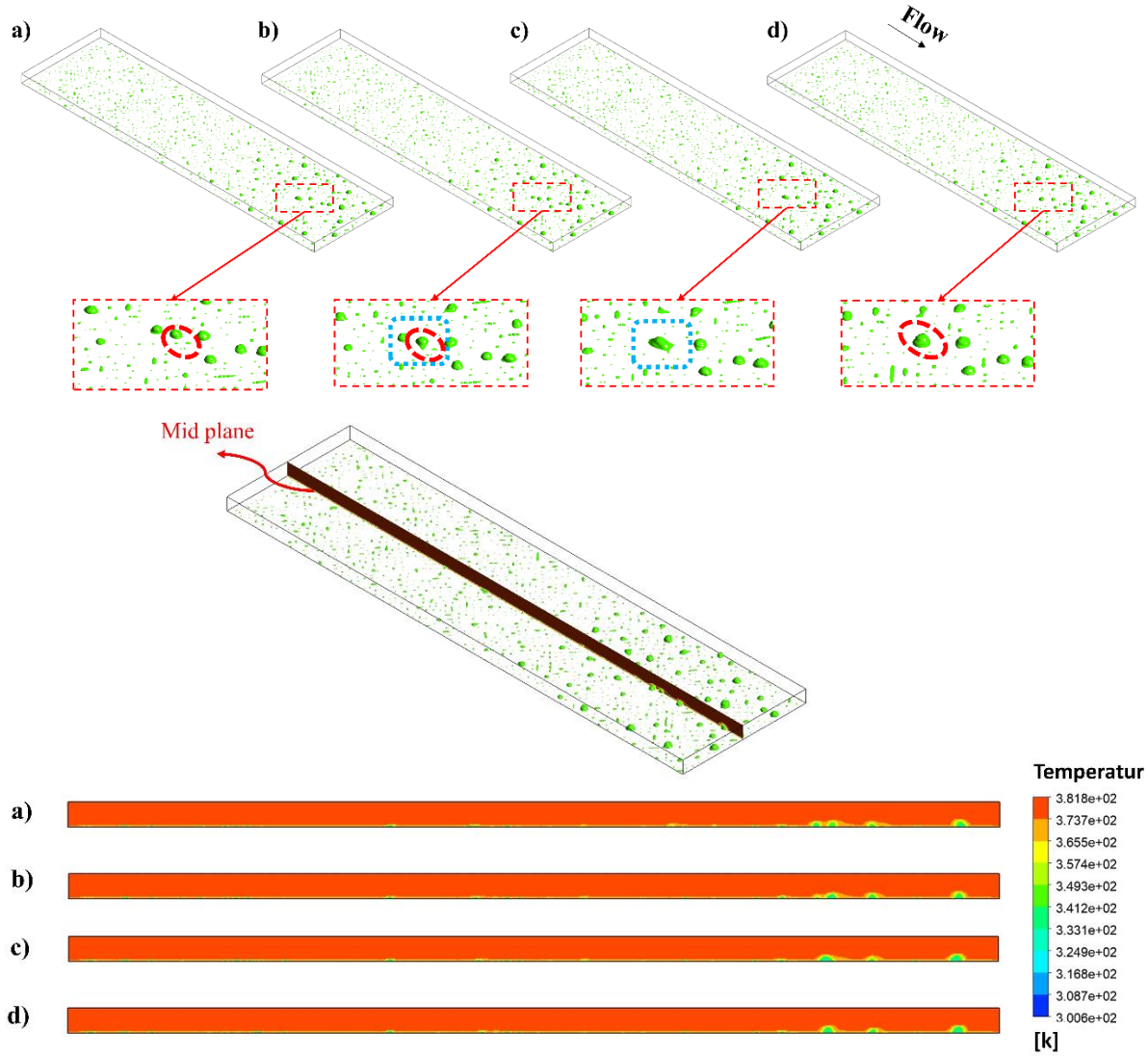

FIG 3-3 Iso-surface of $\alpha_L = 0.5$ and temperature distribution of droplet evolution on the superhydrophobic surface at SMF 10 kg/m^2s in successive time steps: a) Droplet growth, b) Droplet coalescence in the mid-plane in the perpendicular direction to the flow direction, c) Droplet coalescence in the mid plane in the flow direction, d) Droplet rise up in the mid-plane in the flow direction

FIG 3-4 discusses dropwise condensation on hydrophobic surfaces with the contact angle of $\theta = 131°$ in terms of temperature distribution and droplet growth using iso-surface of $\alpha_L = 0.5$ at SMF 10 kg/m^2s. Red circle in FIG 3-4(a) depicts the start of the nucleation. In FIG 3-4(b), the droplets begin merging as adjacent ones make contact. Similar to the superhydrophobic surfaces, coalescence occurs in both the flow direction (FIG 3-4(b)) and the perpendicular direction to the flow direction (FIG 3-4(d)). However, larger droplets form through coalescence on hydrophobic surfaces compared to the superhydrophobic ones.

In FIG 3-4(b), two droplets get closer in the flow direction. In FIG 3-4(c), resulting combined large droplet can be seen (red circle). FIG 3-4(d) depicts subsequent coalescence perpendicular to the flow direction, which demonstrates how a droplet can undergo multiple coalescence during its growth until reaching the departure radius. The blue box in FIG 3-4(d) illustrates droplet shedding resulting from coalescence, thereby clearing the space for subsequent

nucleation cycle.

For the hydrophobic surface, the temperature distribution related to iso-surface is presented in FIG 3-4, which depicts the stages of the growth, coalescence, and shedding. The smallest droplet, undergoing growth, is initially positioned nearby the largest droplet in FIG 3-4(a). Coalescence initiates in the flow direction in FIG 3-4 (b) as condensation progresses. In FIG 3-4(c), a small droplet disappears due to coalescence, and a larger droplet form. FIG 3-4(d) illustrates the continued expansion of the merged large droplet through coalescence perpendicular to the flow direction, which involves another hidden droplet in FIG 3-4(c). Eventually, the resulting large droplet becomes invisible in the temperature contours upon exiting the mid-plane. This process of coalescence and re-nucleation repeats alternately until the large droplet reaches its maximum departure size. Besides, when comparing the droplet motion on hydrophobic (FIG 3-4) and superhydrophobic surfaces (FIG 3-3), it is evident that the motion of droplets is more visible on hydrophobic surfaces.

These observations highlight the importance of three-dimensional numerical studies for understanding the dropwise condensation process that is crucial for optimizing heat transfer.

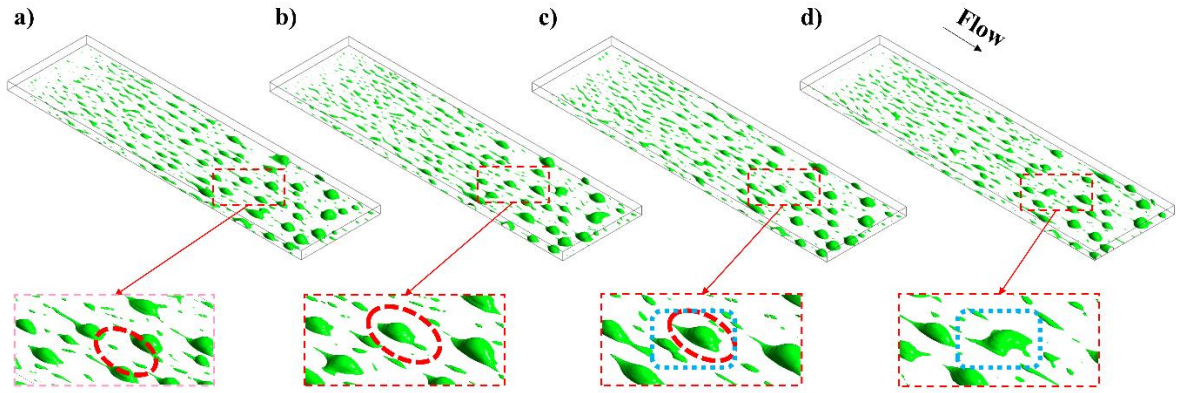

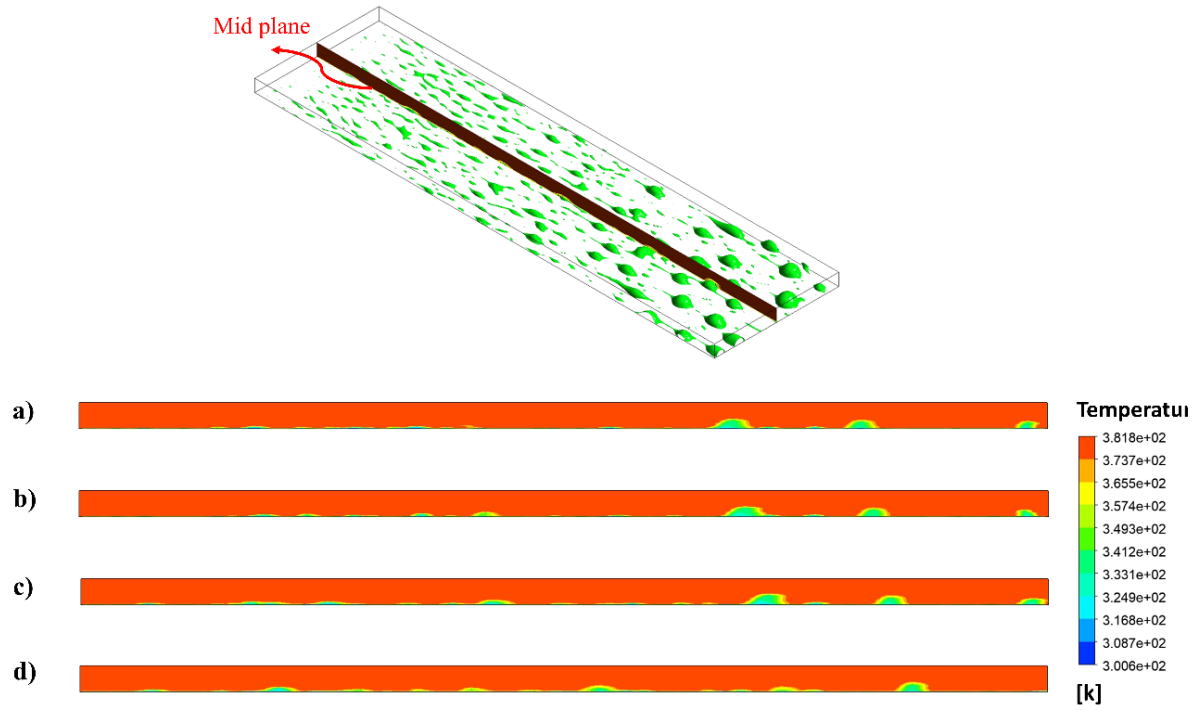

FIG 3-4 Droplet evolution on hydrophobic surface for SMF 10 kg/m^2s in successive time steps: a) Droplet growth, b) Droplet coalescence in the mid-plane in the flow direction, c) Droplet raise-up in the mid-plane in the flow direction, d) Droplet coalescence in the mid-plane perpendicular to the flow direction

Dropwise condensation is a cyclic procedure, encompassing droplet nucleation, growth, coalescence, and departure. Investigating of this cycle serves as a valuable tool for characterizing the condensation phenomenon. To compare the dropwise condensation performance of hydrophobic and superhydrophobic surfaces, FIG 3-5 and FIG 3-6 illustrate condensation cycles with stages of nucleation (stage I), growth (stage II), coalescence (stage III), and departure (stage IV). In this analysis, τ represents the full cycle period.

Regarding the superhydrophobic surface, FIG 3-5 depicts a comparison between the numerical simulations results and the available experimental results of a complete cycle for dropwise condensation at a steam mass flux of 10 kg/m^2s in a previous study [83]. At stage I, the droplet nucleation begins. A number of factors such as the temperature and wettability of the surface, the hydrothermal characteristics of vapors, and the amount of non-condensable gas present in the vapor flow influence the droplet nucleation rate. The stages II and III correspond to the growth of the droplet as a consequence of continued vapor condensation. Also, the further droplet growth caused by the calescence of the nearby tiny droplets can be seen in FIG 3-5 via blue and red circles (stage II and stage III). Later, the vapor drag force overcomes the adhesion force. Upon reaching a critical size, the droplets slide down while cleaning the surface and exposing it to vapor, as shown by green box (stage IV).

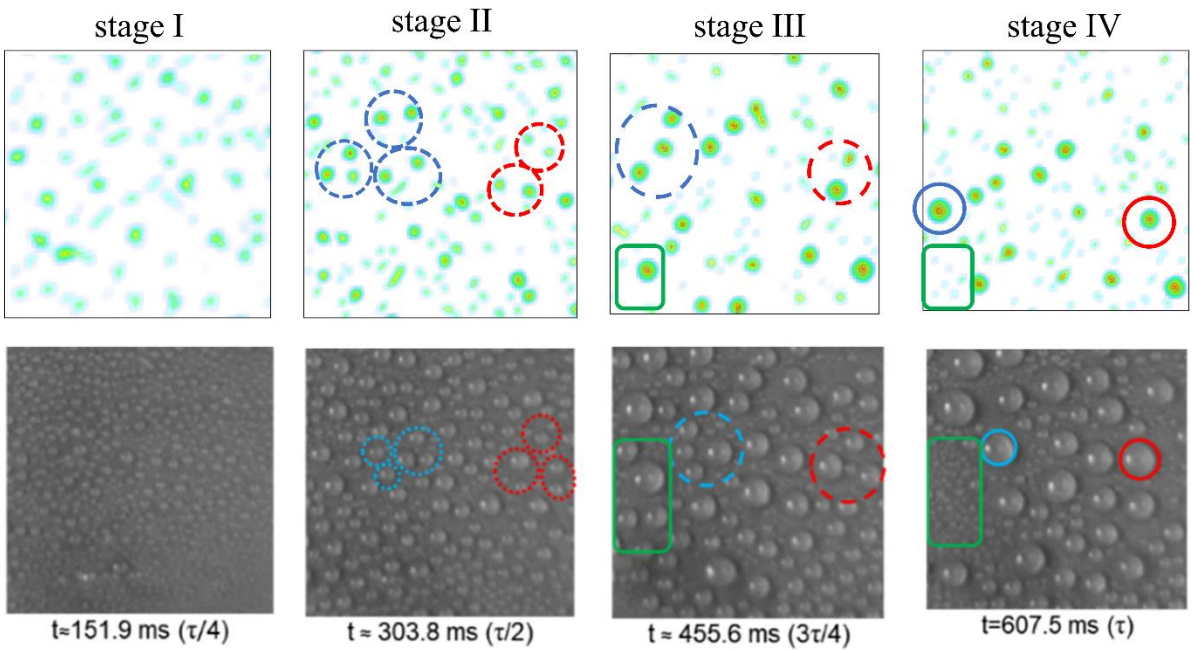

FIG 3-5 Comparison of numerical and experimental [83] visualization of droplets evolution on the superhydrophobic surface at steam mass flux (SMF) of 10 kg/m^2s at different time steps

FIG 3-6 presents a comprehensive analysis of dropwise condensation on a hydrophobic surface by comparing experimental results [83] with numerical simulation results under the same conditions. The stage I, similar to the superhydrophobic surface, depicts the initial nucleation of droplets on the hydrophobic surface. The distribution of droplet sizes at this stage suggests that the hydrophobic surface experiences a faster droplet coalescence than the superhydrophobic surface, which results in larger droplets on the hydrophobic surface. However, a more uniform droplet size distribution is offered by the superhydrophobic surface, shown in FIG 3-5. The performance of heat transfer is adversely affected by the spreading of large droplets over the hydrophobic surface, which acts as a thermal resistance. As time progresses to the stage II, both the experimental and simulated results reveal a certain growth pattern and distribution of droplets.

The stage III represents a critical point in the droplet cycle, which is associated with the departure of droplets from the surface. Unlike the superhydrophobic surface, the droplet departure time varies noticeably for different droplets on the hydrophobic surface. Even though droplets in green box are forced away from the surface by shear force, in the stage IV, several droplets (red circle) are still attached to the surface.

While droplets on the hydrophobic surface grow more quickly, their cycle duration is longer than those on the superhydrophobic surface. At the end of the cycle, the droplets on the hydrophobic surface are significantly larger because of the increased surface wettability. Until the vapor shear rate becomes high enough to separate the droplets from the hydrophobic surface, the droplets usually keep expanding on the surface. Larger droplets are more likely to leave the surface, but smaller droplets may also leave from hydrophobic and superhydrophobic surfaces (as indicated by the green box in FIG 3-6) as a result of two neighboring droplets coalescence. Because of the vapor shear rate and released surface energy, some smaller droplets (in comparison to the droplet diameter at the final stage of the cycle) could become

sufficiently mobile to escape from the surface. Under the same conditions, the results of the numerical simulations are in good agreement with the experimental results related to the flow patterns observed during the experiments. This suggests that the model is reasonable and trustworthy and it can be used to predict the droplet dynamics in flow condensation on various surfaces.

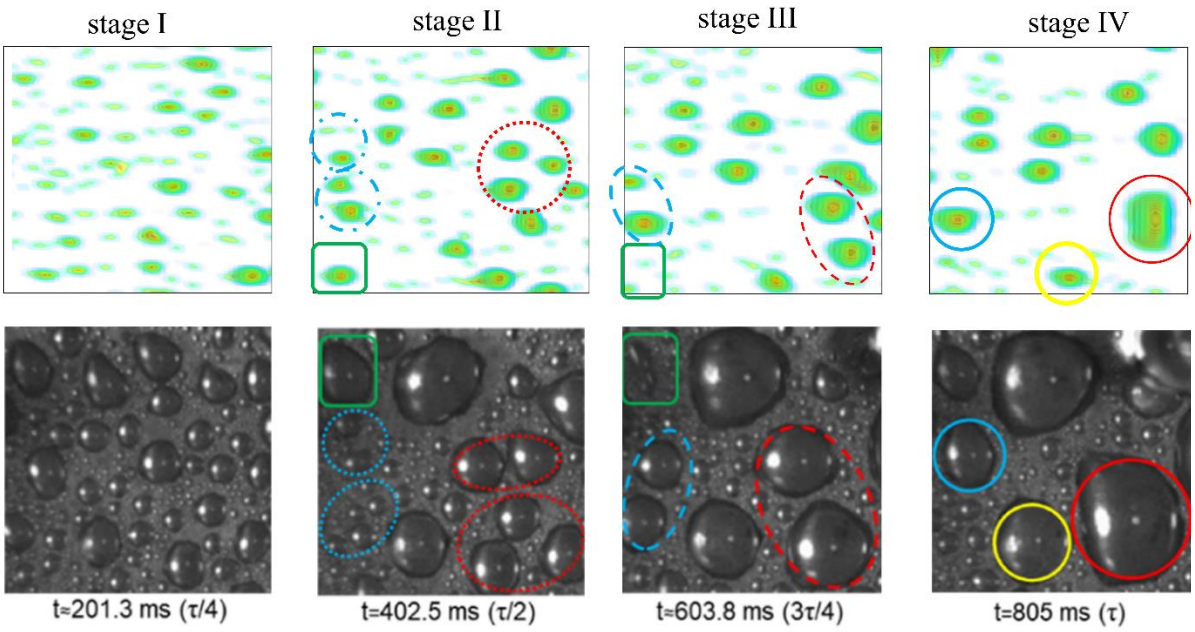

FIG 3-6 Comparison between numerical and experimental [83] results on droplet evolution on the hydrophobic surface at the steam mass flux (SMF) of 10 kg/m^2s and different time steps

The comparison between simulation and experimental results of dropwise condensation on a superhydrophobic and hydrophobic surfaces for a range of SMF is presented in FIG 3-7. Interestingly, the size of the droplets on the superhydrophobic surface consistently decreases with increasing steam mass flux. Upon an increase in steam mass flux, the vapor shear rate makes the droplets leave the surface more quickly.

FIG 3-7 shows the effect of the steam velocity on the droplet departure radius. The mean droplet departure radius decreases with the mass flux. As demonstrated in FIG 3-7, an increase in the steam mass flux (SMF) from 10 to 20 kg/m^2s results in a significant reduction in the size of the leaving droplets at the end of the condensation cycle. When the SMF approaches 30 kg/m^2s, the difference becomes much more noticeable. The droplet departure size decreases with increasing steam mass flux, however beyond this SMF (40 and 50 kg/m^2s), this effect diminishes.

This trend is also observed on the hydrophobic surface (FIG 3-7). Despite the larger droplet sizes, the higher surface energy of this surface makes it more difficult for droplets to detach, even though the vapor shear rate is greater.

The model accurately depicts the reduction in the droplet size, which confirms its validity as shown in FIG 3-7. This highlights the influence of mass flux on droplet distribution on superhydrophobic and hydrophobic surfaces.

As the droplet size decreases, heat transfer coefficient increases. Thus, strategies to reduce the droplet size will be useful for enhancing dropwise flow condensation heat transfer.

Particularly, the maximum departure radius needs to be decreased.

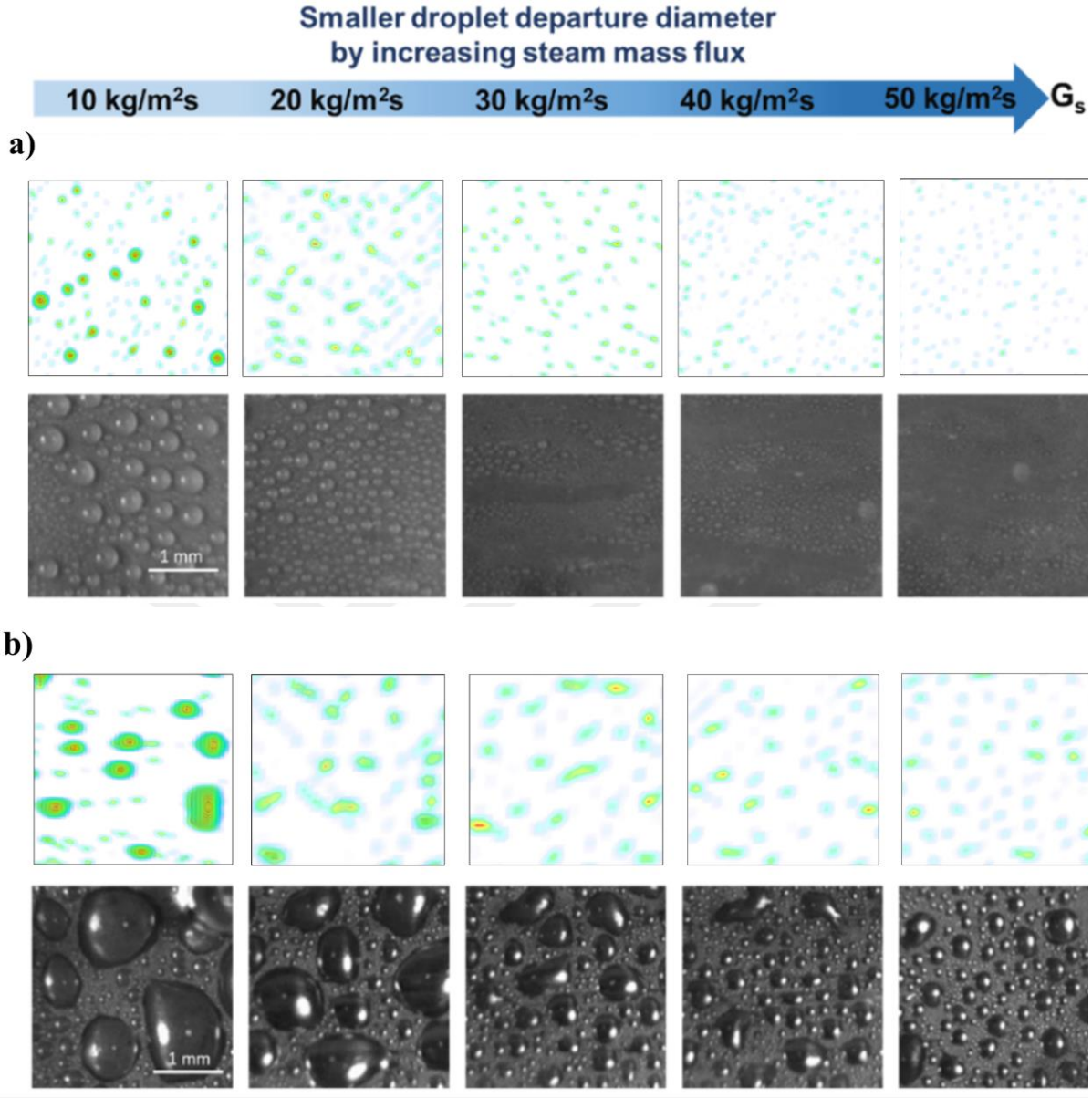

FIG 3-7 Comparison between numerical and experimental [83] results on droplet distribution at different steam mass fluxes at the end of the dropwise condensation cycle a) superhydrophobic and b) hydrophobic surfaces

3.2 Droplet distribution on superhydrophobic surface

The droplet distribution histogram constructed in the cycles of simulations of dropwise condensation on hydrophobic and superhydrophobic surfaces using the software ImageJ provides a comprehensive understanding of the periodic evolution of droplet dynamics. The analysis was conducted at four different time instants, which offers a detailed examination of how droplet distribution changes during the condensation process. Importantly, these simulations cover a wide range of inlet steam mass fluxes, which makes it possible to compare

the performance of hydrophobic and superhydrophobic surfaces under different operating conditions.

FIG 3-8(a) illustrates the droplet distribution on a superhydrophobic surface throughout a cycle of dropwise condensation at the steam mass flux SMF 10 kg/m^2s. This histogram shows a predominance of small droplets at the first time instant, revealing the beginning of nucleation on the superhydrophobic surface. This early stage is crucial for understanding how effectively the surface promotes droplet formation, which is a key factor for efficient heat transfer. At subsequent time instant in FIG 3-8(a), the number of tiny droplets (less than $100\mu m$) decreases and the number of larger droplets increases, indicating the evolution of droplet size through coalescence.

The distribution is influenced by coalescence and shedding mechanisms throughout time, as seen in the third and final period in FIG 3-8(a). While the quantity of small droplets decreases over time until the cycles completion at the end of the cycle in FIG 3-8(a), the creation of new droplets due to direct condensation is shown as the beginning of a new cycle. By the end of the cycle, droplets reach their maximum size and leave, thereby creating space for new nucleation in the subsequent condensation cycle. This leads to a slight increase in the number of droplets less than $100\ \mu m$ at the cycle completion instance for all steam mass fluxes. The droplet distribution histogram effectively displays the performance of the superhydrophobic surface in terms of size and number of droplets. Smaller droplets consistently grow at each time instant on the superhydrophobic surface, which indicates effective shedding and shorter contact times.

Furthermore, the effect of steam mass flux on droplet distribution was investigated. Designing surfaces for the most possible heat transfer enhancement is limited to maintenance of performance under different mass flux conditions. It is apparent that an increase in the vapor mass flux leads to a decrease in the droplet departure radius, as depicted in FIG 3-8, which results in an increase in the heat transfer coefficient (HTC).

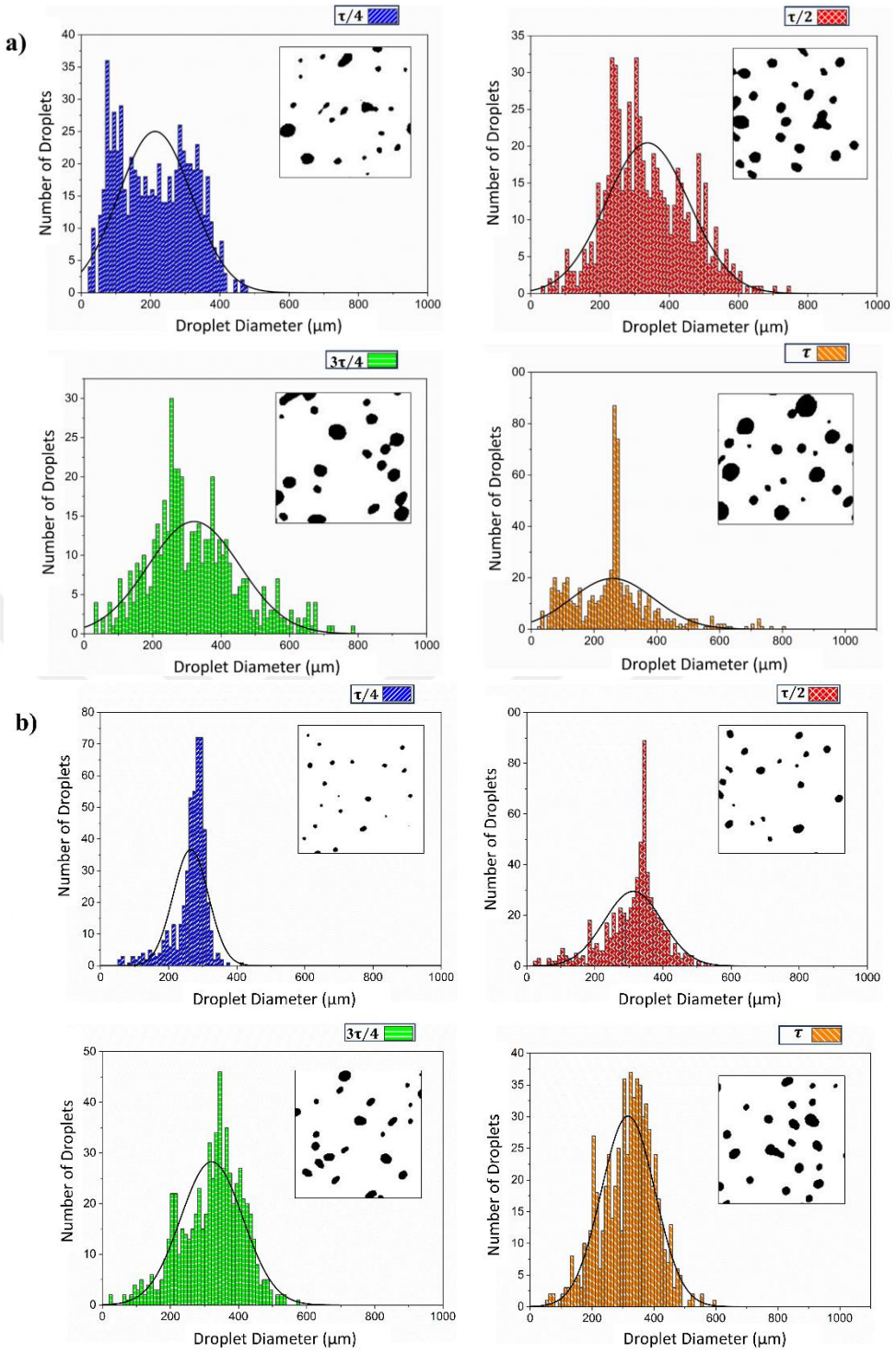
a)
τ/4
τ/2
3τ/4
τ
b)
Number of Droplets
Droplet Diameter (μm)

c)

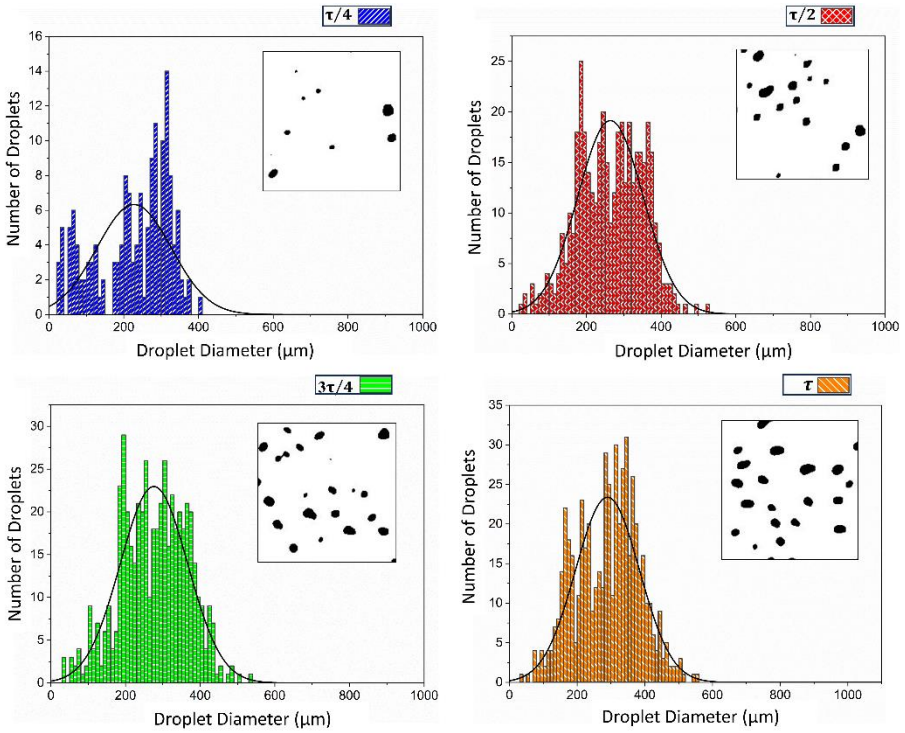
τ/4
τ/2
3τ/4
τ
Number of Droplets
Droplet Diameter (μm)

d)

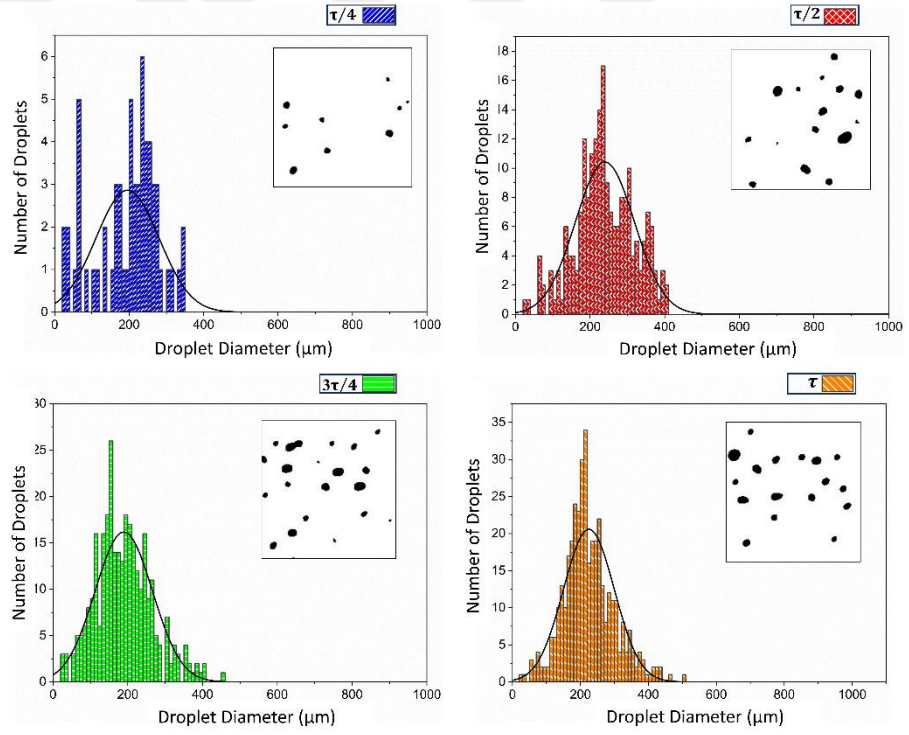
τ/4
τ/2
3τ/4
τ
Number of Droplets
Droplet Diameter (μm)

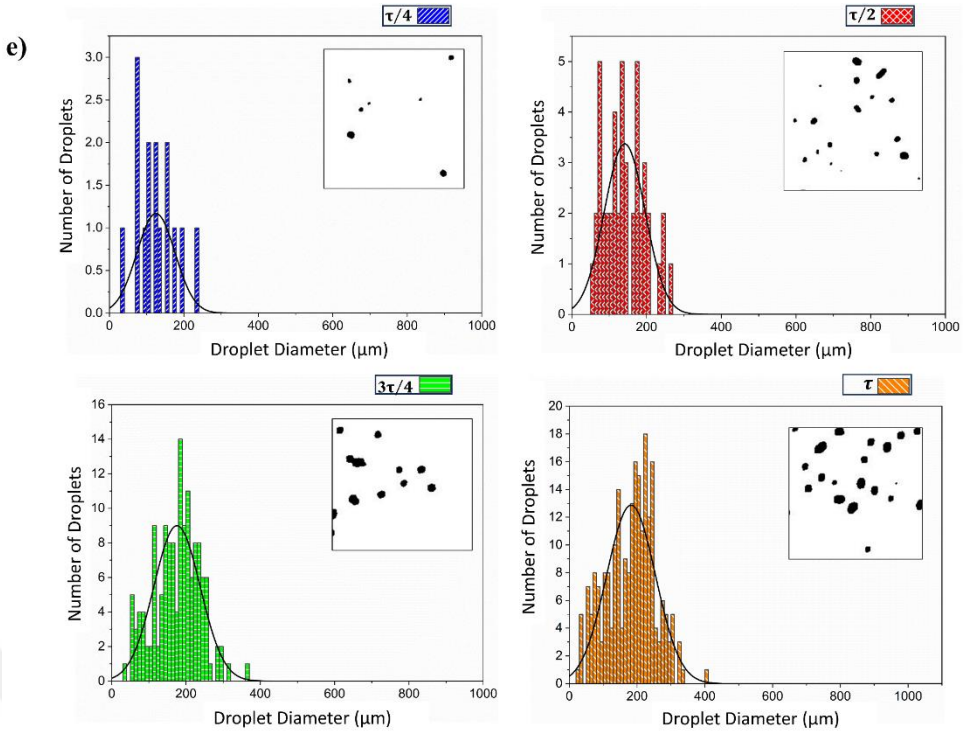

FIG 3-8 Droplet distribution histogram for the superhydrophobic surface at a range of steam mass fluxes: a) 10 kg/m^2s, b) 20 kg/m^2s, c) 30 kg/m^2s, d) 40 kg/m^2s, e) 50 kg/m^2s

3.3 Droplet distribution on hydrophobic surface

FIG 3-9 illustrates the droplet distribution during a cycle of dropwise condensation on the hydrophobic surface at different steam mass fluxes ranging from 10 $kg/m^2\,s$ to 50 $kg/m^2\,s$. As can be seen in FIG 3-9, at the initial time instant, the histogram for the hydrophobic surface has a distribution of larger droplets which is consistent with the inherent nature of hydrophobic surfaces. In contrast to this surface, the superhydrophobic surface has a large number of smaller droplets, which is indicative of its enhanced ability to facilitate dropwise condensation. As time progresses, the hydrophobic surface continues to promote larger droplets through coalescence, while the superhydrophobic surface keeps having mostly small droplets (FIG 3-8), which reflects efficient shedding for this surface.

When examining the effect of steam mass flux on droplet distribution, it can be seen that higher mass fluxes intensify condensation, which influences the size and density of droplets. However, it's noteworthy that the droplet departure size decreases on both surfaces with steam mass flux.

The comparison in the droplet distribution histograms for hydrophobic and superhydrophobic surfaces at each period enables a direct evaluation of their performances. The superhydrophobic surface's ability to maintain a higher number of small droplets of different mass fluxes shows its superiority in promoting effective dropwise condensation (shown in FIG 3-8). In contrast, the hydrophobic surface consistently leads to a distribution of larger droplets, which indicates its inclination towards film condensation.

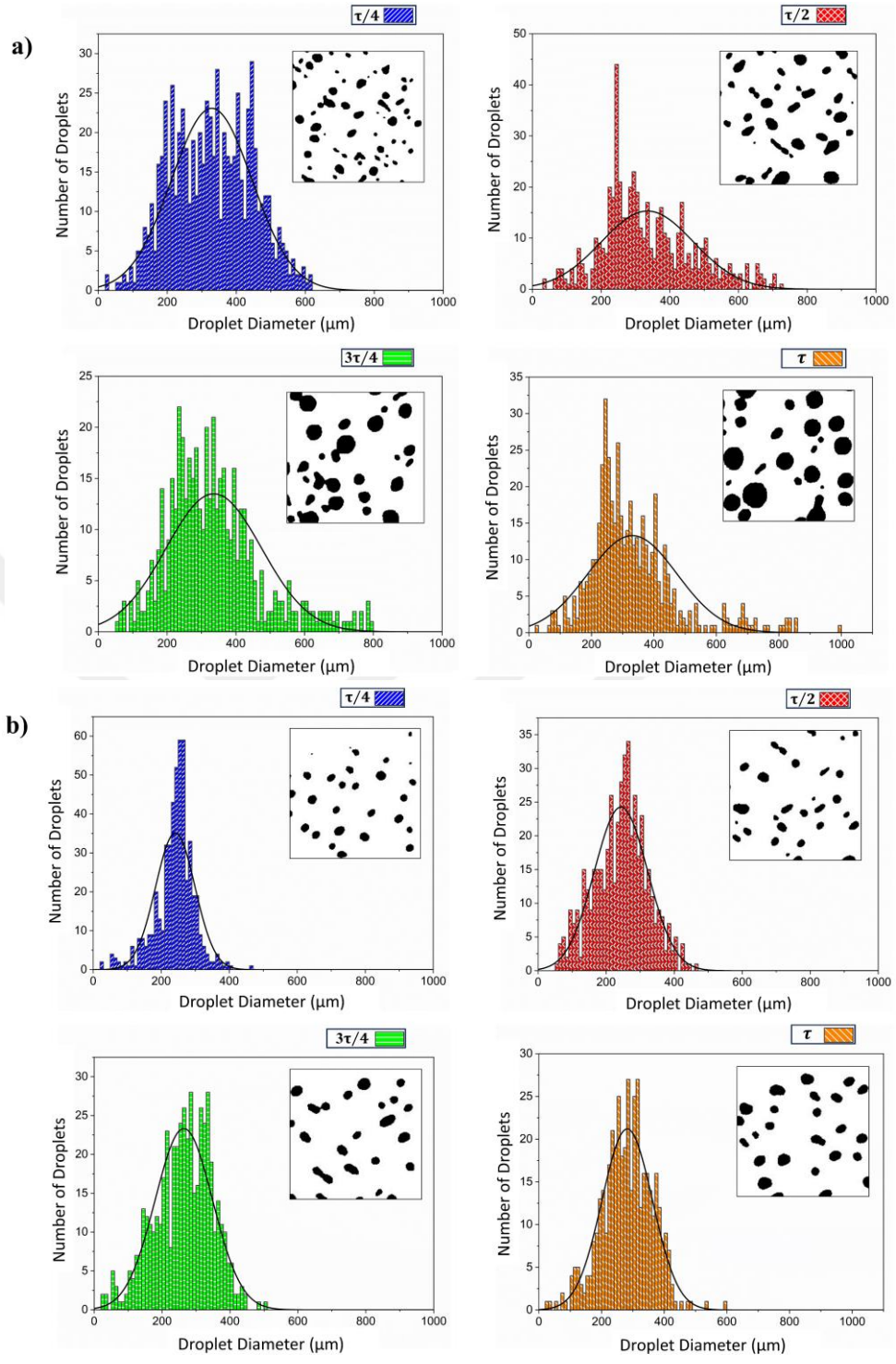
a)
τ/4
τ/2
3τ/4
τ
Number of Droplets
Droplet Diameter (μm)
b)
τ/4
τ/2
3τ/4
τ
Number of Droplets
Droplet Diameter (μm)

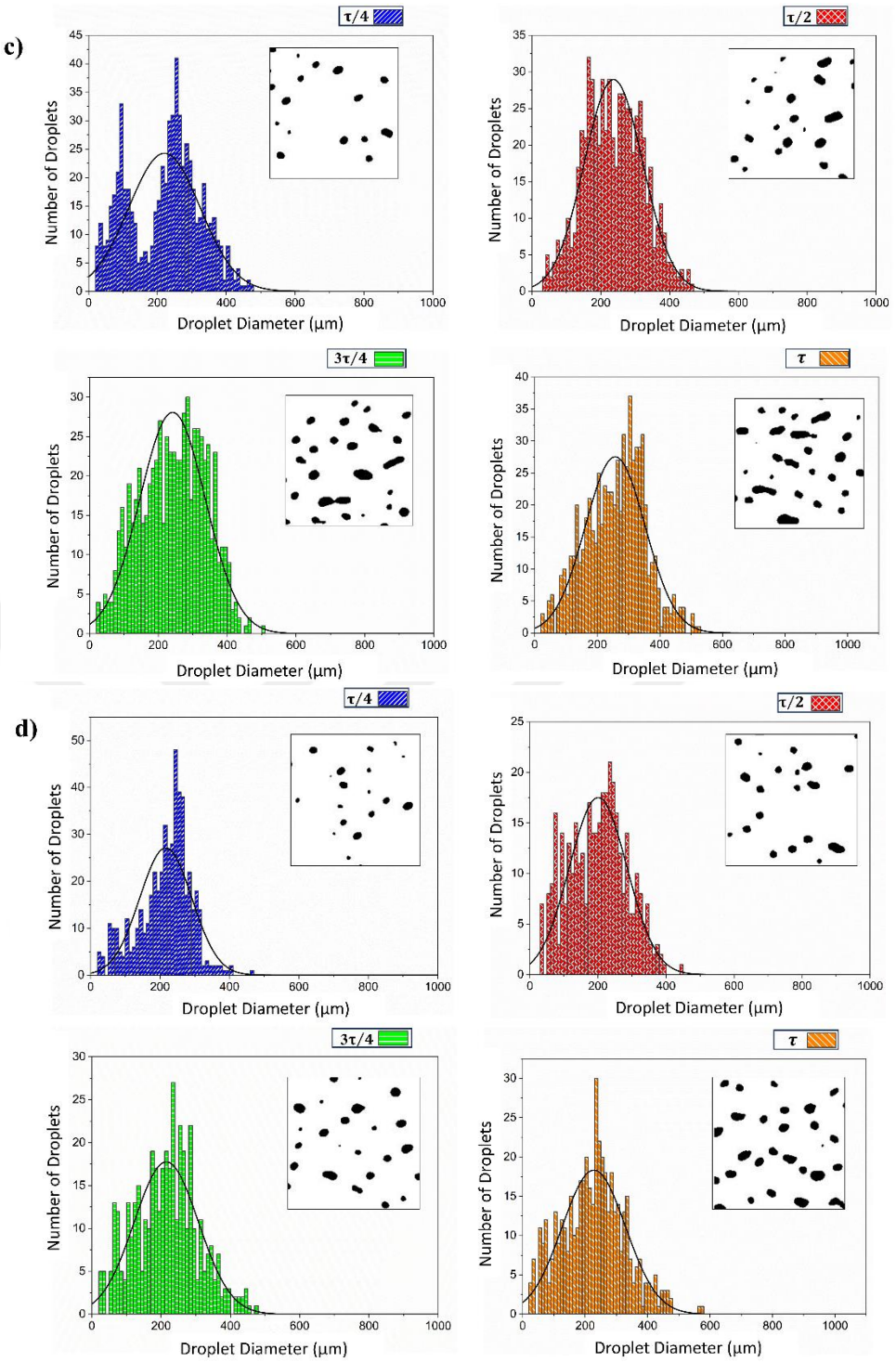
c)
τ/4
τ/2
3τ/4
τ
Number of Droplets
Droplet Diameter (μm)
d)
τ/4
τ/2
3τ/4
τ
Number of Droplets
Droplet Diameter (μm)

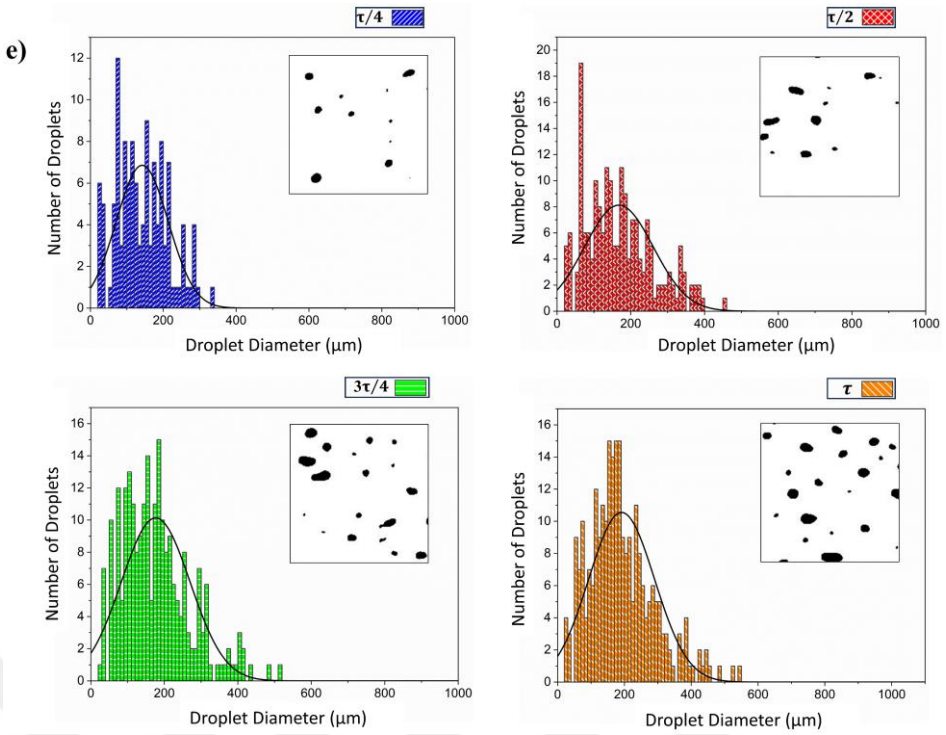

FIG 3-9 Droplet distribution histograms on the hydrophobic surface at different steam mass fluxes: a) 10 kg/m^2s, b) 20 kg/m^2s, c) 30 kg/m^2s, d) 40 kg/m^2s, e) 50 kg/m^2s

3.4 Effect of Material on Heat Transfer Coefficient

In this section, the effects of contact angle, surface material, and steam mass flux on dropwise condensation were examined, and five steam mass flux values of $10, 20, 30, 40, 50$ $kg/m^2\,s$ were considered. Copper, aluminum, and steel are commonly used materials. Thus, three distinct materials, copper, aluminum, and steel, were taken into consideration in order to further analyze how material properties such as thermal conductivity (k), heat capacity (c_p), and density (ρ) affect the heat transfer coefficient and droplet sizes. High thermal conductivity of copper promotes effective condensation, which enables heat to be transferred away from the surface quickly. Aluminum is lightweight and has good thermal conductivity but is not as effective as copper in terms of heat conduction. Steel, while robust, has a low contact angle, which impacts the formation and shedding of droplets.

As seen in FIG 3-10, the copper surface provides a larger heat transfer coefficient (HTC) than the others and less HTC on steel surfaces in all scenarios. This might be the result of steel having a lower thermal diffusivity ($\alpha_{steel} = k/\rho c_p = 4e-6$) and copper having a higher thermal diffusivity ($\alpha_{copper} = k/\rho c_p = 1e-4$). ANSYS FLUENT utilizes the thermal resistance of the wall ($\Delta x/k$) to calculate heat transfer within it. The thermal resistance is determined by the ratio of wall thickness (Δx) to the thermal conductivity of the material (k). Since the wall thickness remains constant in all scenarios, the thermal conductivity of the surface material plays a significant role in heat transfer.

Table 3-1 Material properties of the surface

	copper	steel	aluminum
Density,ρ $[kg/m^3]$	8978	8030	2719
Thermal conductivity, k $[W/(m\,k)]$	387.6	16.27	202.4
Heat capacity, c_p $[J/(kg\,k)]$	381	502.48	871

To expand the study to explore the impact of wettability on heat transfer, three contact angles were considered: 70°, 131°, and 172°, which correspond to hydrophilic (Hphi), hydrophobic (Hpho), and superhydrophobic (Shpho) surfaces, respectively. FIG 3-10 exhibits an increase in the heat transfer coefficient with an enhanced contact angle. This trend remains consistent for all materials, including the coefficient is low for the steel surface showing less variation. Notably, the heat transfer coefficient increase is the largest for hydrophilic surfaces, as evident in the case of copper.

An increase in mass flow rate impacts the heat transfer coefficient (HTC) in two ways. Firstly, it increases the steam velocity, which leads to increased shear stress and reduces condensate thickness. Secondly, there is a rise in momentum transfer between steam and condensate liquid. As a result, the heat transfer coefficient increases with increasing mass flow rate, which agrees with findings in Chehrhghani et al.'s study [83].

In FIG 3-10, HTC increased by 90% on the copper hydrophobic surface while the increase is 60% on the copper superhydrophobic surface upon an increase in the steam mass flux from 10 to 50 $kg/m^2\,s$. Steel surfaces consistently have low HTC, but copper superhydrophobic surfaces cause a larger HTC attributed to their thermal properties.

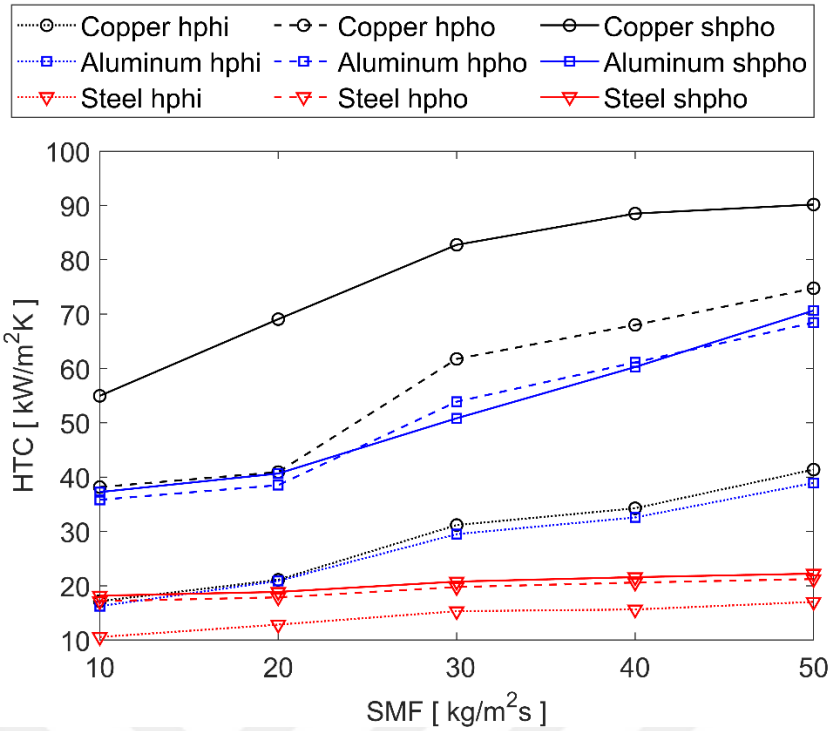

FIG 3-10: The effect of steam mass flux, surface material properties, and wettability on heat transfer coefficient (HTC)

FIG 3-11 displays the impact of wettability on the maximum droplet size (departure size). In this case, by the vapor drag force acting on the droplet, which is proportional to the fluid velocity and the droplets' frontal area is critical.

FIG 3-10 illustrates how superhydrophobic surfaces, which outperform hydrophobic and hydrophilic surfaces, significantly improve dropwise condensation. These surfaces exhibit exceptional water-repelling characteristics, typically characterized by high contact angles. Considering the expression $h = r(1 - cos\theta)$, it becomes apparent that, for a droplet with an identical radius, the height is greater at a larger contact angle, leading to an increased drag force on the droplet. This enhanced drag force contributes to an increase in droplet height and a reduction in the contact area with the surface. As depicted in FIG 3.11, the superhydrophobic surface denotes a greater droplet height compared to hydrophobic surfaces. Furthermore, FIG 3.11 clearly displays the correlation between heat transfer coefficient and droplet departure size.

As SMF varies from 10 to 20 $kg/m^2\,s$, noticeable variations in droplet size occur on the superhydrophobic surface. Subsequently, an increase in SMF from 20 to 30 $kg/m^2\,s$ results in a significant reduction in droplet size, as depicted in FIG 3-11(a). Beyond this point, changes in SMF have no further impact on droplet size, which aligns with the results in FIG 3-7(a).

For the hydrophobic surface, droplet size consistently decreases with an increase in SMF. Hydrophobic surfaces have departure droplet sizes larger than superhydrophobic surfaces at high SMF. Steel surfaces lead to larger droplet sizes in every scenario.

As the steam mass flux (SMF) and vapor velocity increase, the drag force intensifies, which causes a decrease in the droplet departure height on the steel superhydrophobic surface from 172 to 15 μm, as depicted in FIG 3-11(a). There is an obvious connection between small

droplet sizes and high heat transfer coefficient (HTC). This is attributed to the fact that the thermal resistance of a droplet rises with an increase in size. Hence, smaller droplets are advantageous for achieving a higher heat transfer coefficient (HTC).
Depending on the particular application, having higher SMF is one of approaches that can improve the heat transfer coefficient (HTC) in dropwise condensation (DWC). While HTC benefits from higher SMF, it comes at the expense of a larger pressure drop.

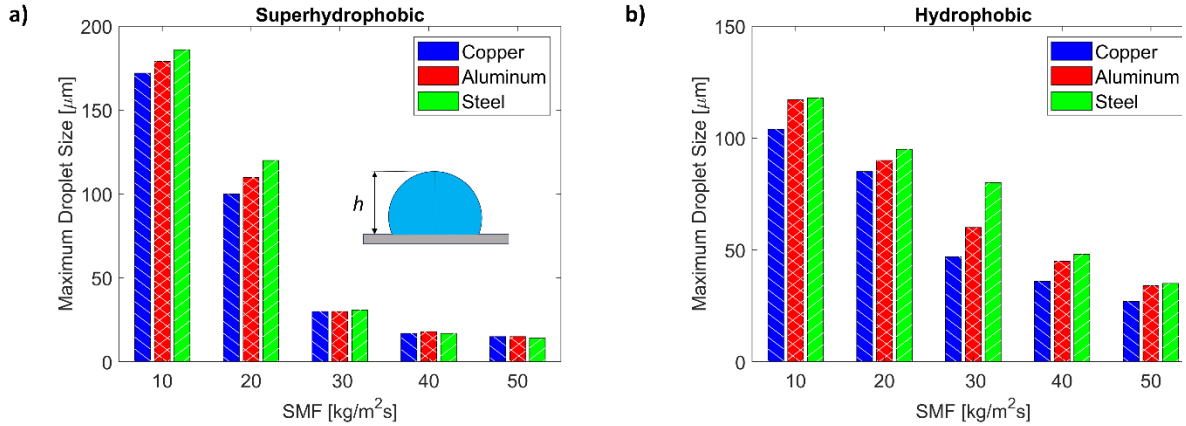

FIG 3-11 Maximum droplet size variation of different materials with the stam mass flux (SMF) on : a) superhydrophobic surfaces and b) hydrophobic surfaces

3.5 Effect of Subcooled temperature

As depicted in FIG 3-12, an increase in temperature difference between vapor and cooling wall enhances heat transfer coefficient through dropwise condensation on both hydrophobic and superhydrophobic surfaces. Our simulations encompass three distinct materials: copper, aluminum, and steel.
FIG 3-12 shows that subcooled temperature exhibits less effect on steel superhydrophobic surface in comparison to other instances, but the overall trend of heat transfer enhancement is the same in all cases. This can be attributed to the less thermal conductivity of the steel.
FIG 3-12 can be divided into three sections. The first section, characterized by a temperature differential of less than $40°C$, exhibits a small slope. This is attributed to the low rate of condensation and droplet formation. Additionally, the condensation rate is noticeably low in this section for both hydrophobic and superhydrophobic surfaces due to the small temperature difference and weak driving force. In the context of low subcooled temperatures, the impact of the contact angle on the heat transfer coefficient is insignificant.
In the second section, upon an increase in temperature difference, a higher number of droplets form on the surface. This leads to an enhancement of the condensation rate and surface renewal. Consequently, the slope of heat transfer coefficient becomes larger, particularly within the temperature difference range of 40 and $60°C$.
In the third section, a higher subcooled temperature leads to a sharp increase in the heat transfer coefficient. As can be seen in FIG 3-12, superhydrophobic surfaces reveal a more significant increase in heat transfer coefficient (HTC) compared to hydrophobic surfaces. It is evident that the heat transfer coefficient is influenced not only by subcooled temperature but also by

surface characteristics and thermal properties. Copper and aluminum, sharing similar thermal characteristics, have closely aligned heat transfer coefficient (HTC) values on the superhydrophobic surface. FIG 3-12 clearly illustrates the relationship among HTC, contact angle, and subcooled temperature. Accordingly, copper superhydrophobic surfaces, which possess higher contact angles and thermal properties, under greater subcooled temperature condition show superior heat transfer coefficients (HTC).

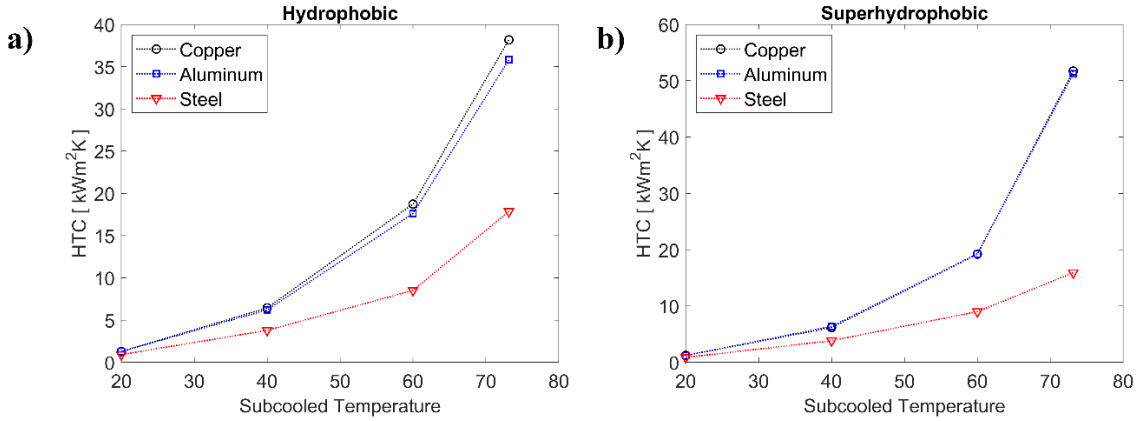

FIG 3-12 Effect of subcooled temperature on heat transfer coefficient with various materials of a) hydrophobic surfaces, and b) superhydrophobic surfaces

3.6 Effect of contact angle on heat transfer coefficient

One of the crucial factors influencing condensation heat transfer is surface wettability, which is characterized by the contact angle. FIG 3-13 shows the impact of contact angle on the heat transfer coefficient for various surface materials at steam mass flux of 10 $kg/m^2\,s$.

FIG 3-13 can be split to three sections. The first section includes hydrophilic surfaces with contact angles between 70° and 90°, having water-attracting characteristics that tend to have smaller contact angles. In this portion of the plot, the heat transfer coefficient (HTC) varies at the highest rate compared to the other sections, nearly doubling. This could be attributed to the influence of contact angle and its relationship with droplet size, which consequently affects the drag force.

The second section involves hydrophobic surfaces with contact angles ranging from 90° and 150°. The variation in the heat transfer coefficient is less pronounced compared to the other sections. HTC slightly increases, and the overall heat transfer coefficient in this section is lower than that of the superhydrophobic section but higher than that of the hydrophilic surfaces.

The third section belongs to superhydrophobic surfaces with contact angles between 150° and 172°. In this section, an increase in contact angle consistently leads to a higher heat transfer coefficient (HTC). Our simulation results indicate that a larger contact angle is preferable for achieving a higher condensation heat transfer.

Steel surfaces display a significant variation in heat transfer coefficient with hydrophilic characteristics, but this variation becomes insignificant afterwards. In contrast, copper and aluminum surfaces exhibit similar behavior with contact angle. However, in line with earlier

findings, copper consistently demonstrates superior heat transfer coefficients.

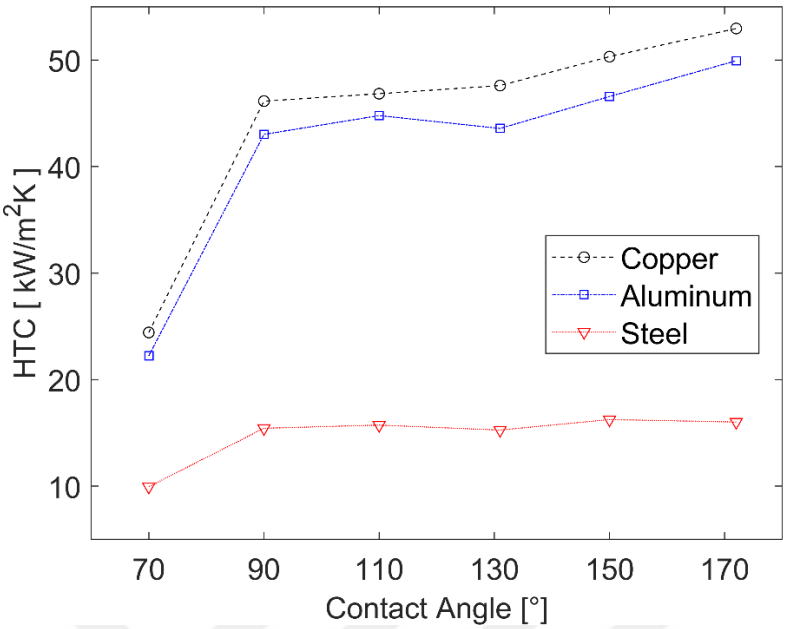

FIG 3-13 Contact angle effect on heat transfer coefficient on surfaces with different material at SMF 10 kg/m^2s

FIG 3-14 displays a comparison between the numerical simulation results and a well-known theory for a droplet on a surface for various material including copper, aluminum, and steel. It is generally known that the ratio of droplet wet length to droplet height at various contact angles on solid surfaces in the equilibrium state is determined as $D/h = 2sin\theta/(1 - cos\theta)$ [140]. The simulation results as shown in FIG 3-14 illustrate that the ratio of droplet wet length to droplet height at various contact angles can well match with the theoretical predictions for all cases.

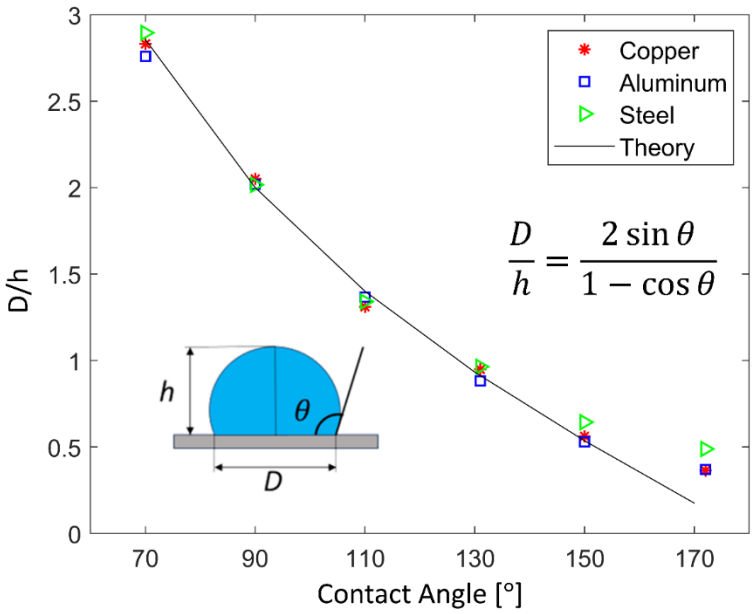

FIG 3-14 Comparison of numerical results with the theory [140] on various surfaces with changing the contact angle.

FIG 3-15 demonstrates that droplet mobility during dropwise condensation is influenced by contact angle. Droplets enlarge from the nucleation to the departure size as a result of a balance between forces that make droplets move (gravity and drag) and retentive forces (droplet adhesion). In our studies, where the surface is horizontally oriented, the adhesion force and vapor shear stress counteract, leading to the continuous sweeping and renewal of the surface. The retentive force is solely dependent on the droplet size, not on its position on the surface, since wettability is uniform throughout the surface.

At a low contact angle, the droplet makes continuously move as it grows via vapor condensation and coalescence with neighboring droplets, as depicted in FIG 3-15(a). As the contact angle increases, mobility significantly decreases compared to hydrophilic surfaces. In FIG 3-15(b)-(c), it can be observed that the droplet, begins to move during growth from nucleation until reaching a specific location where adhesion force outweighs the drag force. At this point, the droplet remains at a fixed position until drag force surpasses adhesion force, which makes the droplet resume movement. On hydrophobic surfaces, the droplet moves more rapidly than on superhydrophobic ones.

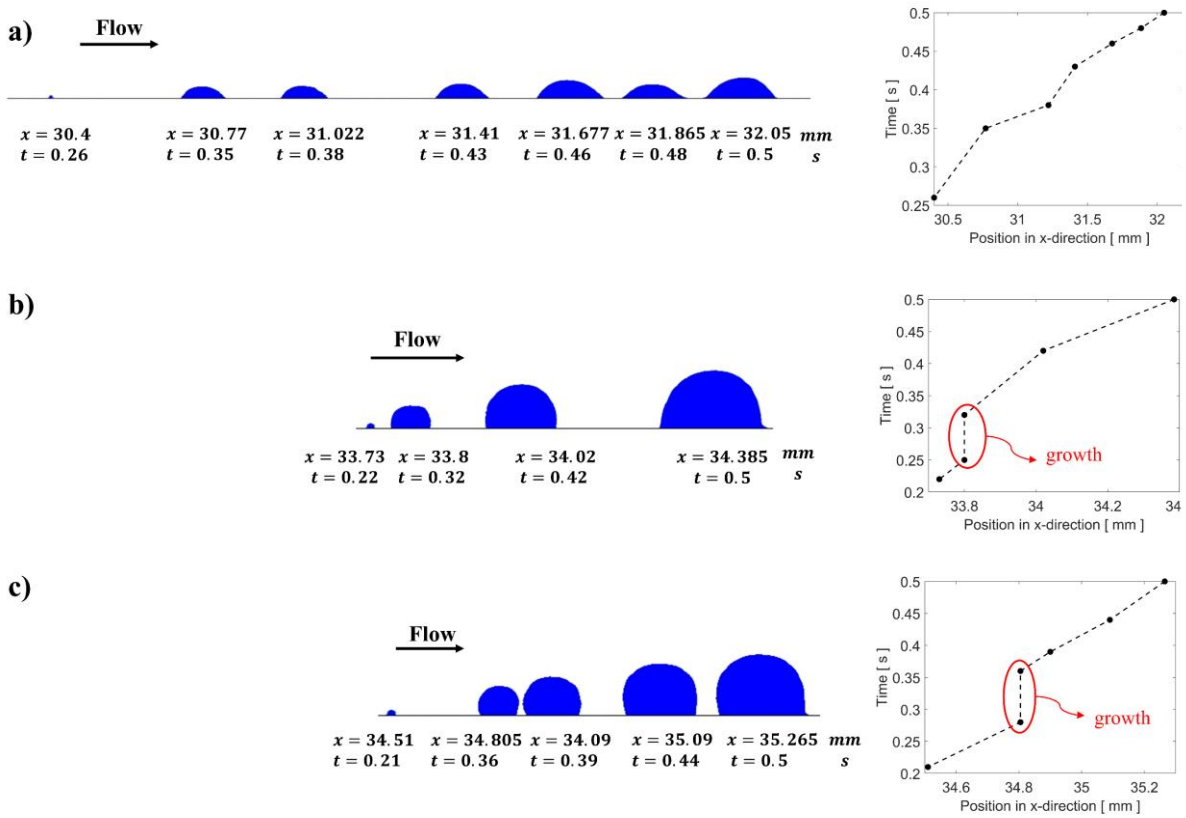

FIG 3-15 Droplet motion at different instants on the aluminum surface for various contact angles: a) $\theta = 70°$, b) $\theta = 131°$ c) $\theta = 172°$

4 RESULTS AND DISCUSSION FOR FUNCTIONAL SURFACES

In this chapter, the results of the numerical analysis on heat transfer in flow condensation on biphilic surfaces within a minichannel were presented. Two different designs were developed by altering the wettability contrast between the surface pattern and the substrate. In the first design, the region surrounding the patterns is superhydrophobic, while the patterns themselves are hydrophobic. The main objective is to enhance the DWC rate. In the alternate scenario, the substate is also superhydrophobic, but the patterns are hydrophilic. This second design aimes to benefit from the advantageof FWC. A parametric study was conducted to identify optimum designs in each case, by varying both pattern size (D) and steam mass flux (SMF). Pattern sizes of 300 ,$700,$ and 900 μm and SMF of $10, 20, 30$ $kg/m^2\,s$ were considered.
The computational domain, mesh , structure, and boundary conditions utilized in this chapter are illustrated in FIG 4-1. The computational domain includes a mass flow inlet, a pressure outlet, symmetry, and a wall boundary condition as a patterned cooling surface, depicted in FIG 4-1. Gravity acts in the Y direction. The patterned surface consists of a copper superhydrophobic substrate with a thickness of 0.5 mm and 150 nm chromium patterns, while the pattern size is denoted as D. The entire domain has dimensions of 37×1 mm, as shown in FIG 4-1. The cooling wall maintains a constant subcooled wall temperature.

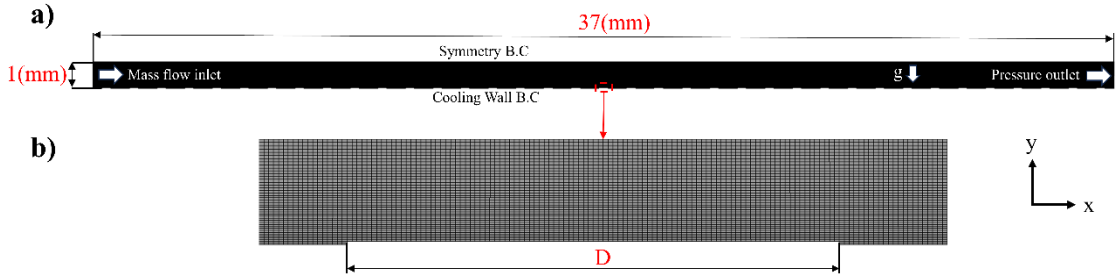

FIG 4-1 a) schematic of the design, b) Computational domain, mesh and boundary conditions used for the biphilic surfaces. The 'D' value indicates the surface pattern size in micrometers; for instance, 'D700' stands for a biphilic surface with hydrophobic size of 700 micrometers.

As discussed in the previous chapter, dropwise condensation on rough superhydrophobic surfaces leads to higher heat-transfer rates compared to dropwise condensation on smooth hydrophobic surfaces. Nevertheless, superhydrophobic surfaces have poor individual droplet growth rates because of their severe apparent advancing contact angles, which limits the overall performance. Also, the efficiency of heat transfer would be hindered by the high thermal resistance and huge nucleation energy barrier under the Cassie-state condensate drops on superhydrophobic surfaces. Moreover, improperly designed superhydrophobic surfaces might trap droplets in a strongly pinned Wenzel state, leading to undesired flooding condensation under high supersaturation conditions. Careful design, optimization of geometry

and wettability, will enable effective condensation heat transfer on a single surface. Our numerical study provides design guidelines for biphilic surface development, which aims to enhance condensation heat transfer. FIG 4-2 compares our simulation results with the experimental data from the literature [117], which demonstrates on a good agreement (within a 20% $discripancy$) for biphilic surfaces.

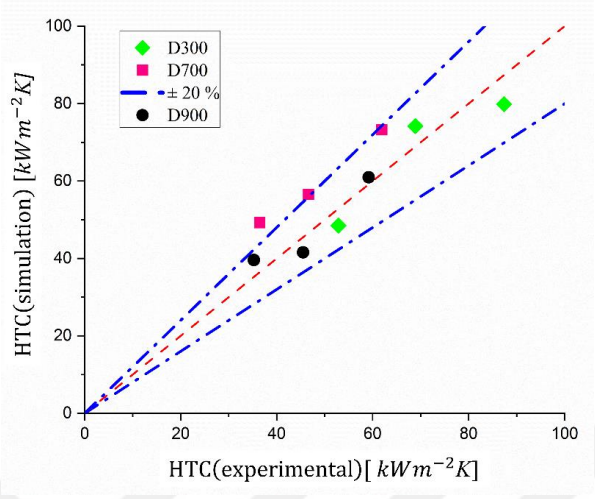

FIG 4-2 Validation of the numerical heat transfer coefficients with the heat transfer coefficient measured by Chehrghani et al [117].

4.1 Condensation flow pattern and droplet distribution for hydrophilic spots

A present study was conducted to assess the effect of wettability contrast on dropwise condensation and droplet distribution. Dropwise condensation across the entire channel were investigated on three distinct hydrophobic patterned surfaces (D300, D700, and D900) at steam mass fluxes of 10,20, and 30 $kg/m^2\,s$, as shown in FIG 4-3 to FIG 4-5 .

FIG 4-3 depicts the vapor volume fraction contours of a horizontal copper substrate with hydrophobic patterns (D300) at three different cross sections ($0-3\,mm$, $17-20\,mm$, and $34-37\,mm$) and steam mass fluxes (SMF) of $10,20, and\ 30\ kg/m^2s$. Condensed liquid forms on the cooling wall due to the temperature difference between the high-temperature vapor and encountering the cold wall surface. As shown in FIG 4-3, there is minimum accumulation of liquid droplets at the entrance section of the wall in all cases where the shear force surpasses inertial forces. FIG 4-3(a)-(c) reveals that an increase in SMF leads to a higher number of uniformly distributed little droplets across the entire wall. Resembling the behavior observed on uniform superhydrophobic surfaces, the droplet size diminishes with increasing SMF. Thus, the largest droplet size appears at the lower SMF of 10 kg/m^2s, as can be seen in FIG 4-3(a). Moreover, larger droplets form consistently on hydrophobic patterned regions in all scenarios, due to droplet´s tendency to move from lower to higher surface free energy.

The patterned surface enhances the frequency of droplet removal, which is attributed to two factors. First, shedding occurs at a smaller droplet size due to low wettability characteristics of the superhydrophobic surfaces; on superhydrophobic surfaces, condensate droplets can spontaneously depart via coalescence-induced jumping or self-propelled droplet jumping, thereby creating tremendous potential for improved heat transfer by rapidly refreshing cold

superhydrophobic surfaces. Second, higher wettability on hydrophobic surfaces leads to more frequent vapor condensation, which keeps superhydrophobic surfaces cleaner and boosting heat transfer. The phenomenon of droplet jumping is demonstrated in FIG 4-3, where the height of jumped droplets is greater at SMF 10 kg/m^2s (FIG 4-3(a)). The size and frequency self-propelled jumping droplets decrease with SMF.

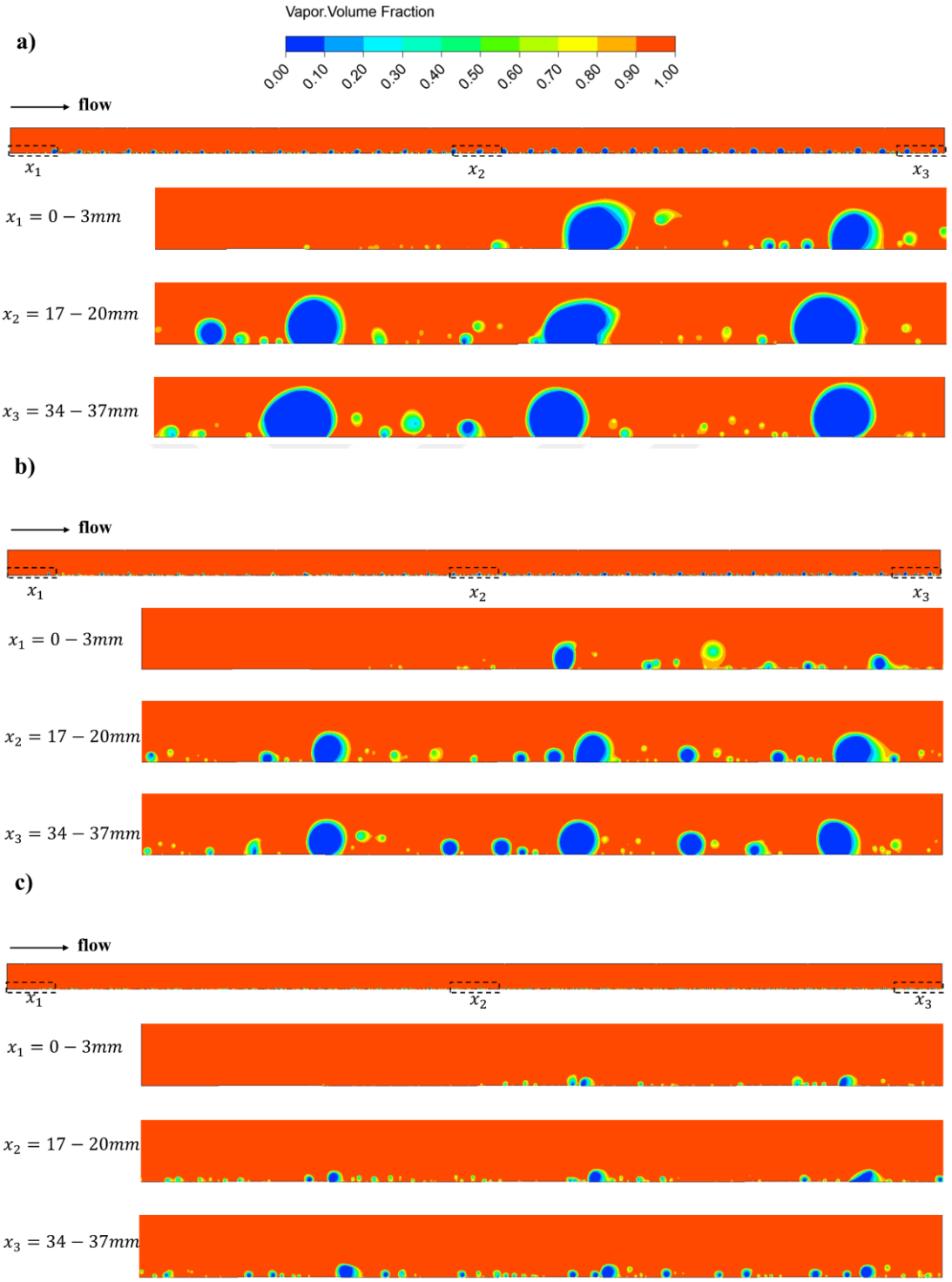

FIG 4-3 Vapor volume fraction contour of the biphilic surface with hydrophobic pattern of D300 at $t = 0.5s$ at different cross-sections of the computational domain for various steam mass fluxes: a) SMF 10; b) SMF 20, c) SMF 30 $kg/m^2\ s$

The efficiency of condensation on biphilic surfaces is significantly influenced by the ratio of hydrophobic to superhydrophobic regions. In this context, this ratio is increased by reducing the superhydrophobic region, by changing the pattern size to $700\mu m$. The distribution of vapor volume fraction at different steam mass flux (SMF) for biphilic surface with the pattern size of $700\mu m$ (D700) is shown in FIG 4-4. Similar to D300 biphilic surfaces, the condensate droplets do not accumulate at the entrance section of the channel, owing to the shear force dominating the inertial forces. In comparison to D300 biphilic surface, there is a decrease in droplet-jumping frequency on the D700 biphilic surface (especially as SMF increases), due to a reduced area of superhydrophobic surface. As SMF increases, the droplets become smaller. The FIG 4-4(c)) reveals a more even distribution of a larger number of small droplets at high SMF. In contrast to D300 biphilic surfaces, the larger droplets are not confined to the hydrophobic zones, which demonstrates the mobility of droplets on D700. These mobile droplets can result in liquid bridging between patterns that they can also migrate across the channel as can be seen in the first section in FIG 4-4(a).

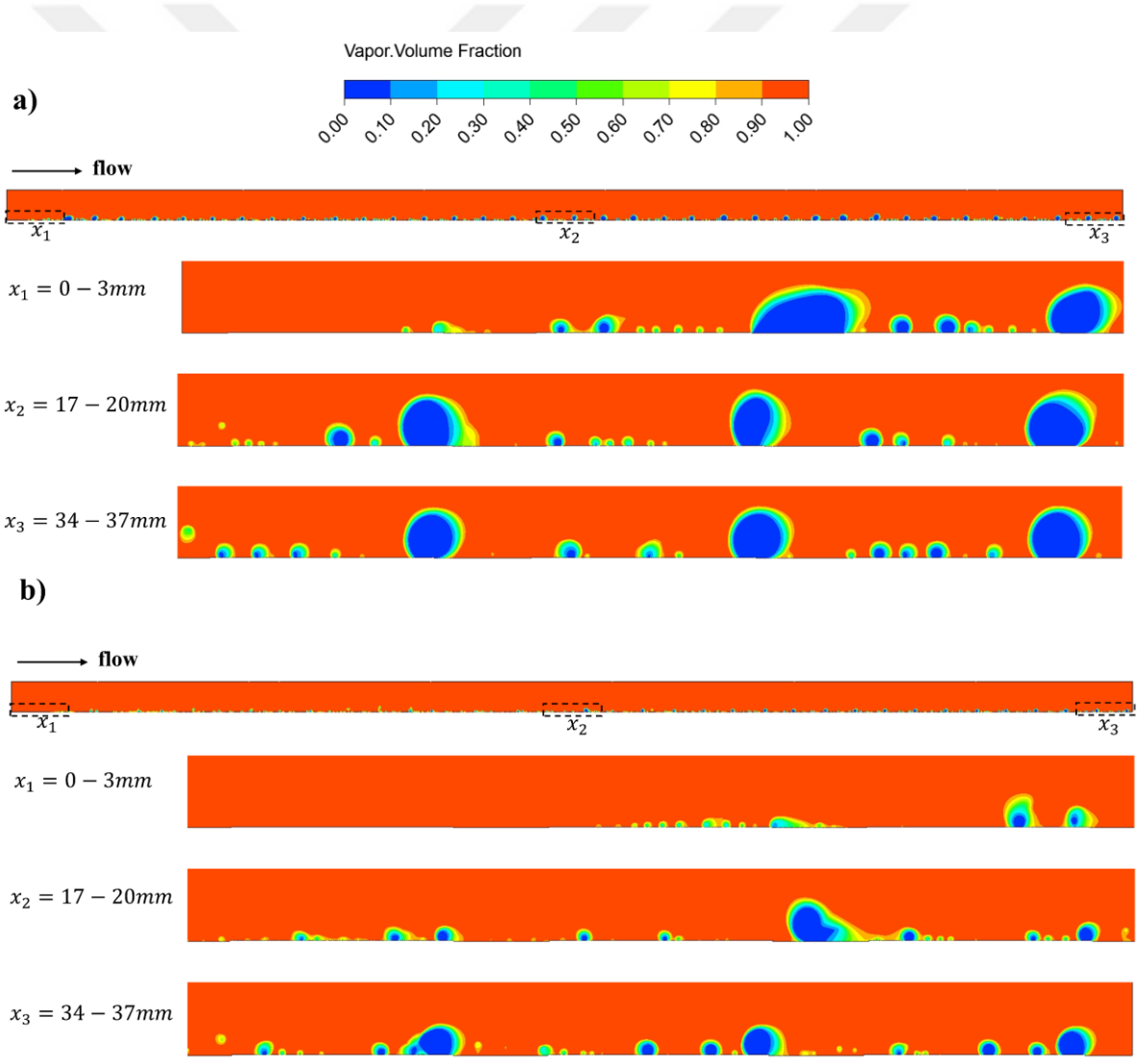

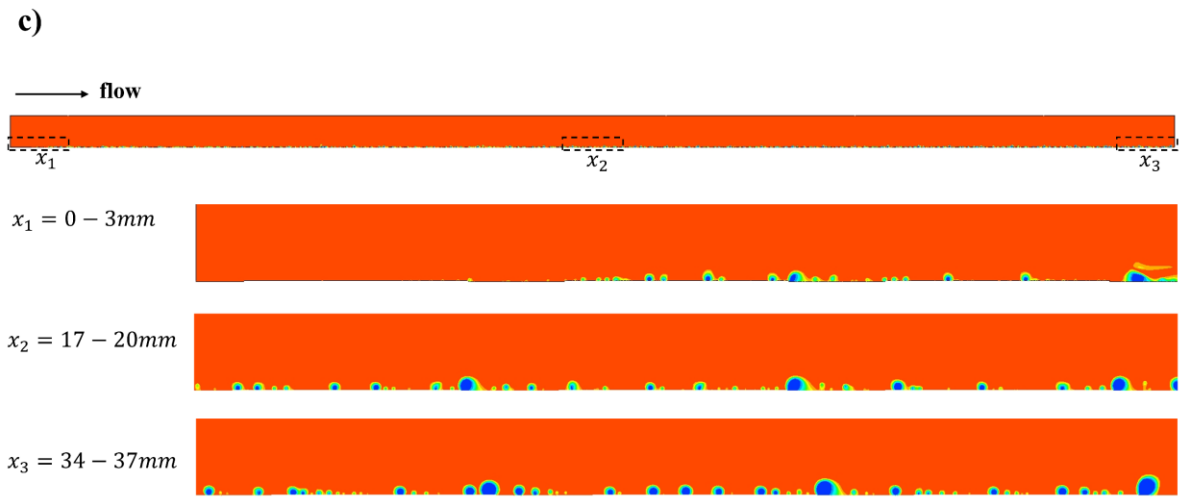

FIG 4-4 Vapor volume fraction contours of the biphilic surfaces with hydrophobic pattern of D700 at t=0.5s at different cross-sections of the computational domain for various steam mass fluxes: a) SMF 10; b) SMF 20, c) SMF 30 $kg/m^2\,s$

In FIG 4-5 , vapor volume fraction contours are presented at three distinct sections of the minichannel with the biphilic surface having $900\mu m$ patterns (D900) at three different SMF. As shown in FIG 4-5 , the droplets on D900 surface are smaller compared to D300 and D700. Unlike previous cases, droplets are also formed in the entrance section of the minichannel, due to an expanded hydrophobic region and consequently increased nucleation sites. However, shear force dominates the inertial forces with SMF resulting in less droplets in entrance section as can be seen in FIG 4-5 (c).

Owing to fewer superhydrophobic areas, less droplet-jumping is observed on top of D900 patterned surfaces. In all cases, for lower steam mass flux (SMF), it can be observed that the nearby superhydrophobic zone hinders the droplets forming in the hydrophobic patterns from rolling downhill once they reach a certain departure diameter. In other words, the droplets were pinned to the hydrophobic surfaces, and also small droplets are dragged to the patterned regions.

To sum up, the dropwise condensation results on biphilic surfaces reveal that the superhydrophobic zone is predominantly covered by relatively smaller droplets, while larger droplets are observed in the hydrophobic regions, shown in FIG 4-3 to FIG 4-5 . This trend is attributed to the higher surface energy and condensation rates on hydrophobic surfaces. Unlike the scenario of a plain hydrophobic or superhydrophobic surface, the maximum droplet size is reduced, and droplets are generated at a higher frequency rate on biphilic surfaces. Also, the droplet distribution changes with variations in the pattern. Furthermore, biphilic surfaces with high-surface-energy regions on a superhydrophobic substrate exhibit increased jumping-droplet condensation and consequently higher surface-removal rate, which leads to a larger heat-transfer coefficient in comparison to homogeneous superhydrophobic surfaces.

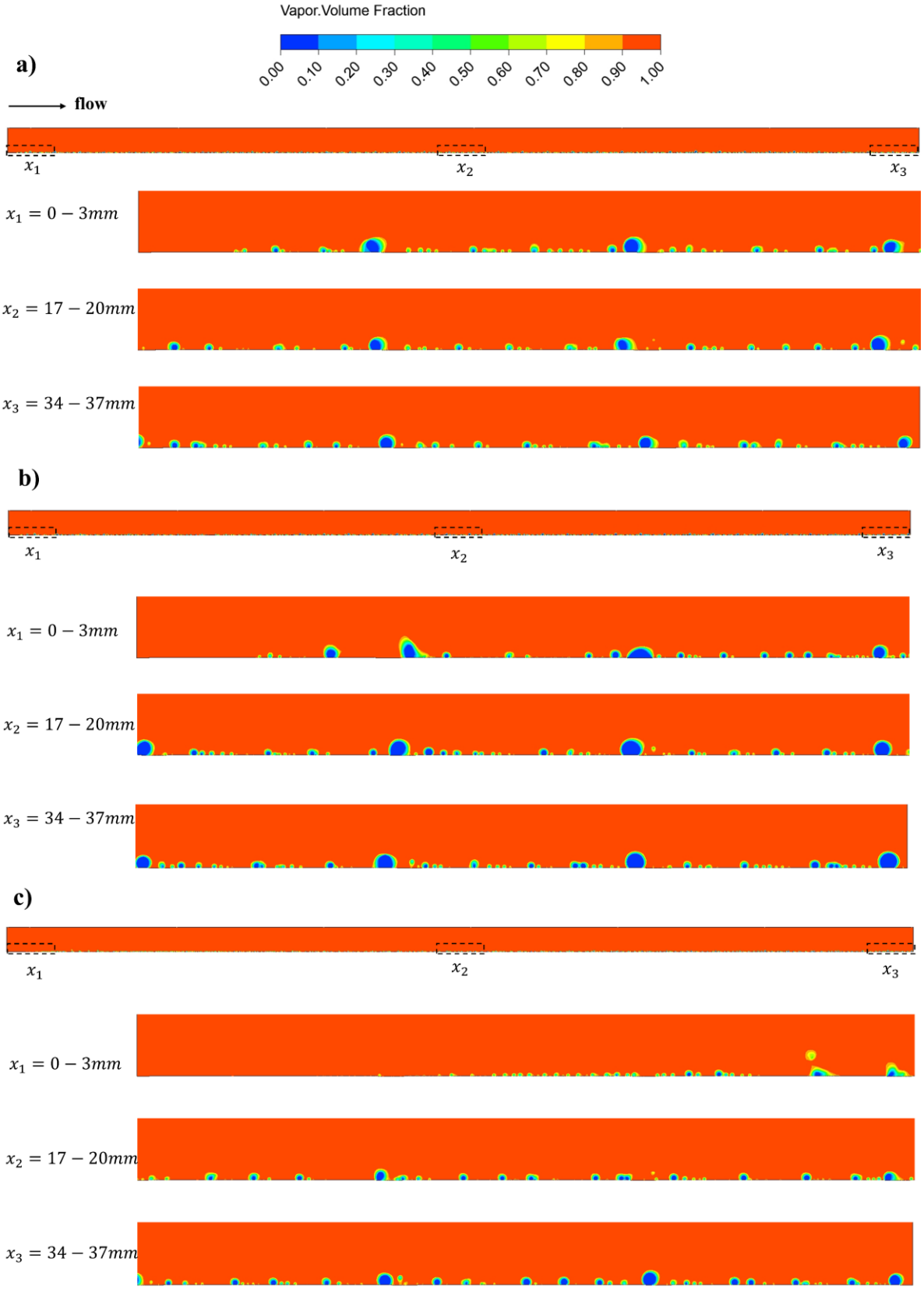

FIG 4-5 Vapor volume fraction contours for the biphilic surface with hydrophobic pattern of D900 at $t = 0.5\ s$ at different sections of the computational domain for various steam mass fluxes: a) SMF 10; b) SMF 20, c) SMF 30 $kg/m^2\ s$

4.2 Droplet Motion on biphilic surfaces with hydrophobic patterns

Using the developed model, the droplet motion along the minichannel in the direction of the flow on different biphilic surface is illustrates in FIG 4-6. Our transient simulations allow us to monitor the droplet movement during condensation proccess.

The condensation process and the droplet migration on the biphilic surface with hydrophobic pattern of D300 is depicted for SMF of $10\ kg/m^2\ s$ in FIG 4-6(a). Initially, liquid droplet nucleates on the superhydrophobic surface; then, the condensate liquid separates from its original nucleate position and moves towards the high surface energy side in the flow direction, where shear force dominates. For a brief period of time, nucleated droplets fluctuate at the left edge between hydrophobic and superhydrophobic region due to coalesencse with adjacent tiny droplets around the left edge of the spot. Later, it spontaneously moves on the mixed wettable surface, driven by unbalanced surface tension, which leads to an increase in the droplet-surface contact area. During droplet growth, droplet sticks at a specific point for a short period of time; then, the droplet keeps enlargening while traverseing the hydrophobic region by coalesencse with other small droplets. Subsequently, it moves to the right edge of the hydrophobic spot, sustaining further expansion and remaining in place.

In FIG 4-6(b), the droplet mobility on the biphilic surface with hydrophobic pattern of D700 is demonstrated for SMF of $10\ kg/m^2\ s$. First, the condensate liquid nucleates on the hydrophobic region. The nucleate droplet migrates to reach a specific point where it stops for a short period as it grows. The droplet then migrates, coalesces with nearby tiny droplets, and becomes larger; it pins at the right edge of the first spot for a short period of time. Unlike D300 biphilic surface, the droplet quickly moves to reach the right edge of the second hydrophobic spot, rather than adhering to the right edge of the first hydrophobic region within the same time frame. Finally, the droplet continues to grow next to the right edge of the second spot. As illustrated in FIG 4-6 (b), the droplet moves along during the greatest distance in the same duration on the D700 surface in comparison to the other cases.

The droplet motion on the biphilic surface with hydrophobic pattern of D900 can be seen in FIG 4-6(c). As can be seen, similar to D700 biphilic surface, nucleation starts on the hydrophobic spot on biphilic surface with hydrophobic pattern of D900. Thus, nucleation and growth process are similar to D700 biphilic surface; subsequently, the droplet continues to increase in size as it moves across the hydrophobic region, merging with smaller droplets. Afterward, it advances to the right edge of the hydrophobic spot, and undergoes additional expansion while maintaining its position. The droplet undergoes the same process for both D300 and D900 biphilic surfaces, while being pinned at the right edge of the hydrophobic spot, as illustrated in FIG 4-6 (a) and FIG 4-6 (c), respectively. However, the speed of droplet movement varies with changes in spot wettability.

Finally, to summarize, the findings indicate the significant impact of area ratio on the nucleation sites as well as the force balance that governs droplet motion determine whether the droplet remains mobile or becomes pinned. The area ratios of the hydrophobic to superhydrophobic region for biphilic surfaces with hydrophobic patterns of D300, D700, and D900 are $0.43, 2.3,$ and 9 respectively.

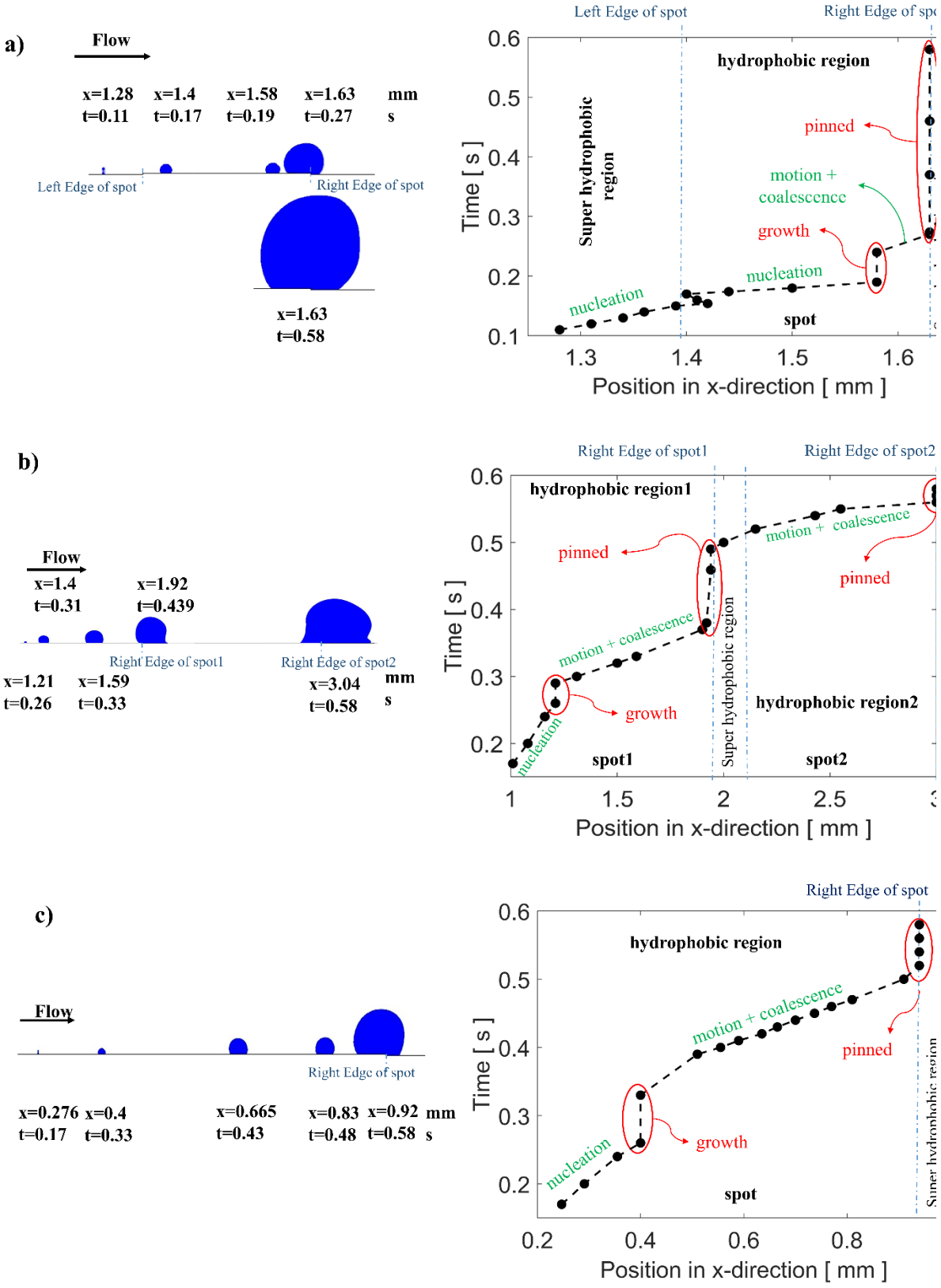

FIG 4-6 Droplet motion on various biphilic surfaces with hydrophobic patterns of a) D300, b) D700, c) D900 at SMF 10 $kg/m^2\,s$

4.3 Condensation flow pattern and droplet distribution for hydrophilic spots

The coexistence of dropwise condensation (DWC) and filmwise condensation (FWC) zones on the condensing surface provides an alternative approach to enhance surface renewal in conjunction with nucleation rate. This arrangement may involve having hydrophilic patterned zones on a superhydrophobic substrate. In the dropwise condensation (DWC) zone, surface renewal occurs via coalescence, jumping, and sweeping. This happens more often in areas with lower thermal resistance, which improves the overall heat transfer performance. Although DWC zones on superhydrophobic surfaces is known for high heat transfer coefficients, nucleation rates on hydrophilic surfaces are higher. Here, using the same pattern ratio of the previous section, we integrate dropwise and filmwise condensation models for having a hybrid system.

Three different patterned surfaces (D300, D700, and D900) were used to study dropwise condensation across the minichannel on the biphilic surface with hydrophilic spots at steam mass fluxes of $10, 20, \text{and } 30\ kg/m^2\ s$. Unlike biphilic surfaces featuring hydrophobic spots, droplets consistently nucleate at the entry section in all scenarios on biphilic surfaces with hydrophilic spots, as shown in FIG 4-7 to FIG 4-9. However, as the steam mass flux (SMF) increases, which suggests a higher velocity, the enhancing shear force significantly reduces the formation of liquid droplets at the entrance portion of the wall.

FIG 4-7 illustrates that as the steam mass flux (SMF) increases, there is a larger number of small droplets uniformly distributed across the entire wall, which is accompanied by a decrease in the number of large droplets (FIG 4-7(c)). The droplet size decreases with SMF, a phenomenon that is consistent with observations made on all the surfaces utilized in this thesis. Consequently, the largest droplet size is evident at an SMF of $10\ kg/m^2\ s$ (FIG 4-7(a),FIG 4-8(a), FIG 4-9(a)). Additionally, larger droplets consistently form on hydrophilic patterned regions in all scenarios, driven by the droplet inclination to move from lower to higher surface free energy and the higher wettability characteristic of hydrophilic surfaces. The use of hydrophilic spots ensures controlled positions for nucleation and keeping superhydrophobic surfaces free for renewal. On the other hand, biphilic surfaces with hydrophilic spots enhance liquid coverage due to their high wettability, which results in larger droplet sizes with extended contact lines and lower heat transfer coefficients (HTC) compared to biphilic surfaces with hydrophobic spots. As shown in FIG 4-7 to FIG 4-9, droplet jumping on biphilic surfaces depends on their design. The frequency of renewal through droplet jumping is notably higher on biphilic surfaces of D300 in comparison to other cases.

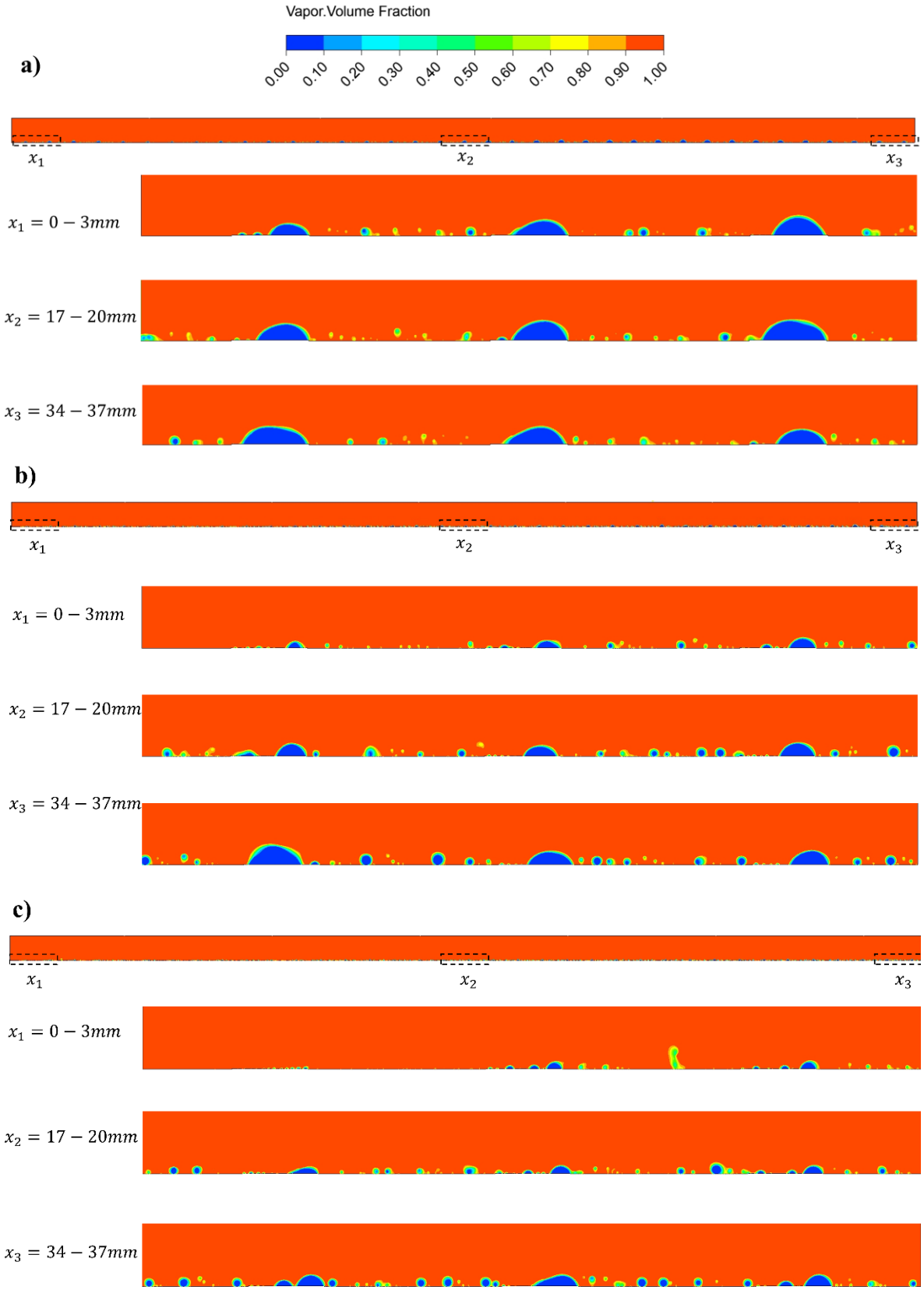

FIG 4-7 Vapor volume fraction contours for the biphilic surface with the hydrophilic pattern of D300 at $t = 0.5\ s$ at different sections of the computational domain for various steam mass fluxes: a) SMF 10; b) SMF 20, c) SMF 30 $kg/m^2\ s$

FIG 4-8 illustrates the vapor volume fraction distribution for the biphilic surface with a $700\mu m$ hydrophilic pattern size (D700) at varying steam mass fluxes (SMF). Similar to D300 biphilic surfaces, condensate droplets accumulate at the entrance section due to enhanced areas with higher surface energy.

Compared to the D300 biphilic surface, the D700 surface has a reduced frequency of droplet jumping, particularly with increasing SMF, which is attributed to the diminished superhydrophobic surface area. At higher SMF, droplets become smaller, which results in a more uniform distribution of numerous small droplets, as evident in FIG 4-8(c). Unlike D300 biphilic surfaces, larger droplets on D700 are not confined to hydrophilic zones, which depicts droplet mobility. These mobile droplets can lead to liquid bridging between patterns and migration across the channel, as can be seen in FIG 4-8 (a).

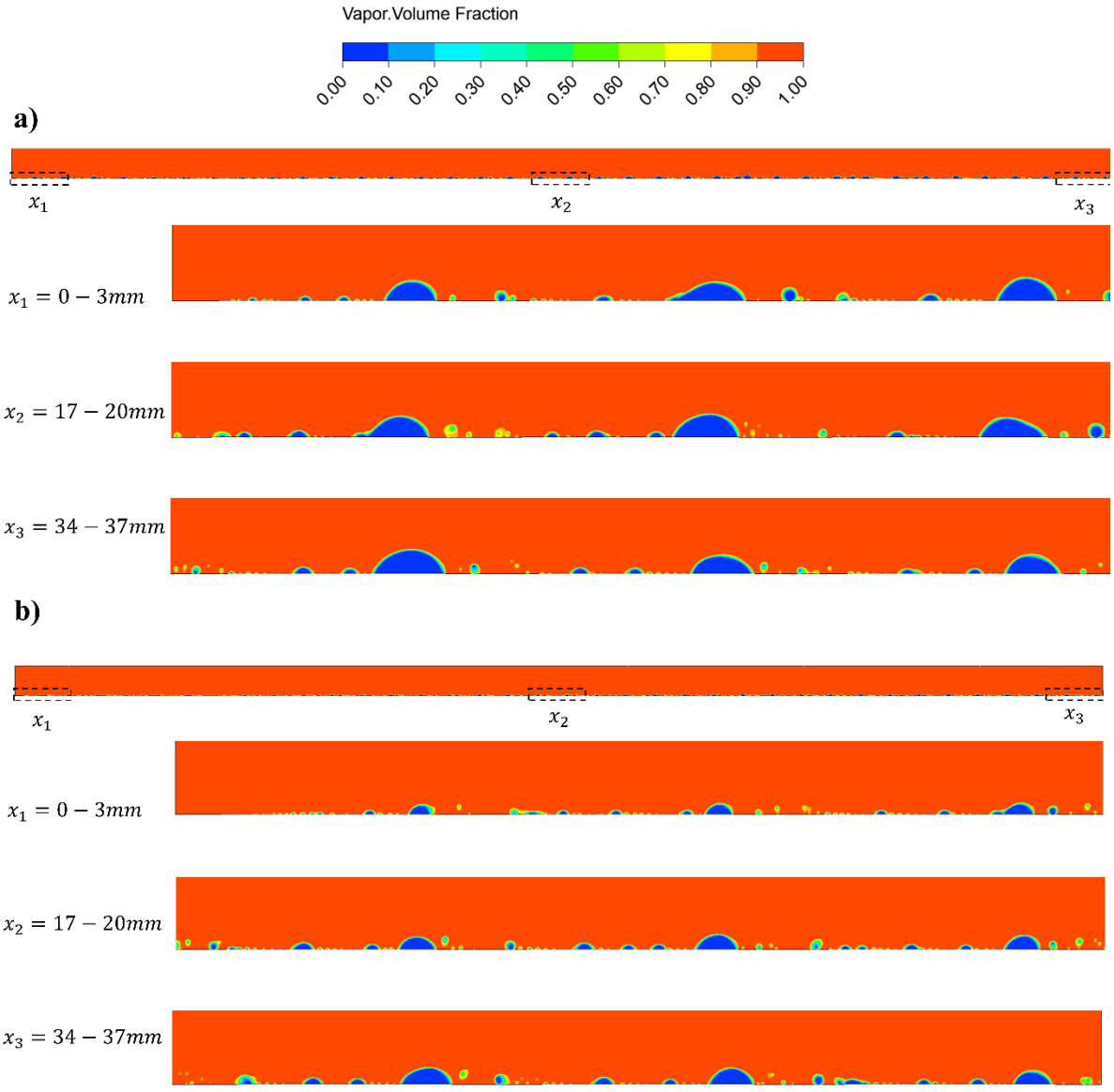

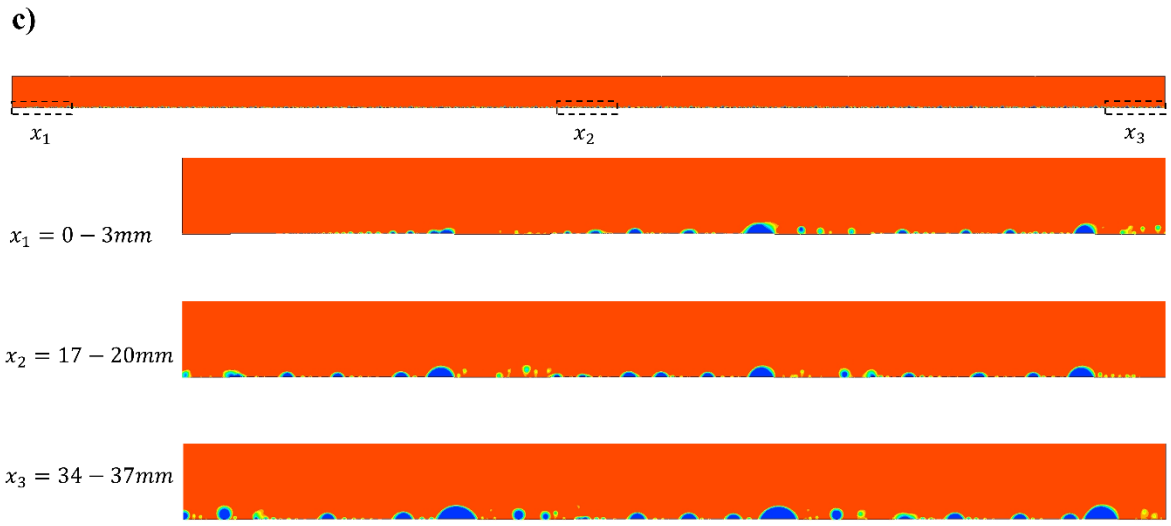

FIG 4-8 Vapor volume fraction contours for the biphilic surface with the hydrophilic pattern of D700 at $t = 0.5\ s$ at different sections of the computational domain for various steam mass fluxes: a) SMF 10; b) SMF 20, c) SMF 30 $kg/m^2\ s$

FIG 4-9 displays vapor volume fraction contours for the biphilic surface with $900\mu m$ hydrophilic patterns (D900) in three sections of the minichannel at different steam mass fluxes (SMF). The droplets on the D900 surface are smaller than those on D300 and D700 at the same SMF. Unlike previous cases, fewer droplets form in the entrance section, and with increasing SMF, shear force dominates inertial forces, which causes in fewer droplets in the entrance section, as shown in FIG 4-9(c).

Due to fewer superhydrophobic areas, droplet-jumping is less observed on D900 patterned surfaces. In all cases, at lower SMF, the nearby superhydrophobic zone impedes droplets forming in the hydrophophilic patterns from rolling downhill, pinning them to the surfaces and dragging small droplets to the patterned regions.

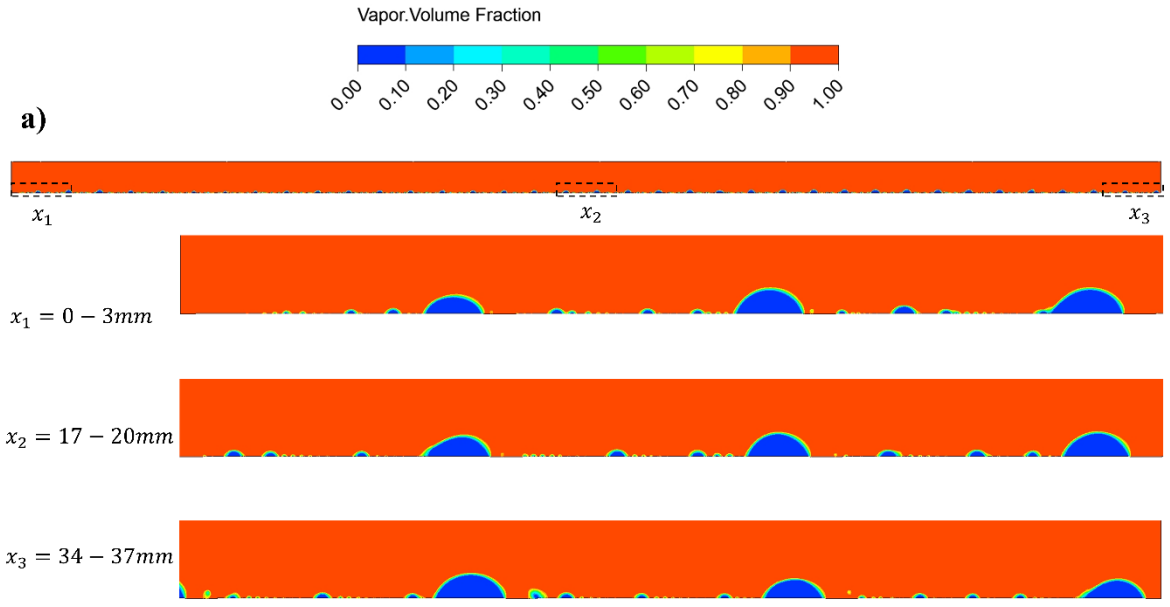

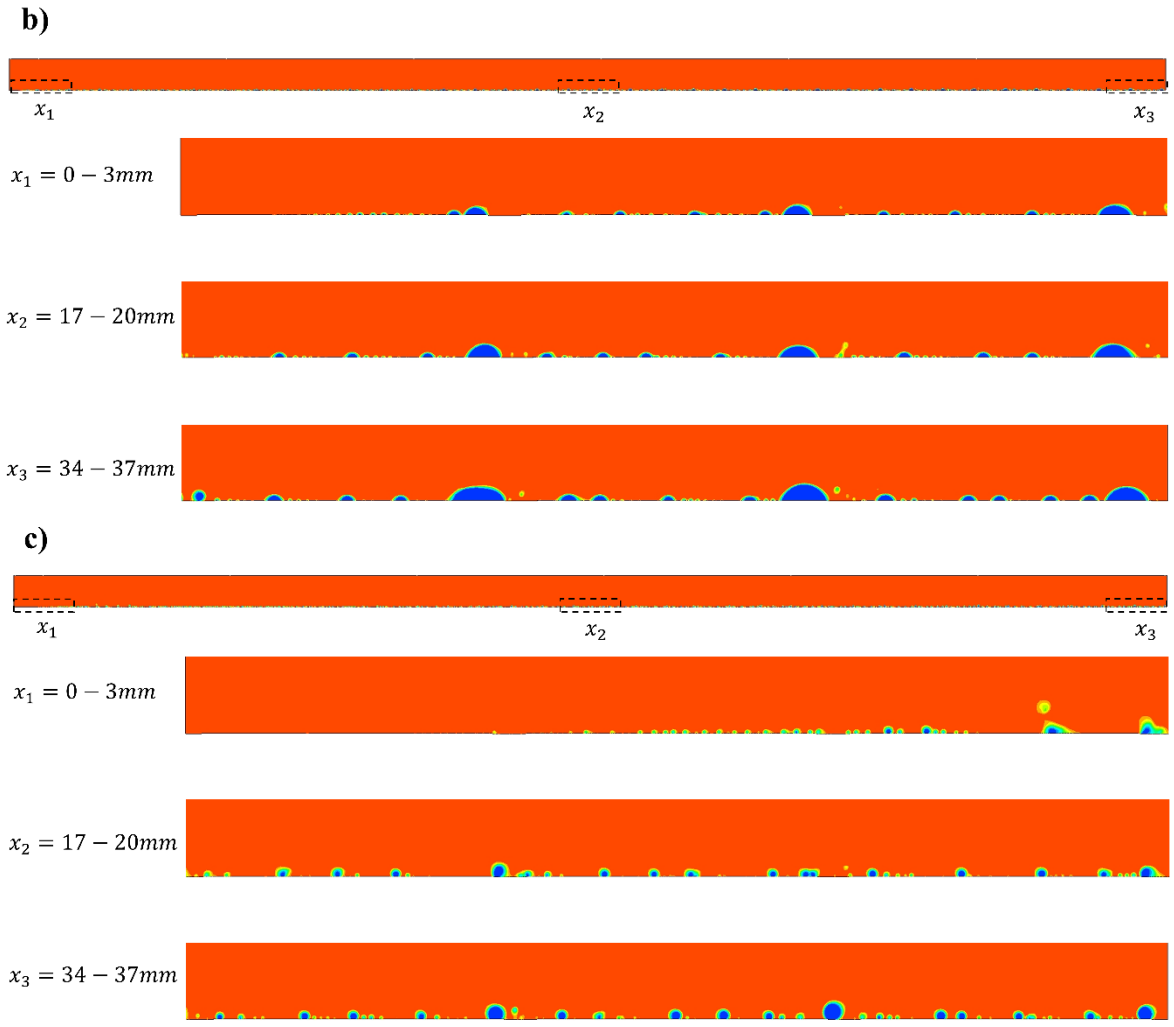

FIG 4-9 Vapor volume fraction contours for the biphilic surface with the hydrophilic pattern of D900 at $t = 0.5\ s$ at different sections of the computational domain for various steam mass fluxes: a) SMF 10; b) SMF 20, c) SMF 30 $kg/m^2\ s$

4.4 Coalescence-induced jumping

Even though the wettability of superhydrophobic and hydrophobic surfaces are the same as those from the previous chapter, the various combinations of these surfaces have a significant impact on the dynamic behavior of the condensate droplet for biphilic surfaces. FIG 4-10 shows the coalescence of the self-propelled jumping motion of condensate droplets on the superhydrophobic zone of the biphilic surface with the hydrophobic pattern of D700 at SMF $20\ kg/m^2\ s$. This motion originates from the surface energy generated during droplet coalescence.

Jumping droplets on the superhydrophobic surface and a pinned droplet on the hydrophobic spot can be seen in FIG 4-10 at t=400 ms. Then, the flying droplet moves in the flow direction and collides with the other jumping droplets; they begin merging and along a liquid bridge is extended at t=410 and 412 ms. Subsequently, a large droplet forms and the large condensate droplets falls due to gravity on the superhydrophobic region at $t = 420\ ms$. Simultaneously,

at $t = 420\,ms$, additional new nucleated liquids appear near both the droplets on the hydrophobic spot and the superhydrophobic zone. At $t = 430\,ms$, the left nucleated condensate coalesces with the other jumping droplet and rolls down on the superhydrophobic zone. At $t = 440\,ms$, the large droplet on the superhydrophobic region moves along the opposite direction of the flow, approaching to the other large droplet on the hydrophobic spot. The surface energy produced during drop coalescence appears to be the driving force behind the self-propelled motion of the drops. At $t = 450\,ms$, the droplet coalescence occurs, and a bigger droplet forms. At $t = 460\,ms$, the big droplet is dragged to the hydrophobic spot from the superhydrophobic region due to the higher surface energy of the hydrophobic spot. Surface-renewal can be seen at $t = 440\,ms$. It is evident that by jumping, the droplet is removed on its own without the assistance of outside forces, which potentially improves condensation heat transfer (self-removal). FIG 4-10 reveals that the condensates can quickly be self-removed due to the sharp tip of the patterned surface, which reduces the solid-liquid contact area and surface adhesion to condensed droplets.

These findings shed light on the spontaneous upward movement of condensates and will direct surface structure design towards a direction of the increase of the upward Laplace pressure that causes the condensate's upward migration and Wenzel to Cassie transition, as well as the ensuing self-removal. Our results demonstrate that while jumping action is observed only on the superhydrophobic surface, which plays a crucial role in reaching high heat transfer by increasing the removal rate, it is not necessarily associated with the superhydrophilicity of the surface. As can be seen the jumping action is observed on hybrid surfaces and not on the uniform superhydrophobic surface.

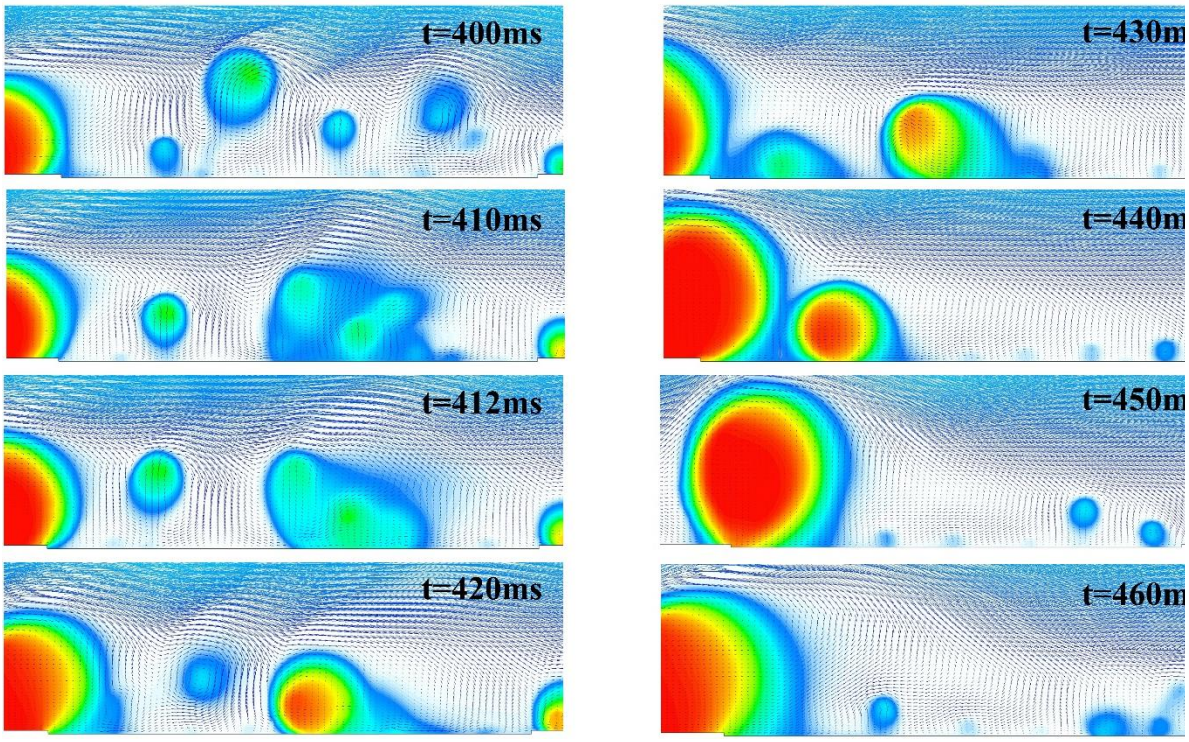

FIG 4-10 The coalesence of jumping droplet mechanism on the superhydrophobic zone of the biphilic surface with hydrophobic pattern of D700 at SMF 20 $kg/m^2\,s$.

4.5 Droplet Evolution

Velocity distribution and the mechanism of droplet growth during coalescence on the hydrophobic zone of the biphilic surface with the hydrophobic pattern of D900 are depicted at SMF 10 $kg/m^2\,s$ in detail in FIG 4-11. As shown in FIG 4-11(a), Moving droplet migrate toward stationary droplet and then the liquid bridge begin to form as they merge. Merging process occurs when the liquid bridge expanded and movement of the droplet, causing a vortex to form close to the top of the stationary droplet and an opposite velocity to arise near the liquid bridge (shown in FIG 4-11(b)). Due to its initial velocity, the left side droplet exhibits a quicker rate of deformation and an asymmetrical shape in the liquid bridge. Capillary force induces the large opposite velocity near the liquid bridge when two droplets coalesce. Then vortex arises on top of the stationary droplet with the proceeding of mergence (shown in FIG 4-11(c)). A vertical upward reaction force arises when the liquid bridge and surface come together, causing the droplet to retract in X direction while expanding in Y direction (shown in FIG 4-11(c)). Following their merging into a single droplet, the wettability gradient's directional force causes a noticeable variation in the average velocity distribution within the droplet. (shown in FIG 4-11(e)). This aligns with the droplet movement as the left droplet undergoes a slight movement towards the right direction, while the right droplet nearly maintains its original position.

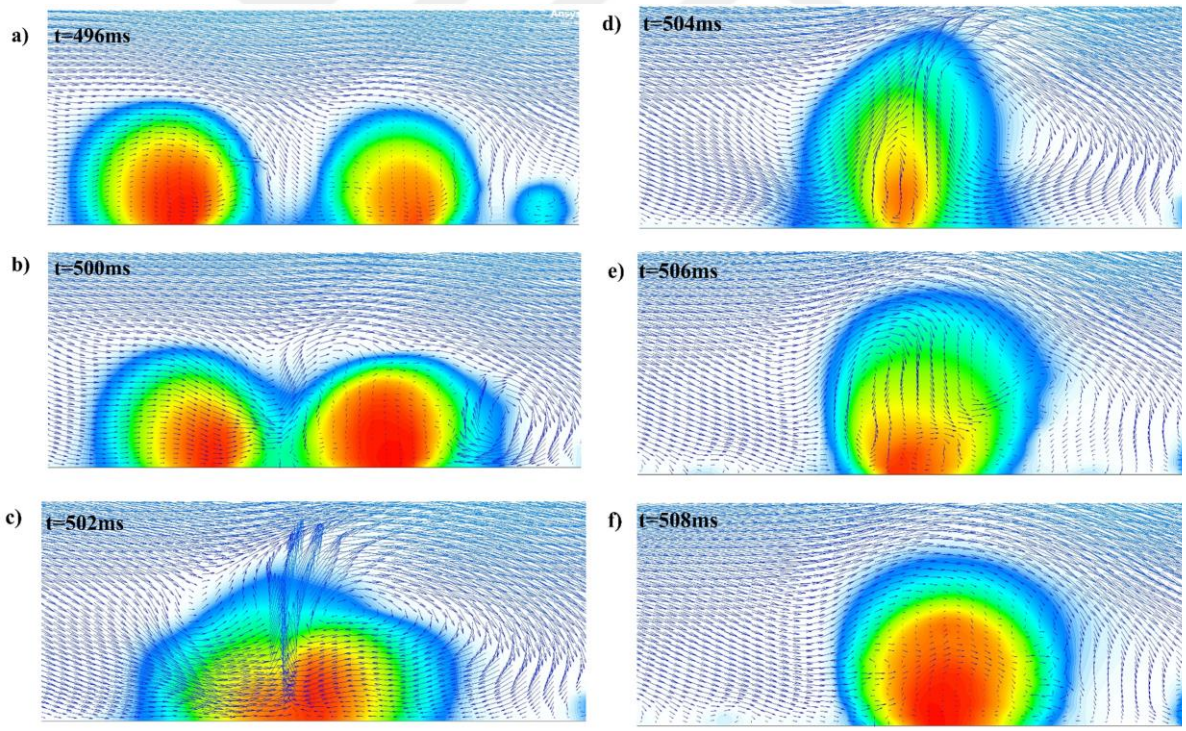

FIG 4-11 The evolution of the vapor-liquid interface and the velocity distribution during droplet coalescence in the hydrophobic region of the biphilic surface with hydrophobic patterns of D900 at SMF 10 $kg/m^2\,s$.

In this section, the velocity distribution and coalescence mechanism on the hydrophobic spot of the biphilic surface with hydrophobic patterns of D700 is illustrated at SMF 20 $kg/m^2\,s$ in FIG 4-12. FIG 4-12(a) displays the internal velocity vectors of two droplets that get closer, near the surface step between hydrophobic and superhydrophobic regions. First, in the stage I

the right side droplet migrate from low surface energy to the high surface energy, while the left side droplet that is situated on the high surface energy is stationary. As expected, the condensing droplets proceed from a lowest to a greater wettability zone, or from superhydrophobic to hydrophobic regions, as shown in FIG 4-12(a). Then, in the stage II the liquid bridge begins to expand. On the liquid bridge, a capillary force differences increases the mobility of the right droplet and inhibits the left droplet's movement on the high surface free energy pattern. As a result, significant velocity toward high surface energy pattern and opposing vortices form on top and below the liquid bridge. Finally, the resulting merged droplet is dragged to the hydrophobic pattern, as seen in FIG 4-12(a).

FIG 4-12(b) illustrates the coalescence mechanism of two droplet on the hydrophobic zone of the biphilic surface with hydrophobic patterns of D700 at SMF $20\,kg/m^2\,s$. As can be seen, the right side droplet is stationary while the left side droplet is moving droplet. First, in stage I, the moving droplet migrate towards the stationary droplet. Second, in stage II two droplets on the hydrophobic zone contact each other and begin to form a bridge similar to the mechanism as seen in FIG 4-11 and FIG 4-12(a). resulting in the large opposite velocity near the liquid bridge when two droplets coalesce induced by capillary force. Then vortex arises on top of the stationary droplet with the proceeding of mergence. Finally, the smaller droplet is drawn towards the larger one due to its velocity vectors pointing in the direction of the larger droplet as can be seen in the stage III. In both cases, the velocity vectors direct the smaller droplet towards merging with the larger one.

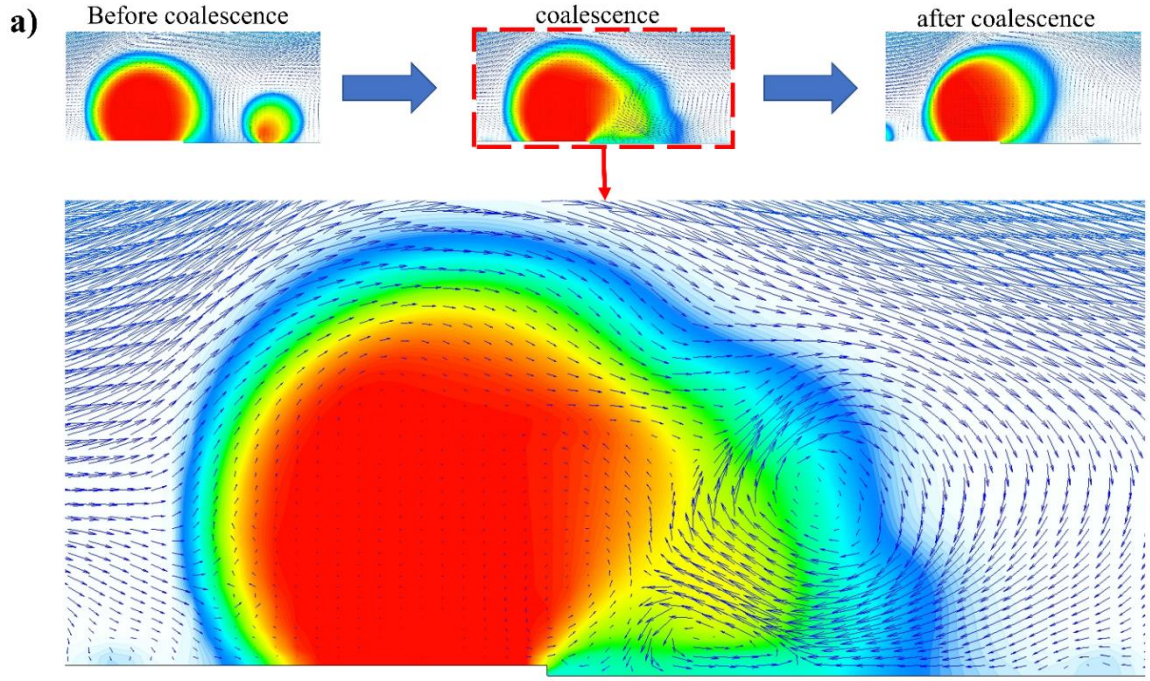

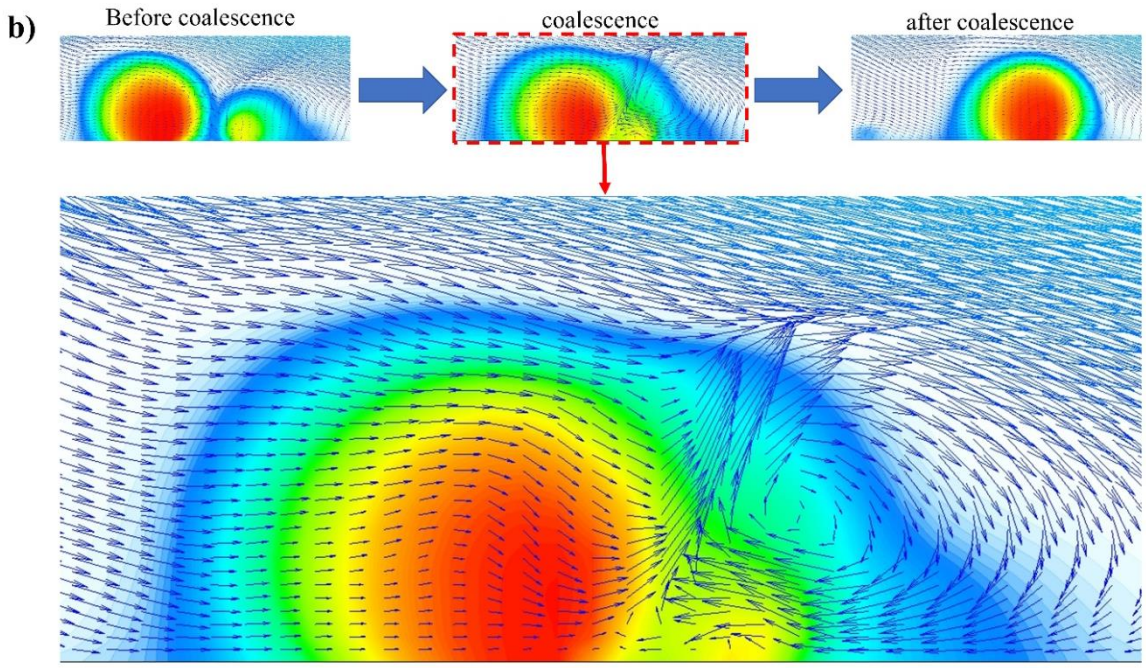

FIG 4-12 Velocity distribution and coalescence mechanism on the hydrophobic spot of the biphilic surface with hydrophobic patterns of D700 at SMF 20 $kg/m^2\ s$; a) near the surface step of the hydrophobic zone, b) on the hydrophobic zone.

4.6 Heat Transfer analysis

FIG 4-13 displays the condensation heat transfer coefficient (HTC) for nine various surfaces with varying pattern size (D) at different steam mass fluxes (SMF). The comparison consists of plain superhydrophobic (Shpho), plain hydrophobic (hpho), and plain hydrophilic (hphi) surfaces. Additionally, there are six biphilic surfaces labeled with 'D,' denotes as the pattern size in micrometers, and prefixed with hphi and hpho to indicate the pattern type as hydrophilic and hydrophobic, respectively.

As can be seen, the condensation heat transfer coefficient increases with increasing steam mass flux for all surfaces, but the enhancement rate varies based on surface properties. Vapor shear force, which drives droplet removal in dropwise flow condensation, increases with steam mass flux. As a result, the departure radius of droplets decreases as they are removed from the surface in smaller sizes, due to the intensified vapor shear force at the condensed droplet interface. This removal process facilitates the nucleation of new droplets, thereby enhancing the condensation heat transfer performance.

At all steam mass fluxes, there is a consistent decrease in the heat transfer coefficient with an increase in the size of the hydrophobic pattern across both biphilic surface design. As a result, the minimum heat transfer coefficient is associated with the D900 biphilic surface at an SMF of 10 $kg/m^2\ s$, while the maximum is observed for the D300 surface at an SMF of 30 $kg/m^2\ s$. The observed trend can be attributed to two reasons; first, the effect of surface renewal on the heat transfer coefficient. Biphilic surfaces with smaller pattern sizes contain a higher proportion of superhydrophobic surfaces, which facilitates effective droplet removal and consequently leads to an enhanced heat transfer coefficient. Furthermore, hydrophobic

patterns increase the number of nucleation sites, where further contributes to the improvement of heat transfer. Second, the impact of pinned droplets formation plays a major role. As the size of pattern increases, formation of larger pinned droplets reduces the surface removal time. As a result, the heat transfer coefficient decreases.

Biphilic surfaces with hydrophilic patterns exhibit a similar trend. Nevertheless, these surfaces demonstrate superior heat transfer performance when compared to biphilic surfaces with hydrophobic patterns, due to their higher droplet nucleation rate. It suggests that it is preferable to optimize spot wettability to maximize individual droplet growth rates while ensuring efficient droplet removal.

The model results indicate that biphilic surfaces with mixed wettability perform significantly better in condensation heat transfer in comparison to surfaces with uniform wettability including hydrophobic and hydrophilic surfaces, and hydrophilic surfaces exhibit a poor heat transfer performance in comparison to all scenarios. This improvement is attributed to the combined effects of surface structure and mixed wettability, which rises droplet departure frequency, condensation cycle period, and prevent flooding. There is an optimal pattern size for each steam mass flux (shown with green circle), where heat transfer performance is at its peak. For steam mass fluxes of $10, 20,$ and $30\ kg/m^2s$, the optimum pattern size is found to be $300\ \mu m$ with a hydrophilic pattern, $300\ \mu m$ with hydrophobic pattern, and $300\ \mu m$ with hydrophobic pattern, respectively, with the ratio of pattern to superhydrophobic surface area 7.6 . The highest observed heat transfer coefficient in this experiment is $83\ kW/m^2K$, achieved at a mass flux of $30\ kg/m^2s$ on the biphilic surface with a hydrophobic pattern size of $300\ \mu m$. The findings align with prior experimental research [117] for steam mass flux (SMF) values of 20 and $30\ kg/m^2s$. However, for SMF 10 kg/m^2s, the optimal heat transfer is enhanced via additional study of the hydrophilic pattern.

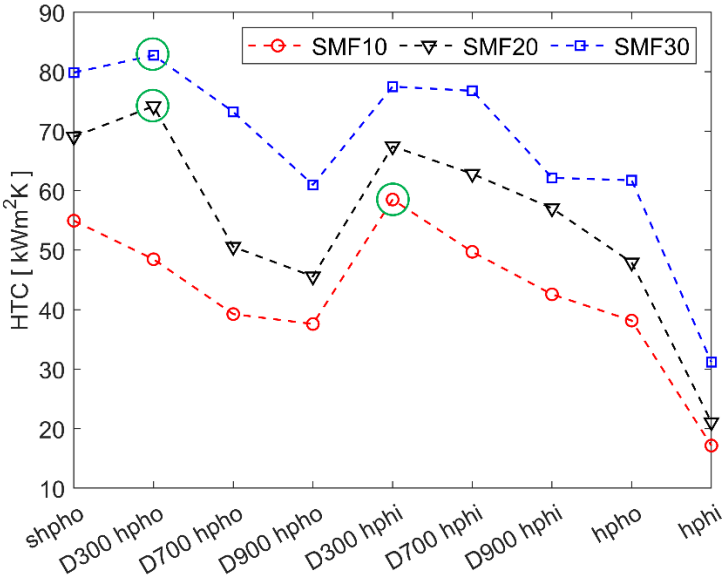

FIG 4-13 Time-averaged heat transfer coefficients at different SMFs on various surfaces : plain superhydrophobic (Shpho), plain hydrophobic (hpho), and plain hydrophilic (hphi) surfaces, biphilic surfaces labeled with 'D,' denoting the pattern size in micrometers, and prefixed with hphi and hpho to indicate the pattern type as hydrophilic and hydrophobic, respectively.

5 CONCLUSIONS

This dissertation presents an extensive modeling investigation on dropwise condensation on diverse surfaces with varying contact angles, materials, and designs. The primary goal was to analyze the effect of steam mass flux and different wettability combinations on heat transfer, which aims to identify the optimal surface characteristics and steam mass flux for achieving maximum heat transfer. Functional surfaces included hydrophilic, hydrophobic, superhydrophobic, and innovative biphilic surfaces.

Based on the findings presented in this thesis, the following conclusions can be drawn:

- The findings consistently showed a positive correlation among higher contact angles, lower wettability, and superior heat transfer performance on surfaces with uniform wettability. Irrespective of the surface material, superhydrophobic surfaces consistently demonstrated a higher heat transfer performance.
- The strong alignment between numerical simulations and experimental data highlights the reliability of the model in accurately representing real-world condensation processes. This validation not only strengthens the credibility of the model but also confirms the practical functionality of the model for predicting and optimizing dropwise condensation behavior.
- The three-dimensional model can capture each stage of the condensation process. It provides detailed information about multiple successive coalescences, coalescence occurring in various directions, droplet jumping, simultaneous presence of droplets of different sizes during condensation, pinned droplets, and vortices around the droplet during coalescence.
- At a given steam mass flux, the heat transfer coefficient consistently decreases as the hydrophobic pattern size increases. Biphilic surfaces with hydrophilic patterns display a comparable trend but outperform surfaces with hydrophobic patterns and uniform wettability due to their higher droplet nucleation rate. This indicates that optimizing spot wettability is preferable for maximizing individual droplet growth rates while minimizing droplet adhesion. The thesis visually illustrated enhanced droplet nucleation and rapid sweeping, which resulted from both extended sweeping time and spatial control of droplet nucleation.
- The strategies proposed in this thesis, such as employing specific mixed wettability surface configurations, increasing steam mass flux, and reducing wettability, contribute to a reduction in the average droplet size. This reduction, in turn, enhances the efficiency of condensation heat transfer.
- Another approach employed in this thesis is boosting the heat transfer coefficient involving increasing nucleation sites and reducing condensation cycle time through the unique design of biphilic surfaces. Consequently, the integration of biphilic surfaces at higher steam mass flux contributes to a further increase in the heat transfer coefficient.

6 Future Work

This dissertation has contributed significantly to the understanding of dropwise condensation by conducting an extensive numerical investigation on diverse surfaces. The comprehensive exploration of contact angles, materials, and designs aimed to identify optimal surface characteristics and steam mass flux for maximizing heat transfer efficiency. The following future work suggestions emerge from the conclusions drawn in this thesis:

Further optimization studies could explore a broader range of parameters, such as steam pressure, steam quality, and surface roughness, to identify comprehensive sets of conditions for maximizing heat transfer efficiency. This could provide more versatile guidelines for adapting the technology to diverse operating environments.

Expanding the model to address minichannels with various cross-sectional areas could offer insights into the specific dynamics of condensation in such configurations, contributing to a thorough understanding of condensation heat transfer phenomena.

Extending the numerical model to investigate the effects of integrating gravity and shear force, especially in conjunction with tilting the surface, is recommended. This extension would deepen the understanding of the removal phenomenon, considering scenarios where both forces contribute to cleaning the surface—going beyond the limitations of our current model, which only considered horizontal surfaces with negligible gravity effects.

Future research could delve into multi-scale analyses to explore the interplay between micro and macroscopic factors influencing dropwise condensation. Investigating how nanoscale surface features contribute to overall heat transfer efficiency could provide a thorough understanding and guide the design of tailored surfaces.

Exploring future biphilic surface designs that incorporate a combination of hydrophilic and hydrophobic patterns with varying ratios on a superhydrophobic background is recommended. This approach aims to leverage the advantages of both surface types, potentially leading to the creation of more efficient surfaces tailored to specific application requirements.

Further exploration could involve varying the ratio of pattern to substrate across a wide range of sizes, as well as adjusting pattern heights. Understanding the flow patterns with variations in pattern heights and the impact of drag coefficients and acting forces may contribute valuable insights for application-oriented surface designs.

BIBLIOGRAPHY

1. Beér, J.M., *High efficiency electric power generation: The environmental role.* Progress in Energy and Combustion Science, 2007. **33**(2): p. 107-134.
2. Bao, J., et al., *Strengthening power generation efficiency utilizing liquefied natural gas cold energy by a novel two-stage condensation Rankine cycle (TCRC) system.* Energy Conversion and Management, 2017. **143**: p. 312-325.
3. Benim, A.C., et al. *Modelling the flow in the exhaust hood of steam turbines under consideration of turbine-exhaust hood interaction*. 1995. Germany: VDI-Verl, Duesseldorf (Germany).
4. Arunkumar, T., et al., *A review of efficient high productivity solar stills.* Renewable and Sustainable Energy Reviews, 2019. **101**: p. 197-220.
5. Dounis, A.I. and C. Caraiscos, *Advanced control systems engineering for energy and comfort management in a building environment—A review.* Renewable and Sustainable Energy Reviews, 2009. **13**(6): p. 1246-1261.
6. Mousa, H., et al., *Experimental study and analysis of solar still desalination using phase change materials.* Journal of Energy Storage, 2019. **26**: p. 100959.
7. Zhao, B., L.-Y. Wang, and T.-S. Chung, *Enhanced membrane systems to harvest water and provide comfortable air via dehumidification & moisture condensation.* Separation and Purification Technology, 2019. **220**: p. 136-144.
8. Lukic, N., et al., *Economical aspects of the improvement of a mechanical vapour compression desalination plant by dropwise condensation.* Desalination, 2010. **264**(1): p. 173-178.
9. Wang, S., et al., *Enhanced condensation heat transfer in air-conditioner heat exchanger using superhydrophobic foils.* Applied Thermal Engineering, 2018. **137**: p. 758-766.
10. Patil, M.S., J.-H. Seo, and M.-Y. Lee, *Heat transfer characteristics of the heat exchangers for refrigeration, air conditioning and heat pump systems under frosting, defrosting and dry/wet conditions—A review.* Applied Thermal Engineering, 2017. **113**: p. 1071-1087.
11. Mudawar, I., *Assessment of high-heat-flux thermal management schemes.* IEEE Transactions on Components and Packaging Technologies, 2001. **24**(2): p. 122-141.
12. Peters, T.B., et al., *Design of an Integrated Loop Heat Pipe Air-Cooled Heat Exchanger for High Performance Electronics.* IEEE Transactions on Components, Packaging and Manufacturing Technology, 2012. **2**(10): p. 1637-1648.
13. Rose, J.W., *Condensation Heat Transfer Fundamentals.* Chemical Engineering Research and Design, 1998. **76**(2): p. 143-152.
14. Rose, J.W., *Dropwise condensation theory and experiment: A review.* Proceedings of the Institution of Mechanical Engineers, Part A: Journal of Power and Energy, 2002. **216**(2): p. 115-128.
15. Selvakumar, R.D., et al., *Numerical modeling of solid-liquid phase change under the influence an external electric field.* International Journal of Multiphase Flow, 2021. **136**: p. 103550.
16. Choi, D.H., et al., *Thermal conductivity and heat transfer performance enhancement of phase change materials (PCM) containing carbon additives for heat storage application.* International journal of refrigeration, 2014. **42**: p. 112-120.
17. Schmidt, E., W. Schurig, and W. Sellschopp, *Versuche über die Kondensation von Wasserdampf in Film- und Tropfenform.* Technische Mechanik und Thermodynamik,

1930. **1**(2): p. 53-63.
18. Le Fevre, E.J. and J.W. Rose, *An experimental study of heat transfer by dropwise condensation.* International Journal of Heat and Mass Transfer, 1965. **8**(8): p. 1117-1133.
19. Graham, C. and P. Griffith, *Drop size distributions and heat transfer in dropwise condensation.* International Journal of Heat and Mass Transfer, 1973. **16**(2): p. 337-346.
20. Liu, L., et al., *Dropwise Condensation by Nanoengineered Surfaces: Design, Mechanism, and Enhancing Strategies.* Advanced Materials Interfaces, 2021. **8**(24): p. 2101603.
21. Murase, T., et al., *Condensation on a Horizontal Wire-Wrapped Tube.* Journal of Heat Transfer, 2005. **127**(11): p. 1207-1213.
22. Ali, H.M. and M.Z. Qasim, *Free convection condensation of steam on horizontal wire wrapped tubes: Effect of wire thermal conductivity, pitch and diameter.* Applied Thermal Engineering, 2015. **90**: p. 207-214.
23. Andrews, H.G., et al., *Three-Dimensional Hierarchical Structures for Fog Harvesting.* Langmuir, 2011. **27**(7): p. 3798-3802.
24. Milani, D., et al., *Evaluation of using thermoelectric coolers in a dehumidification system to generate freshwater from ambient air.* Chemical Engineering Science, 2011. **66**(12): p. 2491-2501.
25. Pérez-Lombard, L., J. Ortiz, and C. Pout, *A review on buildings energy consumption information.* Energy and Buildings, 2008. **40**: p. 394-398.
26. Oh, I., et al., *Enhanced Condensation on Liquid-Infused Nanoporous Surfaces by Vibration-Assisted Droplet Sweeping.* ACS Nano, 2020. **14**(10): p. 13367-13379.
27. Ng, B.T., Y.M. Hung, and M.K. Tan, *Acoustically-controlled Leidenfrost droplets.* Journal of Colloid and Interface Science, 2016. **465**: p. 26-32.
28. Lee, C. and C.-J. Kim, *Underwater Restoration and Retention of Gases on Superhydrophobic Surfaces for Drag Reduction.* Physical Review Letters, 2011. **106**(1): p. 014502.
29. Traipattanakul, B., C.Y. Tso, and C.Y.H. Chao, *Study of jumping water droplets on superhydrophobic surfaces with electric fields.* International Journal of Heat and Mass Transfer, 2017. **115**: p. 672-681.
30. O'Callaghan, P.W., PhD, and R.F. Babus'Haq, *Cooling Problems Facing the Electronics and Aerospace Industries.* Aircraft Engineering and Aerospace Technology, 1990. **62**(7): p. 17-19.
31. Leipertz, A. and A. Fröba, *Improvement of Condensation Heat Transfer by Surface Modifications.* Heat Transfer Engineering, 2008. **29**: p. 343-356.
32. Young, T. *An essay on the cohesion of fluids*. in *Abstracts of the Papers Printed in the Philosophical Transactions of the Royal Society of London*. 1832. The Royal Society London.
33. Cassie, A. and S. Baxter, *Wettability of porous surfaces.* Transactions of the Faraday society, 1944. **40**: p. 546-551.
34. Wenzel, R.N., *Resistance of solid surfaces to wetting by water.* Industrial & engineering chemistry, 1936. **28**(8): p. 988-994.
35. Johnson Jr, R.E. and R.H. Dettre, *Contact angle hysteresis. III. Study of an idealized heterogeneous surface.* The journal of physical chemistry, 1964. **68**(7): p. 1744-1750.
36. Dettre, R.H. and R.E. Johnson Jr, *Contact angle hysteresis. IV. Contact angle measurements on heterogeneous surfaces1.* The journal of physical chemistry, 1965. **69**(5): p. 1507-1515.
37. Yaminsky, V., *Molecular mechanisms of hydrophobic transitions.* Journal of adhesion

science and technology, 2000. **14**(2): p. 187-233.
38. Goswami, A., S.C. Pillai, and G. McGranaghan, *Surface modifications to enhance dropwise condensation.* Surfaces and Interfaces, 2021. **25**: p. 101143.
39. Putra, N., Yanuar, and F.N. Iskandar, *Application of nanofluids to a heat pipe liquid-block and the thermoelectric cooling of electronic equipment.* Experimental Thermal and Fluid Science, 2011. **35**(7): p. 1274-1281.
40. Ma, M. and R. Hill, *Superhydrophobic Surfaces.* Current Opinion in Colloid & Interface Science, 2006. **11**: p. 193-202.
41. Roach, P., N.J. Shirtcliffe, and M.I. Newton, *Progess in superhydrophobic surface development.* Soft Matter, 2008. **4**(2): p. 224-240.
42. Abdulhussein, A.T., et al., *Current trend in fabrication of complex morphologically tunable superhydrophobic nano scale surfaces.* Applied Surface Science, 2016. **384**: p. 311-332.
43. Sanjay, S.L., et al., *Recent progress in preparation of superhydrophobic surfaces: a review.* Journal of Surface Engineered Materials and Advanced Technology, 2012. **2012**.
44. Yan, Y.Y., N. Gao, and W. Barthlott, *Mimicking natural superhydrophobic surfaces and grasping the wetting process: a review on recent progress in preparing superhydrophobic surfaces.* Adv Colloid Interface Sci, 2011. **169**(2): p. 80-105.
45. Nakajima, A., *Design of hydrophobic surfaces for liquid droplet control.* NPG Asia Materials, 2011. **3**(5): p. 49-56.
46. Chen, C.-H., et al., *Dropwise condensation on superhydrophobic surfaces with two-tier roughness.* Applied physics letters, 2007. **90**(17).
47. Dietz, C., et al., *Visualization of droplet departure on a superhydrophobic surface and implications to heat transfer enhancement during dropwise condensation.* Applied Physics Letters, 2010. **97**(3).
48. Das, A.K., et al., *The Use of an Organic Self-Assembled Monolayer Coating to Promote Dropwise Condensation of Steam on Horizontal Tubes.* Journal of Heat Transfer, 1999. **122**(2): p. 278-286.
49. Blackman, L. and M. Dewar, *30. Promoters for the dropwise condensation of steam. Part IV. Discussion of dropwise condensation and testing of compounds.* Journal of the Chemical Society (Resumed), 1957: p. 171-176.
50. Wilmshurst, R. and J.W. Rose. *Dropwise and filmwise condensation of aniline, ethanediol and nitrobenzene*. in *International Heat Transfer Conference Digital Library*. 1974. Begel House Inc.
51. Fang, C., et al., *Impact of wall hydrophobicity on condensation flow and heat transfer in silicon microchannels.* Journal of Micromechanics and Microengineering, 2010. **20**(4): p. 045018.
52. Lee, S., et al., *Heat transfer measurement during dropwise condensation using micro/nano-scale porous surface.* International Journal of Heat and Mass Transfer, 2013. **65**: p. 619-626.
53. Enright, R., et al., *Dropwise condensation on micro-and nanostructured surfaces.* Nanoscale and Microscale Thermophysical Engineering, 2014. **18**(3): p. 223-250.
54. Miljkovic, N., R. Enright, and E.N. Wang, *Effect of droplet morphology on growth dynamics and heat transfer during condensation on superhydrophobic nanostructured surfaces.* ACS nano, 2012. **6**(2): p. 1776-1785.
55. Khandekar, S. and K. Muralidhar, *Dropwise condensation on inclined textured surfaces*. 2014: Springer.
56. Sikarwar, B.S., et al., *Dropwise condensation underneath chemically textured surfaces: simulation and experiments.* 2011.

57. Tanaka, H., *Measurements of drop-size distributions during transient dropwise condensation.* 1975.
58. Zhao, H. and D. Beysens, *From droplet growth to film growth on a heterogeneous surface: condensation associated with a wettability gradient.* Langmuir, 1995. **11**(2): p. 627-634.
59. Daniel, S., M.K. Chaudhury, and J.C. Chen, *Fast drop movements resulting from the phase change on a gradient surface.* Science, 2001. **291**(5504): p. 633-636.
60. Macner, A.M., S. Daniel, and P.H. Steen, *Condensation on surface energy gradient shifts drop size distribution toward small drops.* Langmuir, 2014. **30**(7): p. 1788-1798.
61. Dietz, C., et al., *Visualization of droplet departure on a superhydrophobic surface and implications to heat transfer enhancement during dropwise condensation.* Applied physics letters, 2010. **97**(3).
62. Feng, J., et al., *Why condensate drops can spontaneously move away on some superhydrophobic surfaces but not on others.* ACS applied materials & interfaces, 2012. **4**(12): p. 6618-6625.
63. Miljkovic, N., et al., *Jumping-droplet-enhanced condensation on scalable superhydrophobic nanostructured surfaces.* Nano letters, 2013. **13**(1): p. 179-187.
64. Wen, R., et al., *Three-dimensional superhydrophobic nanowire networks for enhancing condensation heat transfer.* Joule, 2018. **2**(2): p. 269-279.
65. Enright, R., et al., *How coalescing droplets jump.* ACS nano, 2014. **8**(10): p. 10352-10362.
66. Miljkovic, N., R. Enright, and E.N. Wang, *Modeling and optimization of superhydrophobic condensation.* Journal of Heat Transfer, 2013. **135**(11): p. 111004.
67. Miljkovic, N. and E.N. Wang, *Condensation heat transfer on superhydrophobic surfaces.* MRS bulletin, 2013. **38**(5): p. 397-406.
68. Cho, H.J., et al., *Nanoengineered materials for liquid–vapour phase-change heat transfer.* Nature Reviews Materials, 2016. **2**(2): p. 1-17.
69. Wen, R., et al., *Hierarchical Superhydrophobic Surfaces with Micropatterned Nanowire Arrays for High-Efficiency Jumping Droplet Condensation.* ACS Applied Materials & Interfaces, 2017. **9**(51): p. 44911-44921.
70. Dorrer, C. and J. Rühe, *Condensation and wetting transitions on microstructured ultrahydrophobic surfaces.* Langmuir, 2007. **23**(7): p. 3820-3824.
71. Thickett, S.C., C. Neto, and A.T. Harris, *Biomimetic surface coatings for atmospheric water capture prepared by dewetting of polymer films.* Advanced Materials, 2011. **23**(32): p. 3718-3722.
72. Zhang, W., et al., *Water-repellent surfaces consisting of nanowires on micropyramidal structures.* ACS Applied Nano Materials, 2019. **2**(12): p. 7696-7704.
73. Boreyko, J.B. and C.-H. Chen, *Self-propelled dropwise condensate on superhydrophobic surfaces.* Physical review letters, 2009. **103**(18): p. 184501.
74. Jung, Y. and B. BHUSHAN, *Wetting behaviour during evaporation and condensation of water microdroplets on superhydrophobic patterned surfaces.* Journal of microscopy, 2008. **229**(1): p. 127-140.
75. He, M., et al., *Hierarchical porous surface for efficiently controlling microdroplets' self-removal.* Advanced Materials, 2013. **25**(16): p. 2291-2295.
76. Quéré, D., *Non-sticking drops.* Reports on Progress in Physics, 2005. **68**(11): p. 2495.
77. Anand, S., et al., *Enhanced condensation on lubricant-impregnated nanotextured surfaces.* ACS nano, 2012. **6**(11): p. 10122-10129.
78. Derby, M.M., et al., *Flow condensation heat transfer enhancement in a mini-channel with hydrophobic and hydrophilic patterns.* International Journal of Heat and Mass Transfer, 2014. **68**: p. 151-160.

79. Shi, J., et al., *Experimental study of flow condensation heat transfer in tubes partially filled with hydrophobic annular metal foam.* International Journal of Heat and Mass Transfer, 2019. **136**: p. 1265-1272.
80. Chen, X. and M.M. Derby, *Combined Visualization and Heat Transfer Measurements for Steam Flow Condensation in Hydrophilic and Hydrophobic Mini-Gaps.* Journal of Heat Transfer, 2016. **138**(9).
81. Chen, X., J.A. Morrow, and M.M. Derby, *Mini-channel flow condensation enhancement through hydrophobicity in the presence of noncondensable gas.* International Journal of Heat and Mass Transfer, 2017. **115**: p. 11-18.
82. Yuan, J., et al., *Convective dropwise condensation heat transfer in mini-channels with biphilic surface.* International Journal of Heat and Mass Transfer, 2019. **134**: p. 69-84.
83. Chehrghani, M.M., et al., *Copper-Based Superhydrophobic Nanostructures for Heat Transfer in Flow Condensation.* ACS Applied Nano Materials, 2021. **4**(2): p. 1719-1732.
84. Kim, S. and K.J. Kim, *Dropwise Condensation Modeling Suitable for Superhydrophobic Surfaces.* Journal of Heat Transfer, 2011. **133**(8).
85. Mikic, B.B., *On mechanism of dropwise condensation.* International Journal of Heat and Mass Transfer, 1969. **12**(10): p. 1311-1323.
86. Rose, J.W., *Effect of condenser tube material on heat transfer during dropwise condensation of steam.* International Journal of Heat and Mass Transfer, 1978. **21**(7): p. 835-840.
87. Aksan, S.N. and J.W. Rose, *Dropwise condensation—The effect of thermal properties of the condenser material.* International Journal of Heat and Mass Transfer, 1973. **16**(2): p. 461-467.
88. Griffith, P. and L. Man Suk, *The effect of surface thermal properties and finish on dropwise condensation.* International Journal of Heat and Mass Transfer, 1967. **10**(5): p. 697-707.
89. Berndt, V., H. Müller-Steinhagen, and S. Zunft. *Theoretical and experimental study on dropwise condensation in plate heat exchangers*. in *2008 5th European Thermal-Sciences Conference*. 2008.
90. Bonner, R.W., *Correlation for dropwise condensation heat transfer: Water, organic fluids, and inclination.* International Journal of Heat and Mass Transfer, 2013. **61**: p. 245-253.
91. Kim, Y.H., K. Kim, and J.H. Jeong, *Determination of the adhesion energy of liquid droplets on a hydrophobic flat surface considering the contact area.* International Journal of Heat and Mass Transfer, 2016. **102**: p. 826-832.
92. Sikarwar, B., K. Muralidhar, and S. Khandekar, *Effect of drop shape on heat transfer during dropwise condensation underneath inclined surfaces.* Interfacial Phenomena and Heat Transfer, 2013. **1**(4).
93. Bahrami, H.R.T. and H. Saffari, *Theoretical study of stable dropwise condensation on an inclined micro/nano-structured tube.* International Journal of Refrigeration, 2017. **75**: p. 141-154.
94. Bani Kananeh, A., et al., *Experimental study of dropwise condensation on plasma-ion implanted stainless steel tubes.* International Journal of Heat and Mass Transfer, 2006. **49**(25): p. 5018-5026.
95. Wen, R., et al., *Hydrophobic copper nanowires for enhancing condensation heat transfer.* Nano Energy, 2017. **33**: p. 177-183.
96. Liu, X. and P. Cheng, *Dropwise condensation theory revisited Part II. Droplet nucleation density and condensation heat flux.* International Journal of Heat and Mass Transfer, 2015. **83**: p. 842-849.

97. Sokuler, M., et al., *Dynamics of condensation and evaporation: Effect of inter-drop spacing.* Europhysics Letters, 2010. **89**(3): p. 36004.
98. Fatica, N., *DROPWISE CONDENSATION*. 1947: University of MICHIGAN.
99. Maa, J.R., *Drop size distribution and heat flux of dropwise condensation.* The Chemical Engineering Journal, 1978. **16**(3): p. 171-176.
100. Abu-Orabi, M., *Modeling of heat transfer in dropwise condensation.* International Journal of Heat and Mass Transfer, 1998. **41**(1): p. 81-87.
101. Wen, H.W. and R.M. Jer, *On the heat transfer in dropwise condensation.* The chemical engineering journal, 1976. **12**(3): p. 225-231.
102. Wu, Y.-T., C.-X. Yang, and X.-G. Yuan, *Drop distributions and numerical simulation of dropwise condensation heat transfer.* International Journal of Heat and Mass Transfer, 2001. **44**(23): p. 4455-4464.
103. Rose, J.W. and L.R. Glicksman, *Dropwise condensation—The distribution of drop sizes.* International Journal of Heat and Mass Transfer, 1973. **16**(2): p. 411-425.
104. Glicksman, L.R. and A.W. Hunt Jr, *Numerical simulation of dropwise condensation.* International Journal of Heat and Mass Transfer, 1972. **15**(11): p. 2251-2269.
105. Mei, M., et al., *A fractal analysis of dropwise condensation heat transfer.* International Journal of Heat and Mass Transfer, 2009. **52**(21-22): p. 4823-4828.
106. Kim, S. and K.J. Kim, *Dropwise condensation modeling suitable for superhydrophobic surfaces.* 2011.
107. Shang, Y., et al., *Modeling and optimization of condensation heat transfer at biphilic interface.* International Journal of Heat and Mass Transfer, 2018. **122**: p. 117-127.
108. Yang, K.-S., et al., *Experimental investigation of moist air condensation on hydrophilic, hydrophobic, superhydrophilic, and hybrid hydrophobic-hydrophilic surfaces.* International Journal of Heat and Mass Transfer, 2017. **115**: p. 1032-1041.
109. Peng, B., et al., *Analysis of condensation heat transfer enhancement with dropwise-filmwise hybrid surface: Droplet sizes effect.* International journal of heat and mass transfer, 2014. **77**: p. 785-794.
110. Peng, B., et al., *Experimental investigation on steam condensation heat transfer enhancement with vertically patterned hydrophobic–hydrophilic hybrid surfaces.* International Journal of Heat and Mass Transfer, 2015. **83**: p. 27-38.
111. Varanasi, K.K., et al., *Spatial control in the heterogeneous nucleation of water.* Applied Physics Letters, 2009. **95**(9).
112. Morrison, J.N.A. and J. Deans, *Augmentation of steam condensation heat transfer by addition of ammonia.* International Journal of Heat and Mass Transfer, 1997. **40**(4): p. 765-772.
113. Baojin, Q., et al., *Experimental study on condensation heat transfer of steam on vertical titanium plates with different surface energies.* Experimental Thermal and Fluid Science, 2011. **35**(1): p. 211-218.
114. Leu, T.-S., H.-W. Lin, and T.-H. Wu. *Enhancement of phase change heat transfer by using surface energy patterning techniques*. in *2006 1st IEEE International Conference on Nano/Micro Engineered and Molecular Systems*. 2006. IEEE.
115. Chen, D., et al., *Bioinspired superhydrophilic-hydrophobic integrated surface with conical pattern-shape for self-driven fog collection.* Journal of Colloid and Interface Science, 2018. **530**: p. 274-281.
116. Chen, X., et al., *Nanograssed micropyramidal architectures for continuous dropwise condensation.* Advanced functional materials, 2011. **21**(24): p. 4617-4623.
117. Chehrghani, M.M., et al., *Biphilic Surfaces with Optimum Hydrophobic Islands on a Superhydrophobic Background for Dropwise Flow Condensation.* Langmuir, 2021. **37**(46): p. 13567-13575.

118. Wang, S., et al., *Bioinspired hierarchical copper oxide surfaces for rapid dropwise condensation.* Journal of Materials Chemistry A, 2017. **5**(40): p. 21422-21428.
119. Bohn, H.F. and W. Federle, *Insect aquaplaning: Nepenthes pitcher plants capture prey with the peristome, a fully wettable water-lubricated anisotropic surface.* Proceedings of the National Academy of Sciences, 2004. **101**(39): p. 14138-14143.
120. Cheng, Y., et al., *Rapid and persistent suction condensation on hydrophilic surfaces for high-efficiency water collection.* Nano Letters, 2021. **21**(17): p. 7411-7418.
121. Lei, J. and Z. Guo, *A fog-collecting surface mimicking the Namib beetle: its water collection efficiency and influencing factors.* Nanoscale, 2020. **12**(13): p. 6921-6936.
122. Wang, Y., et al., *Biomimetic water-collecting fabric with light-induced superhydrophilic bumps.* ACS applied materials & interfaces, 2016. **8**(5): p. 2950-2960.
123. Garrod, R., et al., *Mimicking a Stenocara Beetle's back for microcondensation using plasmachemical patterned superhydrophobic− superhydrophilic surfaces.* Langmuir, 2007. **23**(2): p. 689-693.
124. Wang, R., et al., *Density maximization of one-step electrodeposited copper nanocones and dropwise condensation heat-transfer performance evaluation.* ACS applied materials & interfaces, 2020. **12**(21): p. 24512-24520.
125. Parin, R., et al., *Heat transfer during dropwise condensation of steam over a mirror polished sol-gel coated aluminum substrate.* International Journal of Thermal Sciences, 2019. **144**: p. 93-106.
126. Gupta, M., et al., *Initiated chemical vapor deposition (iCVD) of conformal polymeric nanocoatings for the surface modification of high-aspect-ratio pores.* Chemistry of Materials, 2008. **20**(4): p. 1646-1651.
127. Azimi, G., et al., *Hydrophobicity of rare-earth oxide ceramics.* Nature materials, 2013. **12**(4): p. 315-320.
128. Chen, L., et al., *n-Octadecanethiol self-assembled monolayer coating with microscopic roughness for dropwise condensation of steam.* Journal of Thermal Science, 2009. **18**: p. 160-165.
129. Hoenig, S.H. and R.W. Bonner III, *Dropwise condensation on superhydrophobic microporous wick structures.* Journal of Heat Transfer, 2018. **140**(7): p. 071501.
130. Hou, Y., et al., *Suppressing ice nucleation of supercooled condensate with biphilic topography.* Physical review letters, 2018. **120**(7): p. 075902.
131. Mouterde, T., et al., *Antifogging abilities of model nanotextures.* Nature materials, 2017. **16**(6): p. 658-663.
132. Wen, R., et al., *Wetting transition of condensed droplets on nanostructured superhydrophobic surfaces: coordination of surface properties and condensing conditions.* ACS applied materials & interfaces, 2017. **9**(15): p. 13770-13777.
133. Mei, M., et al., *A numerical study on growth mechanism of dropwise condensation.* International journal of heat and mass transfer, 2011. **54**(9-10): p. 2004-2013.
134. Ke, Z., et al., *Numerical investigation of condensation on microstructured surface with wettability patterns.* International Journal of Heat and Mass Transfer, 2017. **115**: p. 1161-1172.
135. Stendardo, L., et al., *Out-of-Plane Biphilic Surface Structuring for Enhanced Capillary-Driven Dropwise Condensation.* Langmuir, 2023. **39**(4): p. 1585-1592.
136. Brackbill, J.U., D.B. Kothe, and C. Zemach, *A continuum method for modeling surface tension.* Journal of Computational Physics, 1992. **100**(2): p. 335-354.
137. Lee, W.H., *Pressure iteration scheme for two-phase flow modeling.* IN" MULTIPHASE TRANSPORT: FUNDAMENTALS, REACTOR SAFETY, APPLICATIONS". 1980: p. 407-432.

138. De Schepper, S.C.K., G.J. Heynderickx, and G.B. Marin, *Modeling the evaporation of a hydrocarbon feedstock in the convection section of a steam cracker*. Computers & Chemical Engineering, 2009. **33**(1): p. 122-132.
139. Milne, A. and A. Amirfazli, *Drop shedding by shear flow for hydrophilic to superhydrophobic surfaces.* Langmuir, 2009. **25**(24): p. 14155-14164.
140. Lv, C. and S. Shi, *Wetting states of two-dimensional drops under gravity.* Physical Review E, 2018. **98**(4): p. 042802.

Appendix A

For droplet distribution analysis using ImageJ software, a black and white image was utilized which was derived from the simulations (liquid volume fraction contour), known as binary. To distinguish particles from the background, a specific threshold range was defined. Pixels in the image with values below the threshold were turned black, and those with values above the threshold were turned white. Then, watershed was applied to separate the overlapping particles. Finally, particle analysis was performed which provided information regarding the area of particles that were used to compute the diameter of the particles. Subsequently, the information was analyzed via origin software to identify the number of droplets and their histogram.

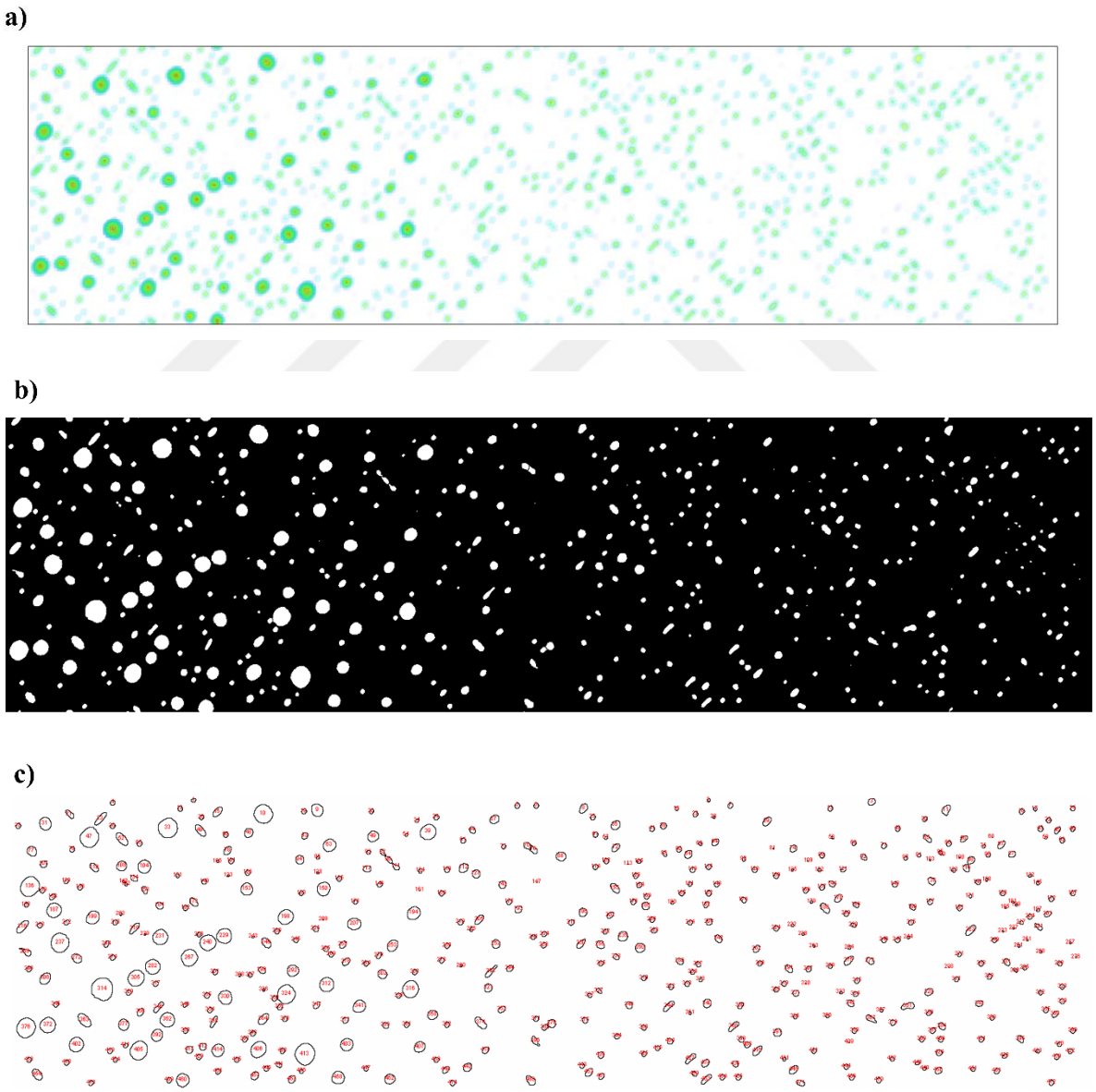

Figure 1. Droplet distribution and droplet counting from a) results of the simulation b) thresholds image using ImageJ software, c) droplet analysis using ImageJ software